THESIS

DYNAMICS AND STRUCTURE OF STABLY STRATIFIED TURBULENCE

Submitted by

Simon Schaad

Department of Civil and Environmental Engineering

In partial fulfillment of the requirements

For the Degree of Master of Science

Colorado State University

Fort Collins, Colorado

Fall 2012

Master's Committee:

Advisor: Subhas Karan Venayagamoorthy

Pierre Y. Julien

Lakshmi Prasad Dasi

ABSTRACT

DYNAMICS AND STRUCTURE OF STABLY STRATIFIED TURBULENCE

The dynamics and turbulent structures of stably stratified turbulence are explored via direct numerical simulations (DNS). The structural features of stratified turbulence and its relationship to the flow dynamics has been the subject of many recent investigations. In strongly stratified turbulent flows, the formation of large-scale quasi-horizontal vortices in layers with strong vertical variability has been observed in laboratory experiments. Enstrophy isosurfaces of strongly stable flows indicate the emergence of randomly distributed 'pancake'-like structures with near horizontal orientation at later times. The strongly stratified simulations are diffusive and dominated by linear internal waves. The results suggest a decoupling between horizontal and vertical dynamics as the vertical dynamics can be described using rapid-distortion theory (RDT) while horizontal dynamics continue to be dominated by non-linear effects not captured by RDT.

The integral flux Richardson number for decaying turbulence is the ratio of background potential energy gain to turbulent kinetic energy loss. The traditional flux-based formulation converges upon this ratio only when integrations are performed over an entire event, while the irreversible formulation converges rapidly without error from reversible effects. Mixing efficiency is a property of the flow for energetic flow but becomes a property of the fluid for diffusive flows and subject to Prandtl number effects. RDT models predict the flux Richardson number scales as the inverse Prandtl number at the diffusive limit when the Prandtl number is greater than unity. Mixing efficiency comparisons between DNS and physical grid-tow experiments reveal a large discrepancy for strong stratification, which is attributed in part to the low Reynolds numbers attained in both DNS and grid-tow experiments.

Overturns are unstable conditions where heavier fluid resides above lighter fluid. The collapse of these local instabilities produce additional patches of turbulence and

mixing making overturns an important mechanism in stratified turbulence. The overturning structures in strongly stratified flow resemble the quasi-horizontal vorticity structures and were found to be correlated with increased horizontal vorticity. The Thorpe scale, a measure of overturning structure height, and the Ozmidov scale equate only at the critical condition where inertial and buoyancy effects are equal (i.e. the turbulent Froude number is unity). The error of inferred dissipation rates from equating the Thorpe and Ozmidov scales was found to be up to two orders of magnitude.

ACKNOWLEDGEMENTS

This thesis would not have been possible without the guidance and teachings from my advisor Dr. Karan Venayagamoorthy. Studying fluid mechanics at CSU has been a fantastic journey and I would like to acknowledge Dr. Venayagamoorthy and his fluid mechanics research group for their support and help with the ideas presented in this work. Thanks to Ben Mater for his help, useful feedback, and collaboration on the overturning length scale ideas in Sec. (4.3). And thanks to Farid Karimpour for helping me solve those tricky calculus problems.

I would like to acknowledge Dr. Pierre Julien and Dr. Prasad Dasi for generously volunteering their time to be on my committee and read my thesis.

Thanks to Lobo, Argos, and Hayek for their loyal company, Caesar for warming my lap, Gaius for spilling drinks on my laptop, and Sawyer for his loud, 3-legged thumping.

Of course this thesis could not have been possible without the loving support from my family (albeit far removed from Colorado).

Most importantly, thanks to Emily Chryst for her love, patience, and sharing her life with me.

DEDICATION

Dedicated to my muse, my friend, and my love;

Emily

TABLE OF CONTENTS

LIST OF TABLES

LIST OF FIGURES

Chapter 1

Introduction

1.1 Background

Stably stratified flows are a rich subject of fluid mechanics due to the coupled relationship between kinetic and potential energy. Gravity acts on the internal dynamics through buoyancy forces, which fundamentally changes the behavior of the fluid. The mechanics of stratified flows are important in a wide range of environments ranging from small scale engineering flows to large scale geophysical flows. Buoyancy forces produce many interesting effects, such as internal waves and anisotropic turbulence making the study of stratified flows a complex but rewarding field.

Turbulence is generally produced by shear mechanisms which further control the decay process. In this work the decay process is isolated from more complex turbulent processes in an attempt to better understand fundamental fluid mechanics. The decay processes of stratified turbulence are simulated by allowing a burst of turbulent kinetic energy in a continuously stratified fluid to decay without further production. The decaying turbulence is akin to the event following a breaking internal wave or other disturbance.

Direct Numerical Simulations (DNS) allow for the exact solution of stratified turbulence to be attained by resolving all scales of motion, ranging from the upper energy-containing range to the lower viscous limit. The lower viscous limit is defined by the size of smallest eddies that can exist, beyond which viscosity acts to rapidly dissipate the energy. The upper energy-containing limit is defined by the largest eddies produced by the initial event. The crux of the problem lies within the massive chasm of length scales which must be accurately resolved. Most DNS studies are heavily inhibited by computational restrictions resulting in low Reynolds number simulations. Regardless, DNS studies continue to be an important avenue to further explore fundamental physics of turbulent flows.

1.2 Objectives

The DNS code used in this work was developed by Riley, Metcalfe & Weissman in 1981, which, as per Moore's law, has been run on ever faster computers. Initially the code was restricted to a domain with 32^3 grid points resulting in a Taylor Reynolds number equal to 27. This work utilizes a domain 512 times larger with 256^3 grid points and a Taylor Reynolds numbers of order 100. The dynamics of diffusive and laminar flows are of little insight into the mechanics of stratified turbulence in environmental flows. The goal of this work is to further understand the mechanics of stratified turbulence at high Reynolds numbers. The Reynolds numbers achieved in this work are still too low for direct comparison with high Reynolds number flows, however, the mechanics of high Reynolds number flows can be inferred from trends and dimensional arguments.

The main objectives of this work are:

(i) to study the dynamics and coherent turbulent structures of decaying stratified turbulence, and

(ii) to investigate the relationship of mixing efficiency of decaying turbulence and stratification, the Prandtl number, and the Reynolds number, and

(iii) to investigate the nature of overturning structures and the relationship between overturning length scales.

1.3 Thesis layout

Chapter 2 contains a brief literature review on previous studies. Fluid mechanics theory on stratified turbulence is reviewed; specifically the governing equations, relevant scales, and important non-dimensional parameters. Additionally, the simulation setup and numerical methods of DNS are discussed

Chapter 3 addresses objectives (i) and (ii). A large parametric study of DNS with varying stratification, Prandtl numbers, and Reynolds number was performed to study the dynamics and coherent turbulent structures of stratified turbulence. The discrepancy between physical and numerical experiments previously brought to light by Stretch *et al.*

(2010) is further explored. Rapid-Distortion Theory (RDT) was used to model diffusive flows outside DNS constraints.

Overturn structures are studied in Chapter 4, covering objective (iii). Length scales can readily be measured from overturns and are an important tool used by oceanographers. However, it is unclear under what conditions overturning length scale are related. The parametric studies from Chapter 3 are used to investigate the relationship between overturning length scales.

The conclusions and recommendations for further work are given in Chapter 5.

1.4 Research presentations and publications

- An abstract entitled "M1.00003: Dynamics and structure of stably stratified turbulence" and accompanying oral talk was presented at American Physical Society Division of Fluid Dynamics conference on November 22, 2011, in Baltimore, Maryland, USA.

- An abstract entitled "Flow structures and dynamics of stably stratified turbulence" and accompanying oral talk was presented at AGU Hydrology Days 2012, March 23, in Fort Collins, Colorado, USA.

- A paper entitled "Relevance of the Thorpe scale in stably stratified turbulence" by Ben Mater, Simon Schaad, and Subhas K. Venayagamoorthy, which includes findings from Chapter 4, is currently under review for publication in the Journal of Physical Oceanography.

- A paper entitled "Dynamics and structure of stably stratified turbulence" by Simon Schaad and Subhas K. Venayagamoorthy summarizing the findings from Chapter 3 and 4 is currently under preparation for publication in the Journal of Fluid Mechanics.

Chapter 2

Literature Review

2.1 Introduction

Waves are present in most environmental flows and are disturbances from an equilibrium state where subsequent motions depend on the restoring force or forces. For large scale flows, planetary rotation manifests as a restoring force. For smaller scale flows with stratification, internal waves form due to the restoring force of gravity. Stable stratification (i.e. vertical density gradients) arises from temperature and/or salinity variations in the natural environment such as oceans and the atmosphere. The behavior of internal waves is dependent on the nature of the stratification. Two broad simplifications are usually made in analyzing stably stratified flows:

(i) Layered flows - This allows the flow to be analyzed layer by layer with added simplifications of hydrostatic pressure distribution and neglect of non-linear effects such that different analytical solutions are feasible.

(ii) Continuously stratified flows - Can be thought of as the limit of an infinite number of layers. Analysis of continuously stratified flows are more involved because the flow dynamics are three-dimensional.

In most flows of interest, shear is an important mechanism which contributes to turbulent events. Kinetic energy is eventually dissipated by turbulence. The traditional governing time scales of environmental flows are the Coriolis frequency f from rotation, buoyancy frequency N from gravity and stratification, the mean shear rate S, and the turbulent time scale T_L. In this work rotation and shear are neglected shortening the list to N and T_L.

In what follows; the theory of stratified turbulence and governing equations are discussed in Sec. (2.2), mixing processes and previous research is reviewed in Sec. (2.3), scales controlling fluid motion and important non-dimensional parameters are reviewed in Secs. (2.4)-

(2.5), and limitations and numerical methods of DNS are discussed in Sec. (2.6).

2.2 Equations of motion

All fluid motion can be fully described by the governing principles of momentum, mass, and energy conservation. The governing equations of fluid motion are formulated from these three governing principles. The incompressible, irrotational, and stratified form of the governing equations are described in Sec. (2.2.1). The energetics of fluid motion are very insightful into the physical processes. The equations of turbulent kinetic energy, turbulent potential energy, and total energy are described in Sec. (2.2.2).

2.2.1 Governing equations

In non-stratified turbulence, density does not play an active role and only the conservation of momentum and mass principles are required to describe the fluid flow. Stratification introduces an additional level of complexity and requires the conservation of energy to be coupled with conservation of momentum and mass equations. The conservation of momentum equations are commonly called the Navier-Stokes equations and are described in Sec. (2.2.1.1). The conservation of mass equation is commonly called the continuity equation and is given in Sec. (2.2.1.2). The incompressible energy equation, described in Sec. (2.2.1.3), is a simple advection-diffusion equation of density. Non-dimensional forms of the governing equations are presented in Sec. (2.2.1.4).

2.2.1.1 Navier-Stokes equations

The Navier-Stokes equations result from the conservation of momentum principle. In large scale geophysical flows, the Coriolis force becomes large enough to require consideration in addition to gravity. This work focuses on small-scale turbulent events and the Rossby number Ro is certainly many orders of magnitude larger than unity rendering the rotational effects to be negligible. The only external force included is gravity.

For such a case, the Navier-Stokes equations simplify to

$$\rho \frac{D\mathbf{u}}{Dt} = -\nabla p + \rho \mathbf{g} + \rho \nu \nabla^2 \mathbf{u}, \tag{2.1}$$

where ρ is density, $D()/Dt$ is the material, or total, derivative, $\mathbf{u}$ is the velocity vector of the form (u, v, w), ∇p is the pressure gradient, $\mathbf{g}$ is the acceleration of gravity, and ν is the molecular kinematic viscosity (Munson *et al.*, 2008). There is no general analytic solution to the Navier-Stokes equations due to it being a set of non-linear partial differential equations with parabolic, hyperbolic, and elliptic behavior (Moin, 2010). It is these properties which are responsible for the coupling between small and large scale motions resulting in the exchange of energy and momentum between eddies of different size (Ouellette, 2012). Solutions are generally achieved through a combination of simplifications and discretization techniques.

Stratified flows are often simplified with the Boussinesq approximation. To begin, the instantaneous density and pressure of a particle can be decomposed into reference quantities, ρ_o and p_o, mean quantities, $\overline{\rho}$ and $\overline{p}$, and fluctuations from the mean, ρ' and p', such that $\rho = \rho_o + \overline{\rho} + \rho'$ and $p = p_o + \overline{p} + p'$. If the decomposed density and pressure are inserted into Eq. (2.1) and a background hydrostatic pressure distribution is assumed of the form $\nabla p_o = \rho_o \mathbf{g}$, the Navier-Stokes equations can be rearranged such that

$$\left(1 + \frac{\rho'}{(\rho_o + \overline{\rho})}\right) \frac{D\mathbf{u}}{Dt} = -\frac{1}{(\rho_o + \overline{\rho})} \nabla p' + \frac{\rho'}{(\rho_o + \overline{\rho})} \mathbf{g} + \left(1 + \frac{\rho'}{(\rho_o + \overline{\rho})}\right) \nu \nabla^2 \mathbf{u}. \tag{2.2}$$

If $\rho'/(\rho_o + \overline{\rho}) \ll 1$ it can be seen that $\rho'/(\rho_o + \overline{\rho})$ is of secondary importance to the inertial terms but is of primary importance to the buoyancy term $\mathbf{g}\rho'/(\rho_o + \overline{\rho})$. The Boussinesq approximation is the assumption that density fluctuations can be neglected in the inertial terms but retained in the buoyancy term if $\rho'/(\rho_o + \overline{\rho}) \ll 1$ (Turner, 1973). Additionally, $\overline{\rho}$ is also assumed negligible because $\overline{\rho} \ll \rho_o$ in environmental flows. Thus, the Navier-Stokes equations for irrotational, incompressible, and stratified flows with the Boussinesq

approximation simplify to

$$\frac{D\mathbf{u}}{Dt} = -\frac{1}{\rho_o}\nabla p' + \frac{\rho'}{\rho_o}\mathbf{g} + \nu\nabla^2\mathbf{u}. \tag{2.3}$$

If the fluid is homogeneous then ρ', and subsequently the buoyancy term, are zero. The increased complexity associated with stratification is revealed by the extra buoyancy term in the Navier-Stokes equations.

2.2.1.2 Continuity equation

The conservation of mass principle in integral form from a flux, or Eulerian, perspective is the continuity equation,

$$\frac{\partial\rho}{\partial t} + \nabla\cdot(\rho\mathbf{u}) = 0. \tag{2.4}$$

Using the material derivate $D()/Dt = \partial()/\partial t + \mathbf{u}\cdot\nabla()$, the continuity equation can be rearranged into the material, or Lagrangian, form as

$$\frac{D\rho}{Dt} + \rho\cdot\nabla(\mathbf{u}) = 0. \tag{2.5}$$

If Eq. (2.5) is divided by ρ the material derivative is of order ρ^{-1} while the velocity divergence is of order unity. Implementing the Boussinesq approximation by ignoring terms of higher order, the continuity equation simplifies to a solenoidal velocity field (i.e. it is divergence free) as

$$\nabla\cdot\mathbf{u} = 0 \tag{2.6}$$

2.2.1.3 Density transport equation

The behavior of stratified flows requires additional equations due to density being an 'active' variable because it affects the behavior of Eqs. (2.3) and (2.6) (Pope, 2000). For incompressible flows, the transport of density can be treated as the transport of any scalar but is coupled with Eqs. (2.3) and (2.6). The density transport equation is simply an

advection-diffusion equation given by

$$\frac{D\rho'}{Dt} = \kappa \nabla^2 \rho', \tag{2.7}$$

where κ is the coefficient of molecular diffusion[1](Turner, 1973).

It is important to note that the density transport equation is a special case of energy conservation when incompressibility is assumed and stratification is due to a single agent (e.g. heat or salt). (Gill, 1982)

2.2.1.4 Non-dimensional form of governing equations

The non-dimensionalized form of the governing equations are solved by the DNS code for generality and programming ease. Using the initial velocity scale u_0, the initial length scale L_0, and the background density scale $L_0|\partial\overline{\rho}/\partial z|$ as characteristic scales, the non-dimensional form of the governing equations are

$$\frac{D\mathbf{u}^+}{Dt^+} = -\nabla p^+ - Ri\rho^+\delta_{i3} + \frac{1}{Re_0}\nabla^2\mathbf{u}^+ \tag{2.8}$$

$$\nabla \cdot \mathbf{u}^+ = 0 \tag{2.9}$$

$$\frac{D\rho^+}{Dt^+} = \frac{1}{Re_0 Pr}\nabla^2\rho^+, \tag{2.10}$$

where the flow field parameters are normalized as $\mathbf{u}^+ = \mathbf{u}(u_0)^{-1}$, $p^+ = p'(\partial\overline{\rho}/\partial z)^{-1}(u_0)^{-2}$ $(L_0)^{-1}$, and $\rho^+ = \rho'(\partial\overline{\rho}/\partial z)^{-1}(L_0)^{-1}$. The other variables are normalized as $t^+ = tu_0(L_0)^{-1}$, $x_i = x_i^+(L_0)^{-1}$ and $\rho_o^+ = \rho_o(\partial\overline{\rho}/\partial z)^{-1}(L_0)^{-1}$. The non-dimensional numbers are the initial Richardson number $Ri = (NL_0/u_0)^2$ (Eq. 2.56), the initial Reynolds number $Re_0 = u_0L_0/\nu$ (Eq. 2.58), and the Prandtl number $Pr = \nu/\kappa$. In this work, all three non-dimensional numbers are varied in parametric studies. All results presented in this work are non-dimensionalized as above but the superscript indicating non-dimensionalization is dropped for the remainder of this work.

[1]The Reynolds averaged form of the density transport equation with the gradient-diffusion hypothesis is similar to Eq. (2.7) but κ is replaced by the effective diffusivity κ_{eff} equal to the sum of the molecular diffusivity κ and eddy diffusivity K_ρ. See Sec. (3.6).

2.2.2 Energetics

In stratified flows both the kinetic and potential energy must be considered. The turbulent kinetic equation is derived in Sec. (2.2.2.1) by using the Reynolds decomposition of the Navier-Stokes equations. The turbulent potential energy equation is derived from the scalar transport equation in Sec. (2.2.2.2) and combined with the turbulent kinetic equation in Sec. (2.2.2.3) to form the total turbulent energy equation.

2.2.2.1 Turbulent kinetic energy

The turbulent kinetic energy per unit mass k is one half of the isotropic Reynolds stresses,

$$k = \tfrac{1}{2}\overline{u_i' u_i'}. \tag{2.11}$$

To derive an equation for the evolution of kinetic energy equation, the Navier-Stokes (i.e. instantaneous momentum equations) and a spatial-average form of the Navier-Stokes equations must be combined.

The spatial-average forms of the Navier-Stokes equations are called the Reynolds equations. The total velocity u_i can be decomposed into a mean $\overline{u}_i$ and fluctuations from the mean u_i', such that $u_i = \overline{u}_i + u_i'$. Taking the mean of Eq. (2.3) with velocity decompositions, the Reynolds equations in Einstein summation notation are

$$\frac{\partial \overline{u}_i}{\partial t} + \overline{u}_j \frac{\partial \overline{u}_i}{\partial x_j} = -\frac{1}{\rho_o}\frac{\partial p'}{\partial x_i} + \nu \frac{\partial^2 \overline{u}_i}{\partial x_i^2} + \frac{\rho'}{\rho_o} g \delta_{i3} - \underbrace{\frac{\partial \overline{u_i' u_j'}}{\partial x_i}}_{\substack{\text{Divergence} \\ \text{of Reynolds} \\ \text{stress}}} . \tag{2.12}$$

The Reynolds equations are identical to the Navier-Stokes equations except for the extra divergence of the Reynolds stress term. The Reynolds stresses $\overline{u_i' u_j'}$ are the velocity fluctuation covariances and capture the non-linear influence of turbulence from the fluctuation fields.

Combining the Navier-Stokes equations (Eq. 2.3) and Reynolds equations (Eq. 2.12), the turbulent kinetic energy equation can be derived. The turbulent kinetic energy equation

with the Boussinesq approximation is (Mansour *et al.*, 1988)

$$\underbrace{\frac{\partial k}{\partial t}}_{\substack{\text{Local}\\\text{derivative}}} + \underbrace{\overline{u}_j\frac{\partial k}{\partial x_j}}_{\text{Advection}} = -\underbrace{\frac{1}{\rho_o}\frac{\partial \overline{u_i' p'}}{\partial x_i}}_{\substack{\text{Pressure}\\\text{diffusion}}} - \underbrace{\frac{\partial \overline{k u_i}}{\partial x_j}}_{\substack{\text{Turbulent}\\\text{transport}\\\mathcal{T}}} + \underbrace{\nu\frac{\partial^2 k}{\partial x_j^2}}_{\substack{\text{Molecular}\\\text{viscous}\\\text{transport}}} \underbrace{-\overline{u_i' u_j'}\frac{\partial \overline{u_i}}{\partial x_j}}_{\substack{\text{Production}\\\mathcal{P}}} - \cdots$$

$$\underbrace{\nu\overline{\frac{\partial u_i'}{\partial x_j}\frac{\partial u_i'}{\partial x_j}}}_{\substack{\text{Kinetic energy}\\\text{dissipation}\\\text{rate,}^1\epsilon_k}} + \underbrace{\left(-\frac{g}{\rho_o}\overline{\rho' u_i'}\delta_{i3}\right)}_{\substack{\text{Buoyancy flux}\\b}}. \tag{2.13}$$

As there are no mean velocity gradients in the flows analyzed in this work, the advection and $\mathcal{P}$ terms to be zero. The turbulence is assumed homogeneous (i.e. statistically invariant under translations of the reference frame, Pope 2000) rendering the transport terms to also be zero. For small Mach numbers (i.e. $Ma \ll 1$) the pressure diffusion term is negligible and is assumed to be zero. Thus, the turbulent kinetic energy equation simplifies to the much more tractable form

$$\frac{\partial k}{\partial t} = -\epsilon_k + b. \tag{2.14}$$

2.2.2.2 Turbulent potential energy

Potential energy is present in stratified flows as density gradients, and acts through the buoyancy force. Buoyancy forces arise if vertical density gradients are non-zero. Fig. (2.1) illustrates the buoyancy forces in stratified flows. If a light fluid is above a heavy fluid (Fig. 2.1a), the buoyancy force acts restoratively and the stratification is stable. If a light fluid is *below* a heavy fluid, an overturning force is created (Fig. 2.1b) which leads to a release of kinetic energy. Thus, stable stratification acts as a sink of kinetic energy and unstable stratification as a source.

[1]The true turbulent kinetic energy dissipation rate is $2\nu\overline{s_{ij}s_{ij}}$, where s_{ij} is the rate-of-strain tensor $\frac{1}{2}(\partial u_i/\partial x_j + \partial u_j/\partial x_i)$, and is related to ϵ_k as

$$2\nu\overline{s_{ij}s_{ij}} = \epsilon_k + \nu\frac{\partial^2 \overline{u_i u_j}}{\partial x_i \partial x_j}. \tag{2.15}$$

The final last term is very small rendering distinction between true dissipation and ϵ_k negligible (Pope, 2000).

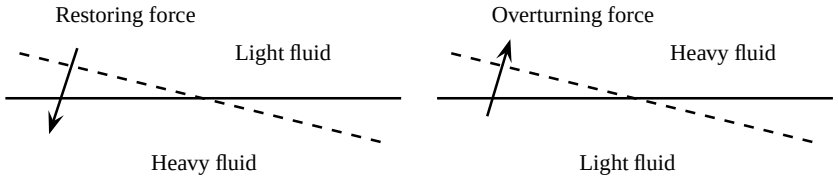

(a) Restoring Force **(b)** Overturning Force

Figure 2.1: Buoyancy forces in stable and unstable stratification - The buoyancy force for stable stratification (a) acts as a sink of energy while the buoyancy force for unstable stratification (b) acts as a source of energy. Figure adapted from Turner (1973).

The mean turbulent potential energy per unit mass E_p can be defined by the mean energy stemming from density fluctuations ρ' and the displaced distance dz as

$$E_p = -\frac{g}{\rho_o}\overline{\int \rho' \, dz}. \tag{2.16}$$

Using $\rho' = (\partial\overline{\rho}/\partial z)z'$, where z' is the vertical displacement from a stable position along the background density gradient, Eq. (2.16) can be written as

$$E_p = -\frac{g}{\rho_o}\left(\frac{\partial\overline{\rho}}{\partial z}\right)\overline{\int z' \, dz}. \tag{2.17}$$

Solving Eq. (2.17) and substituting z' with $\rho'(\partial\overline{\rho}/\partial z)^{-1}$, E_p can be defined as (Venayagamoorthy & Stretch, 2010)

$$E_p = -\frac{g}{\rho_o}\left(\frac{\partial\overline{\rho}}{\partial z}\right)^{-1}\tfrac{1}{2}\overline{\rho'^2} = N^2\left(\frac{\partial\overline{\rho}}{\partial z}\right)^{-2}\tfrac{1}{2}\overline{\rho'^2}, \tag{2.18}$$

where N is the buoyancy frequency (Eq. 2.47).

The turbulent potential energy equation can be derived from the scalar variance equation, which is derived from the instantaneous and mean forms of the advection-diffusion equation (Eq. 2.7). The scalar variance equation is (Winters & D'Asaro, 1996)

$$\underbrace{\frac{\partial\overline{\frac{1}{2}\rho'^2}}{\partial t}}_{\substack{\text{Local}\\ \text{derivative}}} + \underbrace{\overline{u}\cdot\nabla\overline{\tfrac{1}{2}\rho'^2}}_{\text{Advection}} = -\underbrace{\overline{u'\rho'}\cdot\nabla\overline{\rho}}_{\text{Flux}} - \underbrace{\nabla\cdot\overline{u'\tfrac{1}{2}\rho'^2}}_{\text{Transport}} + \underbrace{\kappa\overline{\rho'\nabla^2\rho'}}_{\substack{\text{Density}\\ \text{dissipation}\\ \text{rate, } \epsilon_\rho}}. \tag{2.19}$$

As mean velocity gradients are absent from the flow the advection term is zero. Additionally, the turbulence is assumed homogeneous so that the transport term is also zero. Using the product rule, $\overline{\rho'\nabla^2\rho'}$ can be written as

$$\overline{\rho'\nabla^2\rho'} = -\overline{\nabla\rho'\cdot\nabla\rho'} + \nabla\cdot\overline{(\rho'\nabla\rho')}. \tag{2.20}$$

For homogeneous turbulence the last term in Eq. (2.20) is zero allowing ϵ_ρ to be defined as (Venayagamoorthy & Stretch, 2006)

$$\epsilon_\rho = \kappa\overline{\frac{\partial\rho'}{\partial x_j}\frac{\partial\rho'}{\partial x_j}}. \tag{2.21}$$

Thus, the vertical scalar variance equation for decaying stratified turbulence becomes (Venayagamoorthy & Stretch, 2010)

$$\frac{\partial\frac{1}{2}\overline{\rho'^2}}{\partial t} = \kappa\overline{\frac{\partial\rho'}{\partial x_j}\frac{\partial\rho'}{\partial x_j}} - \overline{\rho'w'}\frac{\partial\overline{\rho}}{\partial z}. \tag{2.22}$$

Multiplication of Eq. (2.22) by $-(g/\rho')(\partial\overline{\rho}/\partial z)^{-1}$ gives the turbulent potential energy equation under the Boussinesq approximation

$$\frac{\partial E_p}{\partial t} = \underbrace{-\frac{g}{\rho_o}\left(\frac{\partial\overline{\rho}}{\partial z}\right)^{-1}\kappa\overline{\frac{\partial\rho'}{\partial x_j}\frac{\partial\rho'}{\partial x_j}}}_{\substack{\text{Potential energy}\\ \text{dissipation rate}\\ \epsilon_p}} \underbrace{-\left(-\frac{g}{\rho_o}\overline{\rho'w'}\right)}_{\substack{\text{Buoyancy flux}\\ b}}, \tag{2.23}$$

or written more simply as

$$\frac{\partial E_p}{\partial t} = -\epsilon_p - b. \tag{2.24}$$

2.2.2.3 Total energy

The total energy E_T is the sum of the turbulent potential and turbulent energy such that $E_T = k + E_p$. From Eqs. (2.14) and (2.24) it follows that

$$\frac{dE_T}{dt} = -\epsilon_k - \epsilon_p = -\epsilon_T, \tag{2.25}$$

where ϵ_T is the total energy dissipation rate. This relationship shows that the buoyancy flux is a reversible mechanism which converts energy between k and E_p but does not influence the total energy in the system. When energy is fluxed from kinetic to potential form, particles are displaced from equilibrium positions creating a buoyancy force and increasing E_p. When the particles are accelerated back towards their equilibrium positions k increases while E_p decreases. The total turbulent energy dissipation rate ϵ_T acts as an irreversible sink of energy.

2.3 Turbulent mixing

Turbulence is responsible for the efficient mixing of quantities such as momentum and scalars. The degree of mixing is a much sought-after quantity in fluid mechanics and in broader related fields. For example, the design of aquaculture farms requires knowledge about the dispersion of antibiotic-laden waste (Venayagamoorthy *et al.*, 2011). An example at a much larger scale is predicting climate change phenomena. As the ocean surface warms the ocean becomes more stratified resulting in decreased vertical mixing. When less oxygen is transported to depths the level of "dead" oxygen-deficient water rises. Mass die-offs of marine life occur when wind induced mixing brings this "dead" water near the surface (Roberts, 2012).

In general fluid mechanics 'mixing' and 'stirring' are used to describe rather different processes. Stirring denotes advective mixing resulting from the interaction of turbulent eddies and is a property of the flow. Mixing denotes molecular diffusion and is a property of the fluid and is not influenced by turbulence (Tseng & Ferziger, 2001). Stationary fluids will mix due to molecular diffusion, but for large scale flows this process is of the order of geologic time scales. In this work 'mixing' will imply both molecular mixing and advective stirring but will be differentiated as either molecular or advective mixing, respectively.

Mixing efficiency Γ is an important parameter to quantify the role of irreversible mixing and is described in Sec. (2.3.1). Mixing efficiency is used in oceanography and climatology to predict the role of small scale turbulence in large scale processes. For example, models

of global energy budgets must quantify energy loss due to kinetic energy being transformed into potential energy (e.g. Munk & Wunsch, 1998) such as the energy transfer from tidal forcing to small scale turbulent mixing (Wunsch & Ferrari, 2004). Accurate models of mixing efficiency allow hypothetical climate change scenarios to be investigated. The value of Γ is usually derived experimentally because the theoretical dependence of Γ on different flow types and parameters is still an open question (Fernando, 1991).

2.3.1 Mixing efficiency and flux Richardson number

The instantaneous mixing efficiency Γ is the irreversible ratio of potential energy loss to kinetic energy loss (Venayagamoorthy & Stretch, 2010), written as

$$\Gamma = \frac{\epsilon_p}{\epsilon_k}. \tag{2.26}$$

Integrations over an entire event yields a mixing efficiency coefficient Γ,

$$\Gamma = \frac{\int \epsilon_p \, dt}{\int \epsilon_k \, dt}. \tag{2.27}$$

The instantaneous mixing efficiency varies considerably throughout an overturning event and is not a focus in this work.[1]The interest in this work is on energy conversions over an entire event. Unless otherwise specified, in this work 'mixing efficiency' and Γ will denote the integral mixing efficiency.

The flux Richardson number Rf is traditionally defined as the ratio of the rate of removal of kinetic energy by buoyancy to the production of turbulent kinetic energy (Turner, 1973),

$$Rf = \frac{b}{\mathcal{P}}. \tag{2.28}$$

For stationary or decaying turbulence Rf must be less than unity (Osborn, 1980). For stationary and homogeneous turbulence, the turbulent kinetic energy equation (Eq. 2.13)

[1]See Park *et al.* (1994) for a study on the evolution of instantaneous mixing efficiency in grid-tow experiments.

simplifies to (Holt *et al.*, 1992)

$$\mathcal{P} - \epsilon_k - b = 0, \tag{2.29}$$

allowing $\mathcal{P}$ to be substituted with $\epsilon_k + b$ in Eq. (2.28). For decaying turbulence (i.e. $\mathcal{P} = 0$), this substitution is also valid for time integrations over an entire event because the time integrations are equivalent to the stationarity condition (Abarzhi, 2011). The integral flux Richardson number for decaying turbulence can therefore be written as

$$Rf = \frac{\int b\, dt}{\int (\epsilon_k + b)\, dt}. \tag{2.30}$$

The integral flux Richardson number is a commonly used parameter by oceanographers and engineers as it describes mixing processes over an entire event. Unless otherwise specified, for the remainder of this work 'flux Richardson number' and Rf will denote the integral flux Richardson number.

DNS results are validated using Rf with results from Venayagamoorthy (2002) and Stretch *et al.* (2010) who calculate Rf as

$$Rf = \frac{\int b\, dt}{\Delta k}. \tag{2.31}$$

DNS results are compared with grid-tow experiments in Sec. (3.6.2). In the grid-tow experiments $\int b\, dt$ is measured from the density profile changes. The flux Richardson number can be interpreted as the ratio of total potential energy gain to total turbulent kinetic energy loss.

It is shown in Sec. (3.3.4) that for an entire turbulent event $\int b\, dt$ converges with $\int \epsilon_p\, dt$ because the net turbulent potential energy E_p change is approximately zero. Therefore, Rf can be rewritten as (Peltier & Caulfield, 2003)

$$Rf = \frac{\int \epsilon_p\, dt}{\int \epsilon_k\, dt + \int \epsilon_p\, dt}. \tag{2.32}$$

Venayagamoorthy & Stretch (2010) argue Eq. (2.32) is a more appropriate formulation because it is only a measure of irreversible mixing without reversible fluxes. From the

turbulent kinetic energy equation (Eq. 2.13) it can be seen that Eqs. (2.30-2.32) should be equal. Different formulations of Rf presented in this section are compared in Sec. (3.3.4). Unless otherwise specified, Rf is calculated in this work using Eq. (2.32).

From Eqs. (2.27) and (2.32), mixing efficiency can be related to Rf as

$$\Gamma = \frac{Rf}{1 - Rf}. \tag{2.33}$$

The ratio of total potential energy gain to total turbulent kinetic energy loss can therefore be related to irreversible mixing processes. At low Rf, $\Gamma \approx Rf$, but at high Rf, Γ is larger than Rf (e.g. $Rf = \frac{1}{4}$ corresponds with $\Gamma = \frac{1}{3}$).

2.3.2 Physical experiments

Many studies have used physical experiments to measure Rf. Rouse & Dodu (1955) first performed grid-tow experiments by towing a bi-planar grid across a fluid bath to produce turbulence. The characteristic length scale L_0 is given by the grid geometry because the largest eddies are confined to grid openings and the characteristic velocity scale u_0 is given by the tow velocity. The DNS experiments in this work simulate a burst of isotropic turbulence and the subsequent decay absent of further production such as shear or forcing. The initial characteristic scales L_0 and u_0 from DNS initial conditions correspond with grid-tow characteristic scales and allow for direct comparison between physical and numerical experiments.

In grid-tow experiments with stratified fluids, each tow introduces an initially isotropic turbulence field but as the flow evolves it becomes anisotropic due to buoyancy effects. The addition of kinetic energy into the stratified system will increase the potential energy by mixing the inital density profile because a homogeneous fluid has a higher center of gravity than a stably stratified fluid. To illustrate, experimental density profiles from Rehmann & Koseff (2004) are shown in Fig. (2.2). Each tow further mixes the density gradient. After enough grid-tow passes the fluid will become homogeneous.

In Fig. (2.2) the density profile initially changes at the top and bottom zero flux bound-

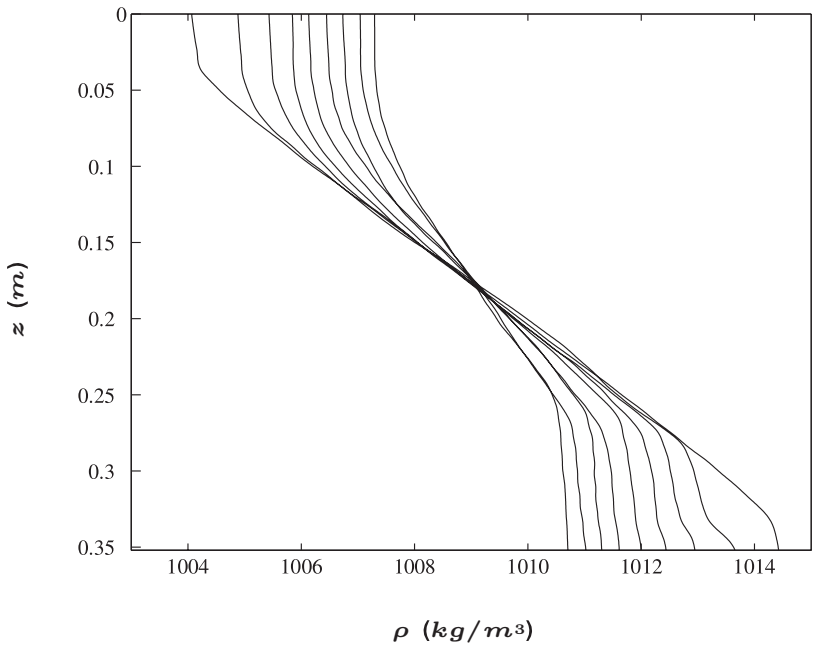

Figure 2.2: Density profile mixing in physical experiment - Density profile mixing from grid-tow experiments from Rehmann & Koseff (2004). The density profile was measured after each grid-tow once all turbulence decayed. The turbulent bursts increase the potential energy by destroying the density gradient resulting in a higher center of gravity.

aries. The density profile in the center of the domain remains constant because the fluxes are approximately in equilibrium. Thus, a net vertical buoyancy flux transports mass upward through the center of the domain. The mass de-accumulation at the bottom and accumulation at the top begin to influence the density profile in the center at later times because the domain is of finite height.

The domain for DNS of decaying turbulence is an idealized box located at the center of a tank of infinite height where vertical buoyancy fluxes are in equilibrium. The background density profile is therefore uniform for all time. Tennekes & Lumley (1974) showed that mean fields are decoupled from the flow resulting in subsequent decoupling of the background density profile from buoyancy fluxes (Venayagamoorthy, 2002). The background density profile remains constant and only the buoyancy flux must be accounted for which allows the vertical boundary conditions, in addition to horizontal boundary conditions, to be set as periodic.

In this work, DNS experiments are compared with physical experiments by Britter

(1985), Rottman & Britter (1986), and Rehmann & Koseff (2004). The potential energy after n tows E_{p_n} was calculated from the measured density profile $\overline{\rho}_n(z)$ as

$$E_{p_n} = LW \int_0^H \overline{\rho}_n(z) g z \, dz, \tag{2.34}$$

where L, W, H are the tank length, width, and height, respectively. The total energy input into each tow was calculated from the drag force F_D on the grid as

$$F_D = C_D \tfrac{1}{2} \rho_o u^2 W H, \tag{2.35}$$

where C_D is a calibrated drag coefficient and u is the velocity of the grid during the tow. The total energy E_{input} is then equal to $F_D L$.

Given E_{P_n} and E_{input}, Rf from n tows can be defined as

$$Rf_n = \frac{E_{p_n} - E_{p_0}}{n E_{input}}, \tag{2.36}$$

because the same amount of energy was input after each tow. As the fluid becomes less stratified Rf_n decreases as n increases. Rf at initial conditions was determined by interpolating the trends toward $n = 0$.

2.4 Length and time scales

Dimensional analysis is a powerful tool in fluid mechanics and can be used to construct an array of length and time scales. The scales reviewed in this section are measures of inertial effects, buoyancy effects, or both.

The Kolmogorov scales, discussed in Sec. (2.4.1), are the small-scale limits of the inertial energy cascade. However, when scalar diffusion is smaller than momentum diffusion, the Batchelor scale, discussed in Sec. (2.4.2), controls the small-scale limit of scalar dissipation. The Taylor microscale is an additional commonly used length scale characterizing small scale motions and is discussed in Sec. (2.4.3).

The time scales controlling the energy containing range are the buoyancy frequency,

discussed in Sec. (2.4.4), and the turbulent time scale, discussed in Sec. (2.4.5).

A variety of length scales characterizing energy-containing scales are discussed in Secs. (2.4.5)-(2.4.9). The turbulent length scale (Sec. 2.4.5) provides a large-scale limit of eddy size based solely on inertial effects. The Ozmidov scale (Sec. 2.4.6) and buoyancy scale (Sec. 2.4.7) are based on combinations of inertial and buoyancy effects. The Thorpe scale (Sec. 2.4.8) and Ellison scale (Sec. 2.4.9) are directly measured from density fields and are not based on dimensional arguements.

2.4.1 Kolmogorov scales

> Big whorls have little whorls
> That feed on their velocity,
> And little whorls have lesser whorls
> And so on to viscosity.
>
> – Lewis F. Richardson

Richardson famously described the fractal nature of turbulence in 1920, but a universal analytical governing theory describing turbulence has eluded turbulence researchers. Kolmogorov, a Russian mathematician, transformed fluid mechanics in 1941 when he proposed three hypothesis concerning the nature of turbulence. He hypothesized that energy is injected into turbulent flows at large scales and subsequently dissipated at molecular scales governed by ν, resulting in an energy cascade where energy is transfered from large scales to small scales, and finally dissipating as heat. In Kolmogorov's *first similarity hypothesis*, he argued that the small-scale motions in the dissipation range are uniquely determined by ν and ϵ_k (Kolmogorov, 1962).[1]The scales defining the lower cutoff of the dissipation range can be constructed from dimensional analysis and are widely considered to be the smallest scales of motion in turbulent flows. The Kolmogorov length, time, and velocity scales are, respectively:

$$L_\eta = (\nu^3/\epsilon_k)^{1/4} \tag{2.37}$$

$$T_\eta = (\nu/\epsilon_k)^{1/2} \tag{2.38}$$

$$u_\eta = (\epsilon_k \nu)^{1/4} \tag{2.39}$$

2.4.2 Batchelor scale

The Batchelor scale L_B (Batchelor, 1959) is the length scale characterizing the molecular diffusion of scalar properties. It is defined as

$$L_B = \left(\frac{\kappa^2 \nu}{\epsilon_k}\right)^{1/4}, \tag{2.40}$$

and is related to L_η through Pr as

$$L_\eta = L_B Pr^{-1/2}. \tag{2.41}$$

Thus, when $Pr > 1$, L_B is smaller than L_η. The Prandtl number is approximately 0.7 for heat stratification in air, 7 for heat stratification in water, and 700 for salinity stratification in water. (Thorpe, 2005)

2.4.3 Taylor microscale

The Taylor microscale is a length scale based on rather abstract correlation functions. The Taylor microscale is a statistical quantity larger than L_η but smaller than L, usually located within the $-5/3$ region of the inertial subrange. There is no clear physical interpretation of the Taylor microscale but as it is based on rigorous statistics it is commonly used to quantify numerical simulations (Pope, 2000). The transverse Taylor microscale L_λ was shown by Taylor (1935) to be related to other flow properties as

$$L_\lambda = \sqrt{\frac{5\nu \left\langle u_i u_i \right\rangle}{\epsilon_k}}. \tag{2.42}$$

2.4.4 Buoyancy frequency

Consider a particle displaced from a position of equilibrium in a continuous stably stratified fluid. A restoring force proportional to the displaced distance acts on the particle towards

[1] Although results stemming from Kolmogorov's hypothesis have been heavily validated in experiments, important questions persist, such as the nature and existence of reverse energy cascades and if dissipation is restricted solely to the dissipation subrange in the Kolmogorov energy cascade.

the equilibrium position (i.e. the position where the density of the particle is equal to the mean horizontal density). Using Archimedes' principle and decomposing density into a reference, mean, and fluctuation from the mean, the force acting on the particle can be written as

$$(\rho_o + \overline{\rho} + \rho')\frac{\partial^2 z}{\partial t^2} = -\rho'\mathbf{g}, \tag{2.43}$$

and rearranged to isolate the acceleration of the particle as

$$\frac{\partial^2 z}{\partial t^2} = -\frac{\rho'}{(\rho_o + \overline{\rho} + \rho')}\mathbf{g}. \tag{2.44}$$

If $\partial\overline{\rho}/\partial z$ is a well behaved function, the Taylor series can be used to approximate the density fluctuation as

$$\rho' = \frac{\partial\overline{\rho}}{\partial z}z', \tag{2.45}$$

where z' is the particle displacement from the equilibrium position. Assuming ρ_o is much greater than $\overline{\rho} + \rho'$, the particle acceleration becomes

$$\frac{\partial^2 z}{\partial t^2} = -\frac{\mathbf{g}}{\rho_o}\frac{\partial\overline{\rho}}{\partial z}\,dz. \tag{2.46}$$

Eq. (2.46) describes the particle motion of a displaced particle in a stratified flow where viscous and mixing effects are neglected. The behavior of this ODE is dependent on the buoyancy frequency, also known as the Brunt-Väisälä frequency,

$$N = \left[-\frac{\mathbf{g}}{\rho_o}\left(\frac{\partial\overline{\rho}}{\partial z}\right)\right]^{1/2}. \tag{2.47}$$

The solution to Eq. (2.46) for a stably stratified flow (i.e. $\partial\overline{\rho}/\partial z < 0$) using Euler's trigonometric identities is

$$dz(t) = c_1\cos(Nt), \tag{2.48}$$

where c_i is an arbitrary scalar dependent on initial conditions. From Eq. (2.48) it can be seen that the solution is oscillatory because the displaced particle is accelerated back towards the equilibrium position, but overshoots the equilibrium position due to inertial

effects. Dampening effects from mixing and viscosity will slow the acceleration and bring the particle to a stationary equilibrium position. The inviscid and zero-mixing assumptions may be unrealistic of real turbulence, but N^{-1} defines an important time scale in stratified flows and Eq. (2.46) illustrates the general behavior of particles in stably stratified flows.

For unstable stratification (i.e. $\partial\overline{\rho}/\partial z > 0$) the solution to Eq. (2.46) can be expressed as

$$dz(t) = c_2 \exp(Nt) + c_3 \exp(-Nt). \tag{2.49}$$

Unstable stratification is stored potential energy. Disturbances will release kinetic energy, resulting in an exponentially accelerating particle. Due to non-linear effects quickly becoming dominant, this solution is only valid for very small displacements (Turner, 1973). However, it neatly illustrates the general behavior of unstable stratification being a source of energy. Contrarily, stable stratification acts as a sink of energy due to restoring forces, mixing, and viscosity.

The buoyancy period T_{bv}, defined as

$$T_{bv} = 2\pi/N, \tag{2.50}$$

characterizes the period of internal waves and varies greatly depending on the flow medium. For example, in the deep ocean, the buoyancy period is of order of many hours while in the atmosphere it is of order of a few minutes (Gregg, 1987).

2.4.5 Turbulent length and time scale

Assuming stationary and isotropy, a time scale can be constructed from k and ϵ_k called the turbulent time scale T_L,

$$T_L = k/\epsilon_k. \tag{2.51}$$

The turbulent time scale T_L is a powerful scale defining the overturning period of large-scale eddies. The corresponding turbulent length scale L characterizes the size of the largest

eddies in isotropic stationary turbulence and is defined as

$$L = k^{3/2}/\epsilon_k. \tag{2.52}$$

2.4.6 Ozmidov scale

If ϵ_k and N are assumed to be the only parameters controlling the energy-containing range of the energy cascade, a length scale can be constructed as

$$L_O = \left(\frac{\epsilon_k}{N^3}\right)^{1/2}. \tag{2.53}$$

This is referred to as the Ozmidov scale, however it was independently discovered by Dougherty (1962) and Ozmidov (1965). It provides a measure of buoyancy effects, and is often interpreted as the length scale separating small scale isotropic turbulence not influenced by buoyancy from large scale anisotropic turbulence effected by buoyancy (Smyth & Moum, 2000).

2.4.7 Buoyancy scale

The vertical distance a fluid particle can travel if all vertical kinetic energy is transformed into potential energy is approximated by the buoyancy length scale, (Stillinger *et al.*, 1983)

$$L_b = \frac{w_{rms}}{N}, \tag{2.54}$$

where w_{rms} is the root-mean-square of vertical velocity.

2.4.8 Thorpe scale

The Thorpe displacement d' is the vertical distance a particle must travel back to a position along a gravitationally stable density profile. The gravitationally stable density profile is calculated by monotonically sorting the profile. The Thorpe scale L_T is the root-mean-square of non-zero d' along a vertical profile and provides a measure of the size of vertical overturns (Thorpe, 1977). The procedure to calculate L_T from density profiles is explained

further in Appx. (B.1).

The gravitationally stable density profile is vertically stable, but may not be horizontally stable. When three-dimensional density fields are vertically sorted, strong horizontal gradients (and instability) can exist as d' is only a measure of vertical stability. Thus, to account for horizontal stability a three-dimensional sorting process can be used to construct a 3D Thorpe scale L_{T3D}. The procedure to calculate L_{T3D} is explained in Appx. (B.2). In contrast to L_T, L_{T3D} is a measure of general scalar displacements and is influenced by internal waves (Tseng & Ferziger, 2001).

2.4.9 Ellison scale

The Ellison scale L_E is an additional measure of the maximum vertical displacement, given a background density profile and a turbulent intensity estimated by $\frac{1}{2}\overline{\rho'^2}$,

$$L_E = \frac{\frac{1}{2}\overline{\rho'^2}}{\partial\overline{\rho}/\partial z}. \tag{2.55}$$

If the sorted density profile is exactly equal to $\partial\overline{\rho}/\partial z$, then L_E is exactly equal to L_T. The Ellison scale is a useful parameter because it can be related to the turbulent potential energy as $L_E = -E_p\rho_o/\mathbf{g}$.

2.5 Non-dimensional parameters

The main non-dimensional parameters of stratified turbulence are relative measures of inertia, viscosity, buoyancy, and shear. This work only considers decaying turbulence, shortening the list to inertia, viscosity, and buoyancy. The strength of stratification is quantified with relative measures of buoyancy and inertia using the initial Richardson number and turbulent Froude number, discussed in Sec. (2.5.1). The Reynolds number is a relative measure of inertial to viscous effects. A variety of Reynolds numbers based on different length scales are discussed in Sec. (2.5.2). Similar to the Reynolds number, the Peclet number is a relative measure of inertial effects to scalar diffusivity and is also discussed in Sec. (2.5.2). The buoyancy Reynolds number, discussed in Sec. (2.5.3), is a mixed parameter and is a

measure of inertial, viscous, and buoyancy effects.

2.5.1 Initial Richardson number and Froude number

For decaying turbulence an initial Richardson number[1] Ri can be constructed from the buoyancy time scale N^{-1} and the initial eddy turnover time scale $T_0 = L_0/u_0$ as

$$Ri = \left(\frac{NL_0}{u_0}\right)^2. \tag{2.56}$$

Ri is used to define the background stratification of different runs.

The turbulent Froude number Fr is a measure of the relative importance of inertial effects to buoyancy (i.e. gravitational effects). The turbulent Froude number can be constructed using the turbulent times scale T_L and the buoyancy frequency N, such that

$$Fr = \frac{\epsilon_k}{Nk}. \tag{2.57}$$

2.5.2 Reynolds number and Peclet number

The Reynolds number is the ratio of inertial effects to viscous effects. The initial Reynolds number Re_0 defined from initial velocity and length scales is

$$Re_0 = \frac{u_0 L_0}{\nu}. \tag{2.58}$$

This form of the Reynolds number is used to defined the value of ν in the DNS code.

Using the turbulent length scale L, the turbulent Reynolds number Re_L can be constructed as

$$Re_L = \frac{k^{1/2}L}{\nu} = \frac{k^2}{\epsilon_k \nu}. \tag{2.59}$$

The Peclet number is the ratio of inertial effects to molecular diffusion. Using the turbulent

[1]Similar to Ri, the gradient Richardson number $Ri_g = N^2/S^2$ characterizes the relative strength of stratification to shear. Large Ri and $Ri_g > 1$ indicate strong stratification.

length scale L, the turbulent Peclet number Pe_L is similarly defined as

$$Pe_L = \frac{k^2}{\epsilon_k \kappa}, \tag{2.60}$$

and can be related to Re_L as $Pe_L = Re_L Pr$.

Using the Taylor microscale L_λ, a statistical quantity, a Taylor Reynolds number can be defined as

$$Re_\lambda = \frac{u_{rms} L_\lambda}{\nu}. \tag{2.61}$$

There is no clear physical interpretation of Re_λ, but as it has a rigorous definition and is widely used in DNS studies it allows for comparisons with other works.

2.5.3 Buoyancy Reynolds number

The buoyancy Reynolds number quantifies the energy level of stratified flows and is defined as

$$R_b = \frac{\epsilon_k}{\nu N^2}. \tag{2.62}$$

It is commonly used in oceanography because it is absent of kinetic energy, a difficult parameter to measure. R_b is a mixed parameter and not a true a Reynolds number as it includes buoyancy effects in addition to inertia and viscosity. Ivey *et al.* (2008) describe it as the "ratio of destabilizing effects of turbulent stirring to the stabilizing effects from combined action of buoyancy of viscosity." It can be constructed from the Ozmidov scale L_O (a measure of inertia and buoyancy) and the Kolmogorov length scale L_η (a measure of viscosity), such that

$$R_b = \left(\frac{L_O}{L_\eta} \right)^{4/3}. \tag{2.63}$$

The ratio L_O/L_η is the intermittency factor (Thorpe, 2005) and can be interpreted as the the bandwidth of length scales available to isotropic turbulence (Gregg, 1987). Similarly, the turbulent Reynolds number can be written as

$$Re_L = \left(\frac{L}{L_\eta} \right)^{4/3}, \tag{2.64}$$

where L/L_η is a measure of the total bandwidth of length scales available to turbulence. Thus, R_b is referred to as the 'buoyancy Reynolds' rather than the also commonly used 'turbulence activity parameter'.

2.6 Direct Numerical Simulations

Turbulence is characterized by a large range of length scales, where energy is input at the large scales while dissipation occurs at the smallest scales. Modeling this chasm of scales is incredibly computationally expensive and gives rise to the famous (or infamous) 'turbulence problem'. Most Computational Fluid Dynamics (CFD) methods use turbulence models to estimate small scale turbulence allowing the resolution to be limited to scales relevant to the particular engineering or geophysical problem of interest. DNS is an exact numerical solution attained by resolving all scales of motion, thus bypassing the turbulence problem. DNS is an important tool because it can be used to investigate properties of turbulent flows which cannot be investigated with conventional theoretical or experimental methods. First theorized by John Von Neumann in 1949 (Davidson, 2004), DNS is the simplest form of numerical simulations. To resolve all scales of motion, the grid size must be of order of the Kolmogorov length scales L_η while the domain length $\mathcal{L}$ must be large enough to capture the largest energy containing eddies (Pope, 2000).

The turbulent Reynolds number Re_L (Eq. 2.59) can be used to illustrate the computational cost associated with large simulations. The number of grid points in one direction N is approximately equal the ratio of the turbulent scale L to the Kolmogorov scale L_η so that N scales as (Durbin & Pettersson Reif, 2011)

$$N \sim \frac{L}{L_\eta} = \frac{k^{3/2}}{\epsilon_k}\left(\frac{\epsilon_k}{\nu^3}\right)^{1/4} = \left(\frac{k^2}{\epsilon_k \nu}\right)^{3/4} = Re_L^{3/4}. \tag{2.65}$$

To resolve all length scales in all three spatial directions N^3 must scale as $Re_L^{9/4}$ (Rogallo & Moin, 1984).

To ensure accurate time advancement, Courant number restrictions for isotropic turbu-

lence have been found to be

$$C \equiv \frac{k^{1/2}\Delta t}{\Delta x} = \frac{1}{20}. \tag{2.66}$$

If the duration of the simulations in this work are $10T_L$, the total number of time steps M scales as

$$M \sim \frac{10T_L}{\Delta t} = 200\frac{k^{3/2}}{\epsilon_k}\left(\frac{\epsilon_k}{\nu^3}\right)^{1/4} = 200\left(\frac{k^2}{\epsilon_k \nu}\right)^{3/4} = 200Re_L^{3/4}. \tag{2.67}$$

The number of floating-point operations is proportional to the product of grid points (or modes) and timesteps. The computational requirements therefore scale as

$$N^3 M \sim 200Re_L^3. \tag{2.68}$$

It is daunting to use DNS for moderate Reynolds numbers and simply impossible for geophysical flows at present and the foreseeable future. The highest resolution DNS of decaying turbulence achieved to date were performed by Kaneda & Ishihara (2006). Using a domain size $N = 4096$ on a super computer they achieved $Re_\lambda = 1200$. Although DNS is the simplest and most general CFD method, it only provides insight into physics of small-scale fluid mechanics and is rarely used outside academia (Pope, 2000). However, it is an essential tool for developing and validating subgrid turbulence models implemented in LES and RANS models.

2.6.1 Description of code

Orszag & Patterson pioneered pseudo-spectral methods in 1972, which have been the preferred method of DNS due to high computational accuracy and efficiency. The pseudo-spectral DNS code used in this work for continuously stratified turbulence is an extension of the method described by Orszag & Patterson (1972), and was developed by Riley, Metcalfe & Weissman (1981). The code was written in the FORTRAN 77 programming language as a serial code. Algorithms to compute wavenumber space operations and Fourier transforms using parallel processors are very complex (Pope, 2000) and have therefore not been implemented in this code. The code used in this work is further discussed in Appx. (A).

A pure spectral method requires very small time steps to satisfy the Courant number (Eq. 2.66). Pseudo-spectral methods compute terms in both wavenumber and physical space, so that linear terms of the non-dimensional governing equations (Eqs. 2.8-2.10) are computed in wavenumber space, while the non-linear time-advancing advection terms are computed in physical space.

Parameters, such as velocity, can be defined in wavenumber space as three-dimensional finite Fourier series for N^3 Fourier modes as

$$\mathbf{u}(\mathbf{x},t) = \sum_{\boldsymbol{\kappa}} e^{i\boldsymbol{\kappa}\cdot\mathbf{x}}\hat{\mathbf{u}}(\boldsymbol{\kappa},t). \tag{2.69}$$

Discrete Fourier Transforms (DFT) is the one-to-one mapping of parameters between wavenumber and physical space, meaning that the number of wavenumbers are truncated to N. The product of two three-dimensional parameters in wavenumber space is a summation of all triad interactions requiring N^6 operations. In contract, the product of two three-dimensional parameters in physical space requires only N^3 operations. A convolution sum is the product of two Fourier series in physical space (Durbin & Pettersson Reif, 2011). The Cooley-Tukey Fast Fourier Transform (FFT) (Cooley *et al.*, 1970) is a powerful DFT algorithm for convolution sums requiring of order $N^3 \log N$ operations. The non-linear advection terms are computed in physical space using a leap-frog scheme, except for every 25^{th} time step an Euler scheme is used in-place for numerical smoothing. The non-linear diffusion terms are also computed in physical space using an implicit Crank-Nicolson scheme (Riley *et al.*, 1981).

The Cooley-Tukey FFT requires N to be a power of 2. The length of the domain is $\mathcal{L} = 2\pi/(L_0\kappa_0)$ where $L_0 = 1$ so that wavenumbers are integers. The simulations are set such that the lowest wavenumber k_0 is 2 making $\mathcal{L} = \pi$ and the highest wavenumber $\kappa_{max} = N$. The Cooley-Tukey FFT also requires periodic boundary conditions, which is conducive to DNS by allowing eddies to travel continuously through the domain (Pope, 2000).

2.6.2 Initial conditions

The simulation was initialized as a Gaussian random isotropic velocity field. The initial velocity field is defined with an energy spectrum function as

$$E(\kappa) = C u_0^2 L_0^5 \kappa^4 e^{-\frac{1}{2}\kappa^2 L_0^2}, \tag{2.70}$$

where C is a constant, and u_0 and L_0 are initial characteristic velocity and length scales.

2.6.3 Rapid-Distortion Theory

When turbulent flows become sharply anisotropic, such as boundary layer flows or flows over bluff bodies (Townsend, 1980), eddies become distorted as they evolve. The distortion may be small vortical structures in high Reynolds number flows or large coherent structures which span entire flow domains (Hunt & Kevlahan, 1993). Stratification introduces axisymmetric anisotropy due to buoyancy forces retarding vertical motions by quickly distorting eddies. The resulting eddies are mostly horizontal (e.g. see Fig. 3.15). When distortion occurs on a time scale much shorter than the eddy life time T_L, the equations of motion can be linearized using RDT (Durbin & Pettersson Reif, 2011). Using very high resolution DNS of homogeneous turbulence, Kaneda & Ishihara (2006) found the life-span of isotropic vortex tubes to be approximately T_L. RDT is not a turbulence model, but rather can be used in conjunction with turbulence theory and has been an insightful tool to study non-linear and multi-scale dynamics of turbulence (Hunt & Kevlahan, 1993).

There are numerous linearization methods using RDT assumptions. The simplest method is neglecting the non-linear terms in the governing equations, which is essentially an inviscid approximation. Inviscid flow implies an infinitely large Reynolds number, which for small and moderate Reynolds number flows grossly neglects the fundamental behavior of turbulent flows. However, Kaneda & Ishida (2000) found that certain statistics from RDT correlated well with DNS for strong stratification at low Reynolds numbers.

Chapter 3

Dynamics and Structure

3.1 Introduction

The dynamics and structure of stratified turbulence was studied using two DNS parametric studies to explore varying levels of stratification, Prandtl numbers, and Reynolds numbers. The main questions addressed in this section are:

(i) What are the dynamics of decaying stratified turbulence at high Reynolds numbers?

(ii) What coherent turbulent structures emerge from simulation of decaying stratified turbulence?

(iii) What is the dependence of mixing efficiency on stratification, the Reynolds number, and the Prandtl number, and how do trends compare with physical experiments?

(iv) Can Rapid-Distortion Theory (RDT) be used to explain Prandtl number effects?

In Sec. (3.2) resolution issues are discussed and DNS results are validated with previous work. The energetics and dynamics of the flow are explored in Sec. (3.3). To understand the behavior of stratified turbulence and the limitations of DNS the results are plotted with R_b and Ri regimes in Sec. (3.4). The nature and behavior of coherent vortex structures are discussed in Sec. (3.5). Physical and numerical experiments are compared in Sec. (3.6). Multiple RDT studies are performed in Sec. (3.7) to further explore Prandtl number and Reynolds number trends outside DNS constraints. Additionally, RDT is used to illustrate the decoupling between horizontal and vertical dynamics at strong stratification.

3.2 Validation

Results from the DNS code used in this work have been previously published in Riley *et al.* (1981), Venayagamoorthy & Stretch (2006), and Stretch *et al.* (2010). Simulations in this

work are performed with a domain resolution $N = 256$, which is 8 times larger than the previous highest published resolution by Stretch *et al.* (2010) with $N = 128$. The numerical accuracy of the code at lower resolutions has been thoroughly verified in multiple studies. It is important that results are thoroughly validated because the code was modified for higher resolution and a different output format was implemented.

To ensure the code is producing realistic physics the energy cascades are analyzed in Sec. (3.2.1). Simulations are compared with previous work for a range of Pr, Ri, and domain sizes in Sec. (3.2.2).

3.2.1 Resolution issues

To obtain an exact solution to the flow it is fundamentally important that all scales are fully resolved. The kinetic energy spectrum, or energy cascade, is a valuable tool to investigate resolution. Energy cascades of fully turbulent flows contain three important ranges. The energy-containing range (E) is the large scale range where energy is injected into the energy cascade through large eddies. The dissipation subrange (D) is the small scale range where energy is dissipated due to viscosity as heat. The inertial subrange is the range where length scales are hypothesized to be transported from E to D without further production.

The model spectrum is the theoretical kinetic energy spectrum normalized with the Kolmogorov scales, where I classically scales to the $-5/3$ power. A model spectrum of turbulent flow with $Re_\lambda = 500$ is shown in Fig. (3.1). In diffusive flows energy is conveyed directly from E to D and do not contain a clear I. The presence of I is a fundamental diagnostic to distinguish between turbulent and diffusive flows. The energy cascades for weak, moderate, and strong stratification are plotted in Fig. (3.2). The plotted energy cascades are shown at the decay point (i.e. at peak ϵ_k) where the flow is most turbulent.

The Kolmogorov length scale L_η is based on the similarity hypothesis that turbulence has a universal form and is uniquely defined by ϵ_k and ν. It does not define the exact transition between I and D but rather where D begins to roll-off to rapidly decreasing energy. It is commonly used as an approximate lower limit of the energy cascade because energetics below L_η quickly become negligible. Yeung & Pope (1989) and Kaneda & Ishida (2000)

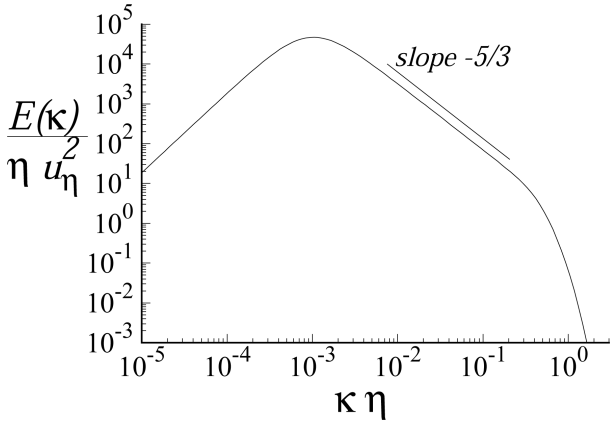

Figure 3.1: Model spectrum - The model spectrum of the energy containing range (E), the inertial subrange (I), and the dissipation range (D). Turbulent flows are characterized by the presence of an inertial subrange which scales to the $-5/3$ power. Figure adapted from Pope (2000).

found that $\kappa_{max} L_\eta > 1.5$ is an adequate resolution to compute higher order statistics. For the main DNS study (summarized in Table A.1), $\kappa_{max} L_\eta$ ranged from 1.044 at $Ri = 0.01$ to 1.614 at $Ri = 1000$. No higher order statistics were computed; thus it was deemed L_η is adequately resolved in all runs for the given scope of work. When $Pr > 1$ it is important that the Batchelor scale L_B is also resolved. Runs were performed with $Pr = 2$ resulting in $\kappa_{max} L_B$ ranging from 0.739 at $Ri = 0.01$ to 0.962 at $Ri = 1000$. An unresolved L_B may lead to underestimation of the buoyancy flux (Oduyemi, 1993). It was deemed $Pr = 2$ is adequatly resolved because the focus of this work is on turbulence at high Ri and no anamalous trends were observed.

Five relevant length scales are plotted in Fig. (3.2) with the energy cascades. The turbulent length scale L characterizes large, isotropic eddies and is not spectrally resolved in the energy cascade. However, for weak stratification L is equal to or smaller than L_0 and retains physical interpretation as the largest eddies. The turbulent length scale is discussed further in Sec. (4.3.4). Depending on Pr, L_η or L_B mark the small scale cutoff. In Fig. (3.2), L_η defines the small scale limit because $Pr = 0.5$ resulting in $L_B > L_\eta$. Regions with $-5/3$ power scaling are limited signifying I is small or absent. The Taylor microscale L_λ generally lies within I. However, in Fig. (3.2) L_λ appears to mark an upper cutoff of I and is further evidence that I is very small or non-existant. The Ozmidov scale L_O marks the approximate

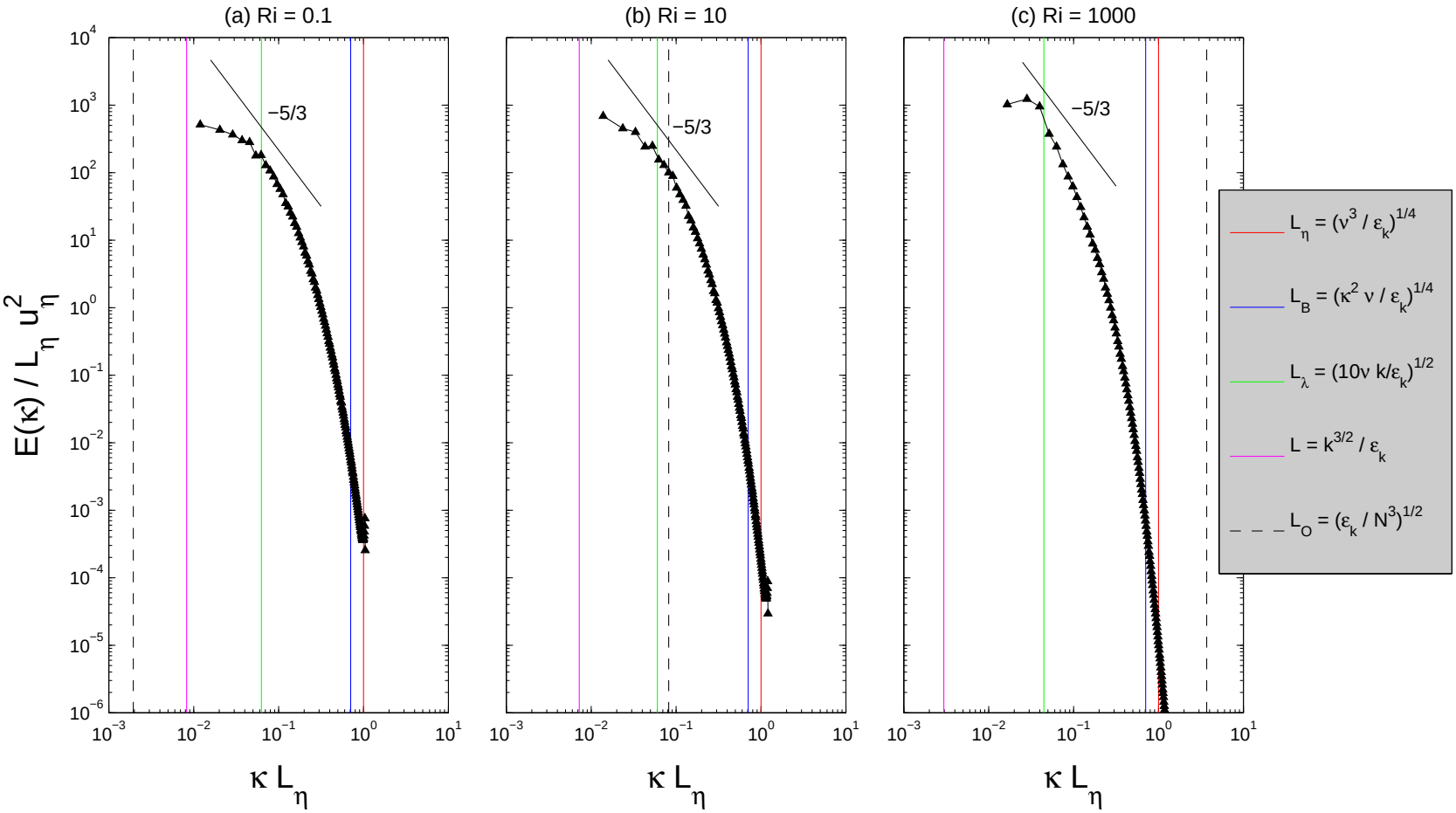

Figure 3.2: Energy cascades with length scales - The three-dimensional mean energy cascade at the decay point (i.e. when ϵ_k peaks) with $Pr = 0.5$ are plotted for weak, moderate, and strong stratification. The presence of the inertial subrange (I), which scales to the $-5/3$ power, is a key diagnostic to determine if a flow is turbulent or laminar. For all three cases there is no clear separation of scales meaning large scales interact directly with small scales, as occurs in diffusive flows.

transition between isotropic and anisotropic turbulence. The length scales larger than L_O are influenced by buoyancy, and therefore anisotropic. Scales smaller than L_O are not influenced by buoyancy and the turbulent statistics are considered spatially isotropic. Also, Kolmogorov's hypothesis of local isotropy required D to be isotropic (Kolmogorov, 1962). In Fig. (3.2a), no scales are influenced by buoyancy because L_O is larger than the domain length $\mathcal{L}$ and the turbulence can be considered fully isotropic. In Fig. (3.2b), L_O is located in the center of the energy cascade and neatly separates the large, buoyancy influenced scales from the small, isotropic scales. In Fig. (3.2c), L_O are much smaller than L_η, and implies that all scales are buoyancy controlled and anisotropic. However, this contradicts Kolmogorov's hypothesis of local isotropy and implies L_O loses traditional interpretation for strongly stratified and diffusive flows.

The presence of large bumps in the energy cascade signify numerical errors. The bumps present at the tail-end in Fig. (3.2) for cases of weak and moderate stratification are exaggerated by the logarithmic scale and are very small. The source of the bumps could be either a form of numerical feedback or a product of anti-aliasing in Fourier transforms as low wavenumbers are truncated following convolution sums. Venayagamoorthy (2002) noted similar behavior and deemed spatial resolution to be adequate.

3.2.2 Comparison with previous work

Simulations are compared with previously published lower-resolution results using the same DNS code. The flux Richardson number Rf is calculated using Eq. (2.31), the same method previously used. To investigate grid independence, Rf is plotted in Fig. (3.3) with domain sizes ranging from $N = 32$ to 256. Rf are compared with $N = 64$ results from Venayagamoorthy (2002) in Fig. (3.4) for varying Ri and Pr.

In Fig. (3.3), Rf increases as grid resolution increases. This trend may be a result of varying initial conditions and/or Reynolds numbers. The relationship between Rf and Reynolds number is explored further in Sec. (3.7.2). In Fig. (3.4), the differing trends at high Ri is an error resulting from calculating Rf using Eq. (2.31), which requires $\Delta k \to 100\%$ for convergence. Venayagamoorthy (2002) found that $10T_0$ simulation durations were sufficient

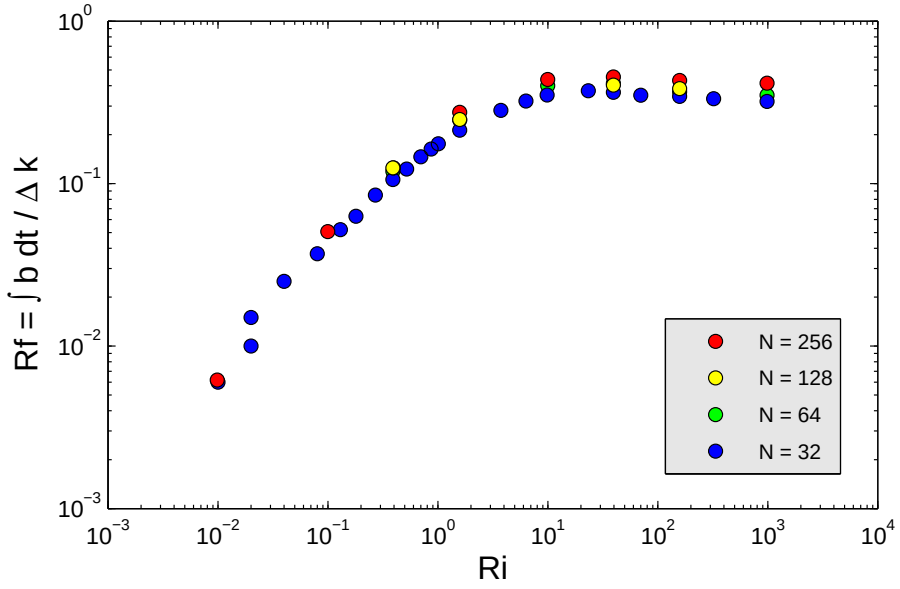

Figure 3.3: Grid independence - Flux Richardson numbers Rf versus Ri for domain sizes ranging from $N = 32$ to 256 with $Pr = 0.5$. Lower resolution results are from Venayagamoorthy (2002) and Stretch *et al.* (2010).

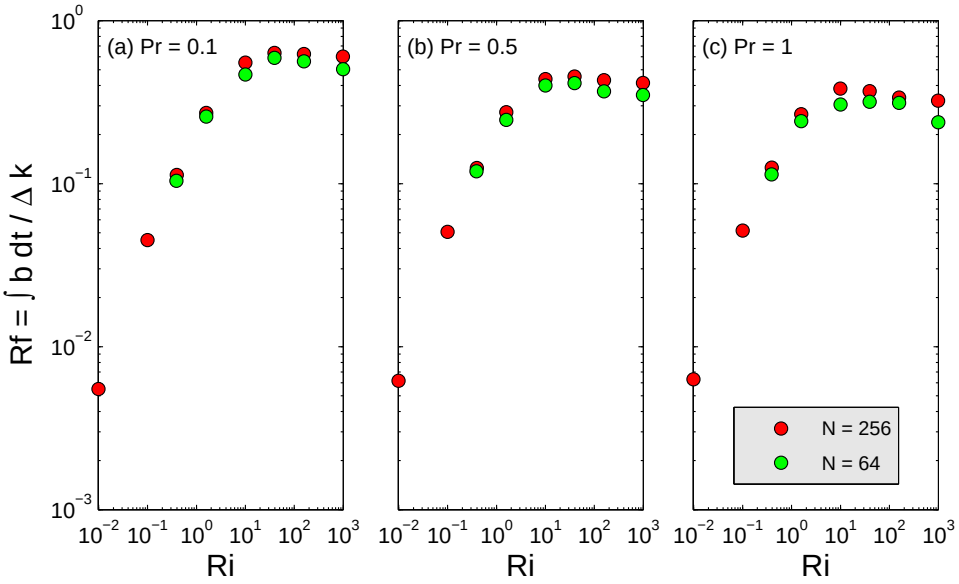

Figure 3.4: Validation with Ri and Pr variation - Flux Richardson numbers Rf versus Ri for $N = 64$ from Venayagamoorthy (2002) and for $N = 256$ from this work.

for at least 95% of k to be dissipated and Rf to converge. In this work, strongly stratified simulations did not achieve sufficient dissipation of k for convergence (e.g. $Ri = 1000$ and $Pr = 1$ resulted in 85% dissipation of k; see Table A.1). A different formulation of Rf which does not require long run times for convergence is discussed in Sec. (3.3.4).

3.3 Dynamics and energetics

The dynamics of stratified turbulence is studied for a range of stratification. Weak stratification corresponds with $Ri = 0.1$, moderate stratification with $Ri = 10$ and strong stratification with $Ri = 1000$. Energetics and dissipation rates are explored in Secs. (3.3.1)-(3.3.2). Reynolds numbers are discussed Sec. (3.3.3) and multiple formulations of Rf are compared in Sec. (3.3.4).

3.3.1 Energetics

The ensemble-average evolution of total energy E_T, potential energy E_p, and kinetic energy k are plotted in Fig. (3.5). The simulations are initialized with a turbulent kinetic energy field and a buoyancy flux field equal to zero. Thus, E_p is initially zero and increases as the flow evolves. E_T gradually decreases for all time while the buoyancy flux transfers energy between kinetic and potential forms. There is a stark increase in E_p between $Ri = 0.1$ and $Ri = 10$ but E_p relative to E_T does not drastically change between $Ri = 10$ and $Ri = 1000$.

The external gravity force is only manifested in the governing equations through the buoyancy flux b in the vertical Navier-Stokes equation. The oscillatory behavior of k and E_p in Figs. (3.5b) and (3.5c) is a result of b being governed by the time scale N^{-1}. There is no oscillatory exchange of energy in Fig. (3.5a) because the buoyancy period T_{bv} is greater than the duration of the event.

For stratified flows, k is reduced by the kinetic energy dissipation rate ϵ_k (an irreversible process) and b (a reversible process). As stratification increases, b fluxes more energy between k and E_p, resulting in a more inefficient decay process. Thus, as stratification increases more energy remains at later times in Fig. (3.5).

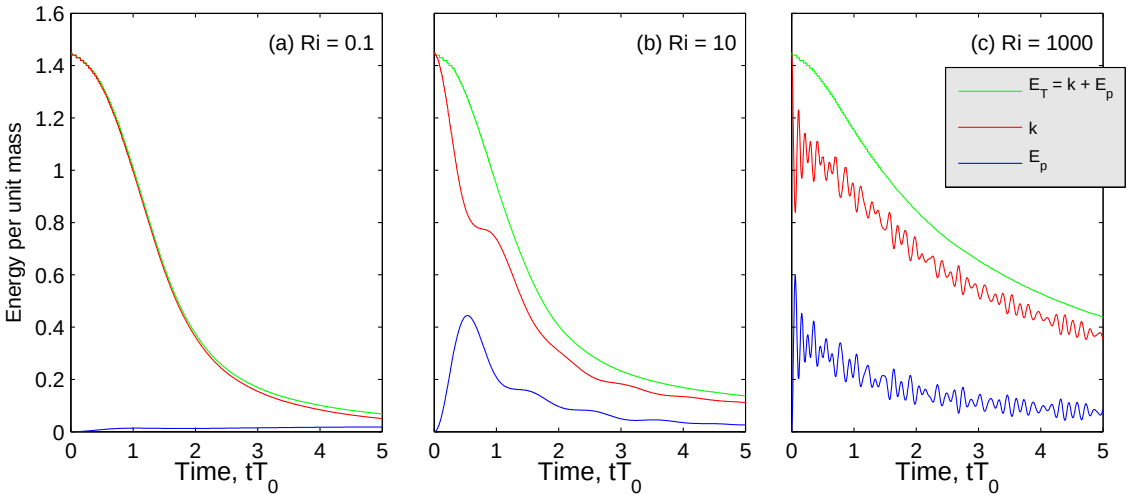

Figure 3.5: Evolution of ensemble-average energetics - The total energy decays for all times during which energy is transfered between kinetic and potential forms through the buoyancy flux. There is no oscillation in (a) because the buoyancy period T_{bv} is greater than the duration of the event. The oscillations in (b) and (c) are govererned by the buoyancy frequency N.

Horizontal motions are affected by b only through coupling of horizontal and vertical dynamics. As stratification increases, b becomes increasingly dominant and restricts vertical motions. To illustrate the reduced vertical motions, the proportion of horizontal and vertical kinetic energy to total kinetic energy are plotted in Fig. (3.6). For isotropic turbulence, k should be equi-partitioned in all spatial directions; i.e. the horizontal kinetic energy k_H should be $\frac{2}{3}E_T$ and the vertical kinetic energy k_V should be $\frac{1}{3}E_T$. As stratification increases to $Ri = 1000$ in Fig. (3.6c) k_V/k decreases to 0.1 and k_H/k increases to 0.9, which illustrates the strong anisotropic behavior of stratification.

3.3.2 Dissipation

Energy dissipation rates are plotted in Fig. (3.7) for weak, moderate, and strong stratification. The dissipative processes of stratified turbulence are strongly dependent on the degree of stratification. After initial conditions, the dissipation rates increase until the decay point, which occurs at approximately one eddy turnover.

The weakly stratified case (i.e. $Ri = 0.1$) corresponds with a very low potential energy dissipation rate ϵ_p and the total and kinetic energy dissipation rates (ϵ_T and ϵ_k, respec-

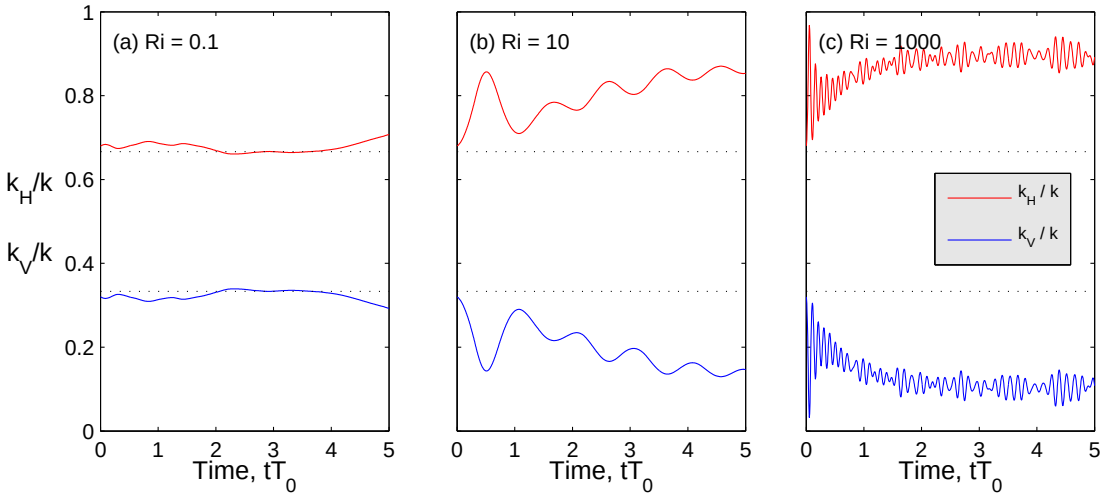

Figure 3.6: Horizontal and vertical kinetic energy - The turbulent kinetic energy $k = \frac{1}{2}\overline{u_i' u_i'}$ consists of horizontal and vertical components. For isotropic turbulent the horizontal kinetic energy k_H should be equi-partitioned between all spatial directions; i.e. the horizontal kinetic energy k_H should be $\frac{2}{3}E_T$ and the vertical kinetic energy k_V/k should be $\frac{1}{3}E_T$. The reduced vertical kinetic energy as stratification increases illustrates the anisotropic behavior of stratification.

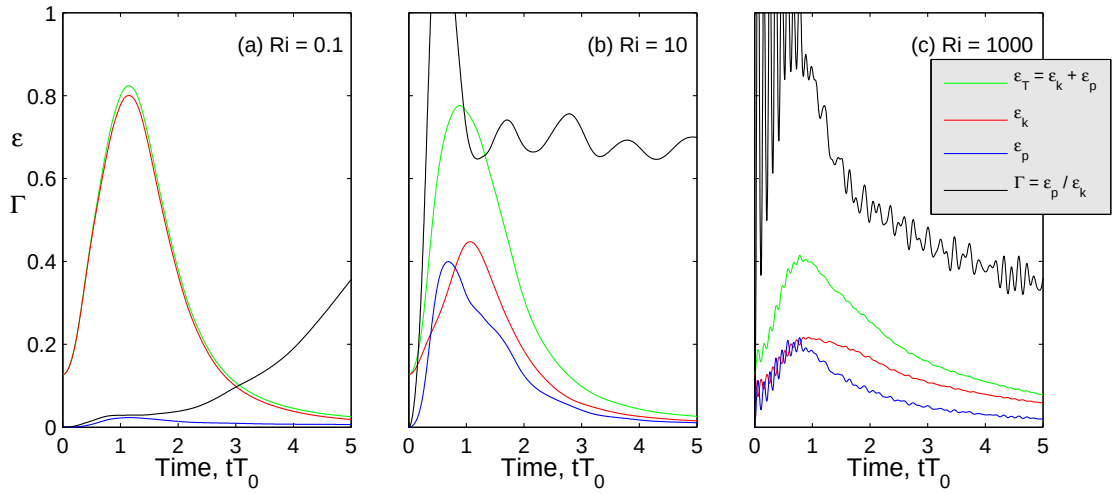

Figure 3.7: Evolution of dissipation rates - The total energy dissipation rate ϵ_T, the kinetic energy dissipation ϵ_k, and the potential energy dissipation ϵ_p are plotted over time. The instantaneous mixing efficiency Γ provides a measure of the irreversible conversion of kinetic energy into potential energy.

tively) are approximately equal. The kinetic and potential energy dissipation rates are approximatly equal for $Ri = 10$ and $Ri = 1000$. The total dissipation rate ϵ_T in Figs. (3.7a) and (3.7b) are approximately equal because ϵ_p increases and compensates for ϵ_k decreasing. The peak total dissipation rate ϵ_T in Fig. (3.7c) is significantly lower because ϵ_p is greater prior to the decay point. However, higher dissipation rates are sustained at later times. The result is that more kinetic energy remains at later times as stratification increases because ϵ_k decreases (see Fig. 3.5).

The mixing efficiency gives a relative measure of the irreversible conversion of kinetic energy into potential energy (Venayagamoorthy & Stretch, 2010). After the decay point, the instantaneous mixing efficiency Γ is highest for $Ri = 10$ because $\epsilon_k \approx \epsilon_p$ and is lowest for $Ri = 0.1$ because ϵ_p is close to zero. The oscillations of Γ are attributed to intermittency in the flow because the buoyancy flux should be independent of dissipation rates.

3.3.3 Taylor and turbulent Reynolds numbers

The turbulent Reynolds number Re_L is a classic parameter that has often been used to characterize turbulent flows. The Taylor Reynolds number Re_λ is a parameter with less physical meaning than Re_L, but is used extensively in literature because it is has a strong statistical foundation. The time evolution of both Reynolds numbers are plotted in Fig. (3.8). The results suggest stronger stratification corresponds with higher Reynolds numbers given equal initial conditions.

As turbulence decays after the initial burst of turbulent kinetic energy, it was thought that the Reynolds numbers would initially increase, then decrease after approximately one eddy turnover time T_0. However, Re_L is initially $10,243$ and Re_λ is initially 262, both of which are unrealistically high given the resolution restrictions of DNS. The peak dissipation rates at the decay point signify that the turbulence has fully developed and is momentarily stationary. Thus, the Reynolds numbers prior to the decay point have little physical significance and are ignored. The peak Reynolds numbers representative of the flow are assumed to occur at the decay point, defined as where ϵ_k peaks, and are plotted Fig. (3.8) as circle markers. All Re_λ and Re_L values presented in this work are the values at the decay point.

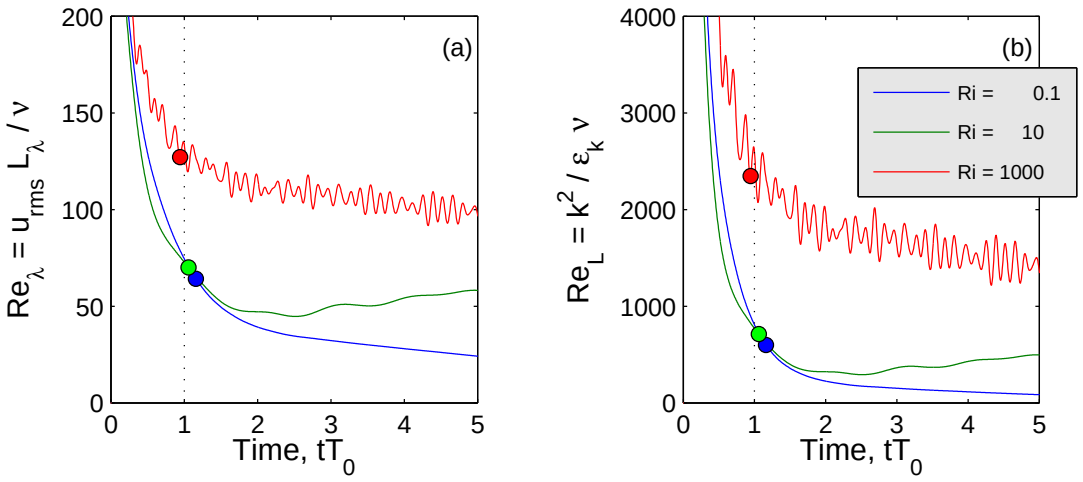

Figure 3.8: Evolution of Reynolds numbers - The Taylor Reynolds number Re_λ and turbulent Reynolds number Re_L are plotted as a function of time. Maximum Reynolds number are assumed to occur at the decay point (i.e. at peak ϵ_k) and are plotted as circle markers. All decay points occur at approximately one eddy turnover time.

3.3.4 Formulations of flux Richardson number

Multiple formulations of Rf are described in Sec. (2.3). Previous work (Venayagamoorthy, 2002; Stretch *et al.*, 2010) calculated Rf as

$$Rf = \frac{\int b\, dt}{\Delta k}, \tag{2.31}$$

where Δk is evaluated as $(k_0 - k_{final})$. Because there is no production, Δk should be equal to $\int (\epsilon_k + b)\, dt$, allowing Rf to be written as

$$Rf = \frac{\int b\, dt}{\int (\epsilon_k + b)\, dt}. \tag{2.30}$$

Venayagamoorthy (2002) found $\int b\, dt$ to converge with $\int \epsilon_p\, dt$ within $10T_0$. $\int b\, dt$ and $\int \epsilon_p\, dt$ are similarly plotted in Fig. (3.9). For $Ri = 10$ and $Ri = 1000$ the solutions converge rapidly. Given $\int \epsilon_p\, dt \approx \int b\, dt$, Eq. (2.30) can be rewritten as

$$Rf = \frac{\int \epsilon_p\, dt}{\int \epsilon_k\, dt + \int \epsilon_p\, dt}. \tag{2.32}$$

The three formulations of Rf are plotted in Fig. (3.10). The two formulations of Rf

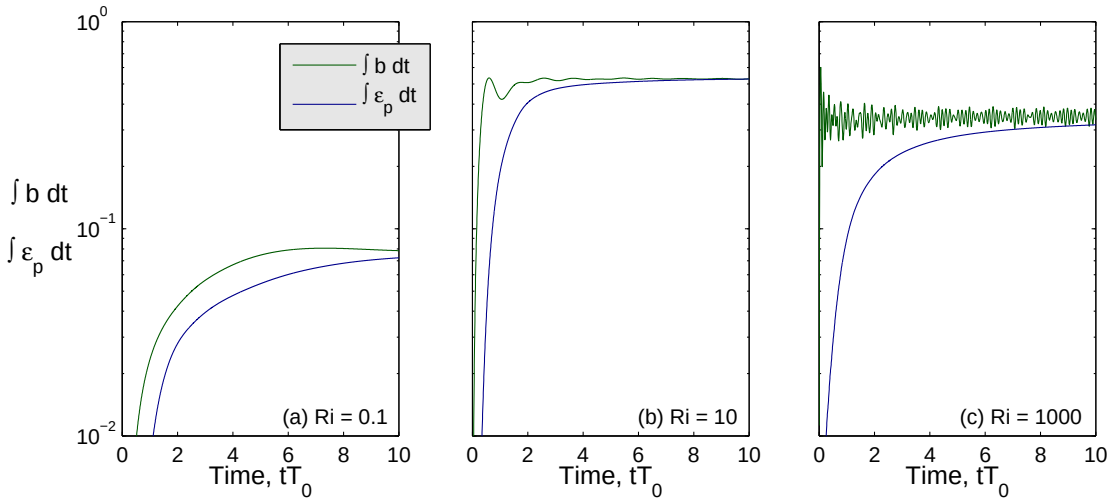

Figure 3.9: Integrated buoyancy flux and potential energy dissipation rate - At later times $\int b\,dt$ converges with $\int \epsilon_p\,dt$ allowing $\int \epsilon\,dt$ to be substituted with $\int b\,dt$ to reformulate Rf.

with reversible fluxes (i.e. Eqs. 2.30 and 2.31) are equal, confirming the substitution of Δk with $\int(\epsilon_k + b)\,dt$ is appropriate. All Rf converge at later times, but for $Ri = 10$ and 1000 Eq. (2.32) converges within approximately $1T_0$. For moderate and strong stratification, Eq. (2.32) is the most useful formulation of Rf because it converges rapidly and is absent of fluctuations from reversible effects. Conversely, for $Ri = 0.1$ the formulations with reversible fluxes appear to converge slightly faster. The focus of this work is on moderate and strong stratification, making Eq. (2.32) an appropriate formulation of Rf for the remainder of this work.

3.4 Flow regimes

The buoyancy Reynolds number R_b and mixing efficiency are insightful parameters to quantify turbulence. Mixing efficiency regimes defined by Rehmann & Koseff (2004) are discussed in Sec. (3.4.1). How results fit R_b regimes defined by Shih *et al.* (2005) are discussed in Sec. (3.4.2). The mixing efficiency and R_b regimes are combined in Sec. (3.4.3) to illustrate the resolution limitations of current DNS results and goals for further work.

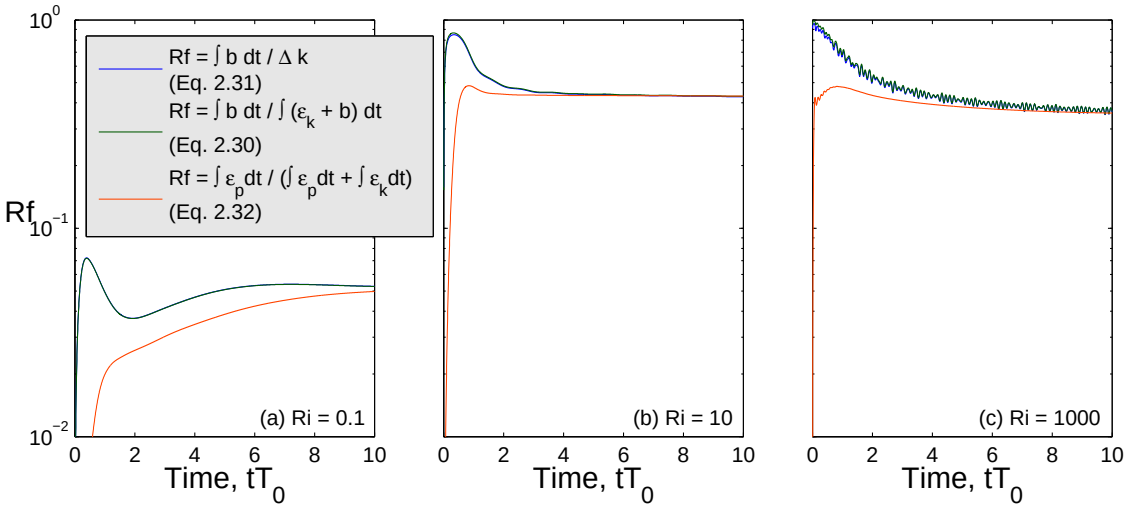

Figure 3.10: Comparison of mixing efficiency formulations - The two formulations of Rf with reversible fluxes are approximately equal. Given that $\int \epsilon_p \, dt \approx \int b \, dt$, Eq. (2.32) is a more useful formulation for moderate and strong stratification because it converges rapidly and lacks oscillatory noise from reversible effects.

3.4.1 Scaling regimes of mixing efficiency

Rehmann & Koseff (2004) performed a series of grid tow experiments to measure mixing efficiency. Their results neatly divided into three distinct regimes; weak stratification where $Ri < 0.1$, moderate stratification where $0.1 < Ri < 10$, and strong stratification where $Ri > 10$. The regimes are based on scaling of Rf versus Ri. The following dimensional arguments follow Venayagamoorthy (2002) to explain the different scalings regimes of Rf[1].

In Sec. (3.3.1) it was shown that the majority of energy in weak and moderate stratification is dissipated within $3T_0$, which will be deemed the active mixing period. In weak stratification, the buoyancy period T_{BV} is less than 1 so that $Nt < 1$ for the entire duration of the event. If the turbulence is assumed not to be affected by buoyancy, then displacements of particles z' are of order $w'T_0$. The density fluctuations ρ' therefore scale as

$$\rho' = z' \frac{\partial \overline{\rho}}{\partial z} \sim w' T_0 \left| \frac{\partial \overline{\rho}}{\partial z} \right| . \tag{3.1}$$

[1]See Rehmann (2004) for scaling arguements specific to grid-tow experiments.

Using ρ' from above, the buoyancy flux $b = \overline{\rho' w'} g/\rho_o$ scales as

$$b \sim (w'^2 T_0) \left| \frac{\partial \overline{\rho}}{\partial z} \right| \frac{g}{\rho_o} = w'^2 N^2 T_0. \tag{3.2}$$

As $Rf = \int b\, dt/\Delta k$ and dt is assumed to be of order T_0, in weakly stratified flows Rf scales as

$$Rf \sim \frac{w'^2 N^2 T_0^2}{w'^2} = Ri. \tag{3.3}$$

In moderately stratified flows (i.e. $0.1 < Ri < 10$), up to one and a half T_{BV} can develop implying buoyancy effects are relatively important in the active mixing period. Therefore, z' is assumed to be of order w'/N and ρ' scales as

$$\rho' = z' \frac{\partial \overline{\rho}}{\partial z} \sim \frac{w'}{N} \left| \frac{\partial \overline{\rho}}{\partial z} \right|, \tag{3.4}$$

and b scales as

$$b \sim \left(\frac{w'^2}{N} \right) \left| \frac{\partial \overline{\rho}}{\partial z} \right| \frac{g}{\rho_o} = w'^2 N. \tag{3.5}$$

In moderately stratified flows Rf scales as

$$Rf \sim \frac{w'^2 N T_0}{w'^2} = Ri^{1/2}, \tag{3.6}$$

because dt is still assumed to be of order T_0 as only $1.5 T_{BV}$ can develop during the active mixing period.

In the strong stratification regime N^{-1} becomes an important time scale and many T_{BV} can develop within the active mixing period. Buoyancy effects are important and ρ' and b scale as per moderate stratification, but dt is approximately equal to N^{-1} because the majority of density is fluxed within one T_{BV} (see Fig. 3.9). Therefore, Rf for strongly stratified flows scales as

$$Rf \sim \frac{w'^2 N}{w'^2 N} = \text{constant}. \tag{3.7}$$

The scaling regimes are plotted in Fig. (3.11) with DNS results for $Pr = 0.5$. The scaling in the moderately stratified regime, $Rf \sim Ri^{1/2}$, does not capture the behavior

entirely because the regime is a transitional zone between only inertial and both inertial and buoyancy effects being important.

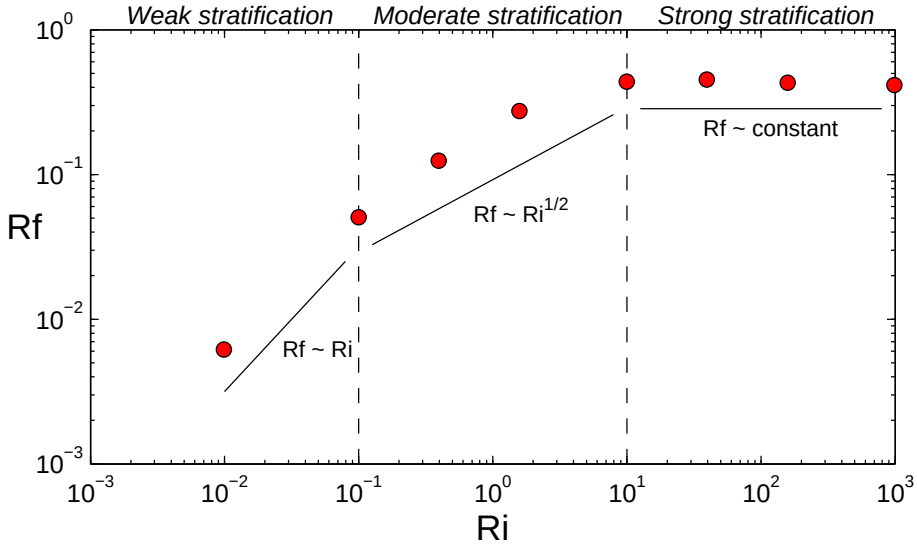

Figure 3.11: Rehmann & Koseff scaling regimes - The weak, moderate, and strong stratification scaling arguments fit DNS results for $Pr = 0.5$, creating three distinct regimes for stratification.

3.4.2 Buoyancy Reynolds number

The buoyancy Reynolds number R_b, defined in Sec. (3.4.2), is a commonly used parameter in oceanography to quantify turbulent intensity. From DNS data, Shih *et al.* (2005) parametrized turbulent diffusivity using R_b and observed three regimes.[1]Barry *et al.* (2001) performed a similar parametrization using laboratory data, and both concluded the flow behaves differently in three R_b regimes; the diffusive, the intermediate, and the energetic regimes. In the diffusive regime, $R_b < 7$, the flow is controlled by molecular effects and although stirred, it is essentially laminar. In the intermediate regime, $7 < R_b < 100$, the turbulent diffusivity increases with R_b. Peak Rf occurs in this regime because the turbulence is stationary (i.e. not developing further). The energetic regime, $R_b > 100$, is characterized by actively growing turbulence. Hence, Rf decreases from the critical value. It is unknown if the critical Rf is universal or dependent on the Reynolds number or flow type (Itsweire

et al., 1993).

The evolution of R_b are plotted in Fig. (3.12) for a range of Ri. Fig. (3.12) is similar to a plot shown by Stretch *et al.* (2010) with $N = 128$ DNS results, but in this work R_b peaks sharper and is multiple orders higher for flows in the energetic regime and slightly higher for flows in diffusive regime.

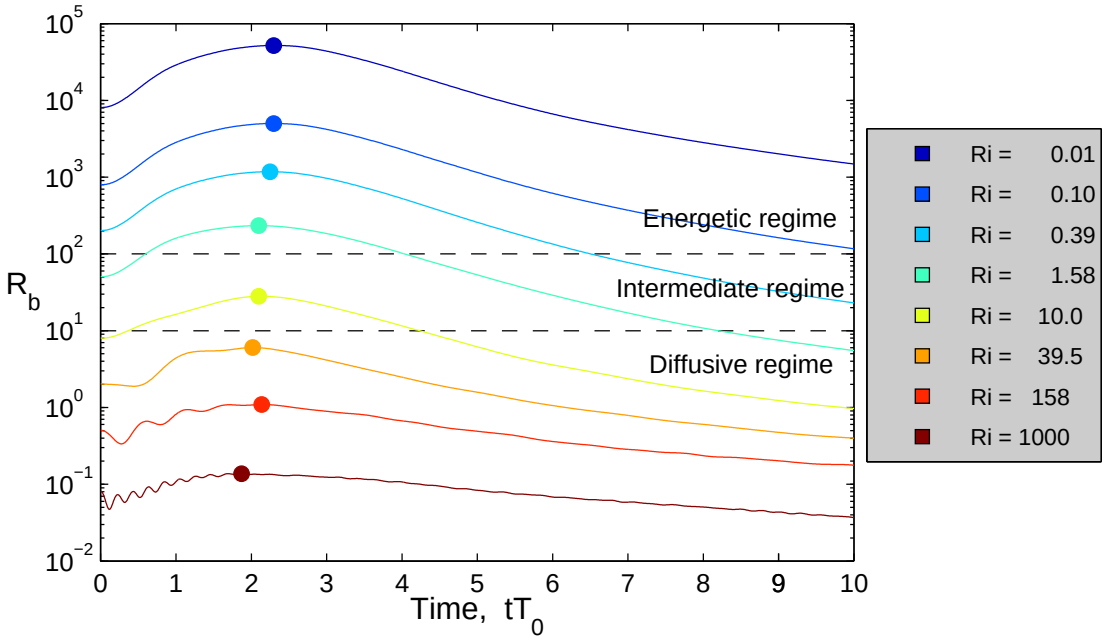

Figure 3.12: Evolution of buoyancy Reynolds number - The R_b regimes proposed by Shih *et al.* (2005) are plotted to provide a measure of the turbulent intensity. At strong stratification the simulations are diffusive.

[1]Stretch & Venayagamoorthy (2010) raised an important issue concerning the R_b regimes proposed by Shih *et al.*. Stretch & Venayagamoorthy argue that scaling of diapycnal diffusivity with ν at high Reynolds numbers is inconsistent with theory and experiments. An alternative parametrization of diapycnal diffusivity used by them did not reveal similar regimes, but rather a continuous spectrum. They also noted that effects of strongly anisotropic structures in the strongly stratified limit is inconclusive in their study. Although the R_b regimes may not contain important physical meaning, the regimes are still a quantitative measure of turbulent intensity used by other literature.

3.4.3 Regimes of buoyancy Reynolds number

The buoyancy Reynolds number can be calculated as a function of the turbulent Reynolds number Re_L and the turbulent Froude number Fr as follows.

$$R_b = \frac{\epsilon_k}{\nu N^2} = \left(\frac{k^2}{\epsilon_k \nu}\right)\left(\frac{\epsilon_k}{Nk}\right)^2 = Re_L Fr^2 \tag{3.8}$$

R_b is widely used because it requires no knowledge about shear or kinetic energy. Re_L at peak R_b ranges from 599 to 2349 while Fr spans many orders of magnitude and is of second-order in Eq. (3.8). Thus, in this work R_b are primarily a function of Fr.

Peak R_b are plotted in Fig. (3.13) as a function of corresponding Fr. The R_b regimes defined by Shih *et al.* (2005) and the Ri regimes defined by Rehmann & Koseff (2004) are additionally plotted, forming four distinct quadrants with intermediate zones. The Ri regimes are plotted by interpolating Ri between the minimum and maximum Fr, as there is no exact relation between Fr and Ri.

In quadrant I, the flow is energetic and strongly stratified. Oceanic and atmospheric flows are located in quadrant I. There are no results in quadrant I because the simulations are computationally restricted to moderate Re_L. The flow in quadrants II and III are either diffusive or weakly stratified, and quadrant IV contains both diffusive and weakly stratified flow. The ultimate goal of this work is to understand the mechanics of strongly stratified turbulence in quadrant I. The most energetic simulation in the strongly stratified regime is for $Ri = 10$.

Stratified turbulence may be described as either 'active' or 'fossil' turbulence (Gibson, 1980). In active turbulence the buoyancy forces are small compared to inertial forces so that overturning and mixing occur readily. Once the turbulence event is allowed to decay, remnant velocity and density fluctuations are fossil turbulence (Itsweire *et al.*, 1993). Turbulence in quadrant III can be classified as fossil turbulence from initial conditions because there is little active stirring.

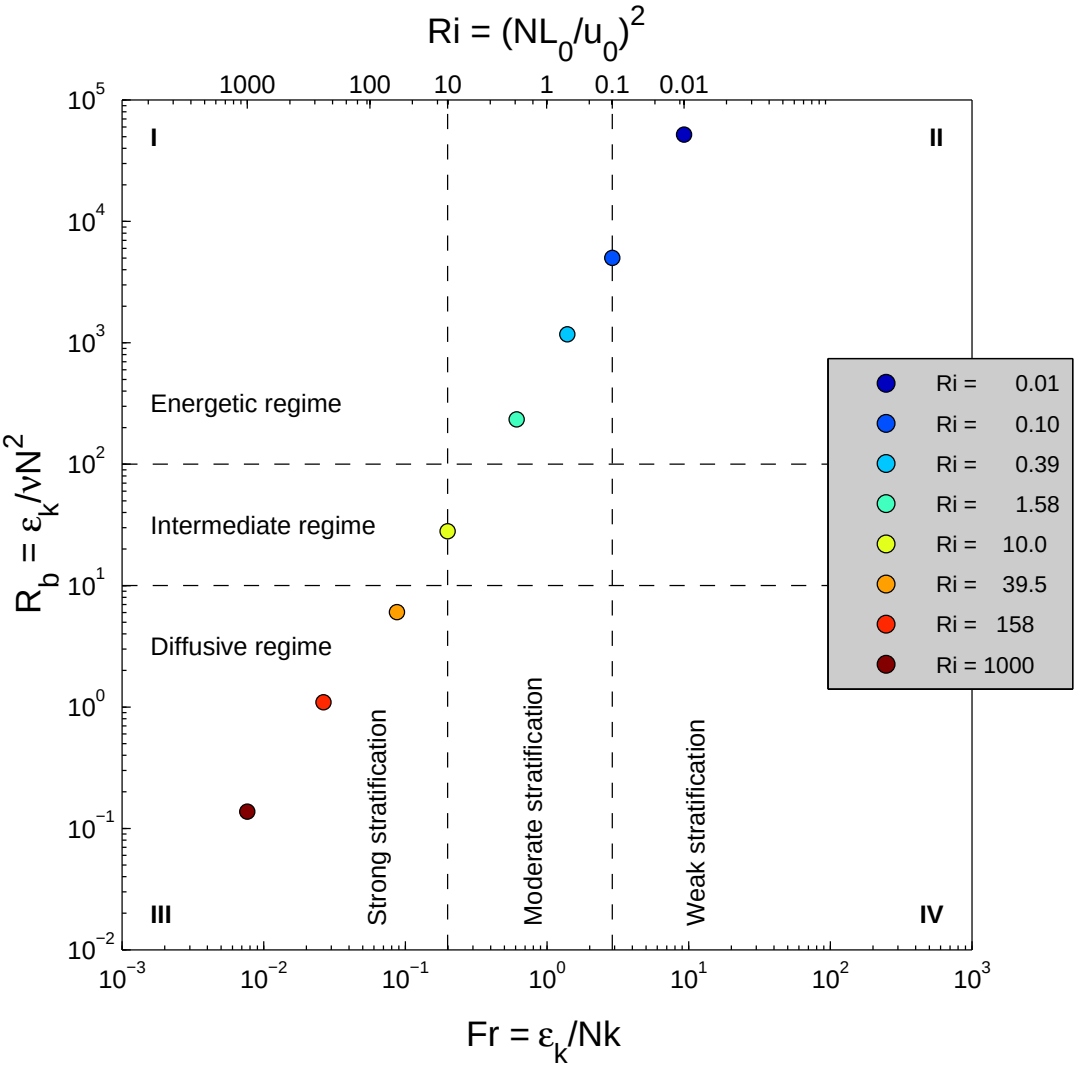

Figure 3.13: Regimes of buoyancy Reynolds number - Peak R_b are plotted as a function of Fr using Eq. (3.8). The R_b regimes, defined by Shih *et al.* (2005), and Ri regimes, defined by Rehmann & Koseff (2004), form four distinct quadrants. The ultimate goal of this work is to understand the mechanics of strongly stratified turbulence in quadrant I.

3.5 Coherent turbulent structures

In Kolmogorov's energy cascade, turbulence is injected as large eddies, which must evolve and breakdown to ever smaller scale motions until all energy is dissipated due to viscosity. The energy cascade, shown in Fig. (3.1), classically illustrates the range of scales characteristic to three-dimensional turbulence. It is the energy containing range and viscosity which control the range of scales, where larger energy-containing eddies and/or lower viscosity expand the energy cascade. Coherent turbulent structures in the energy containing range are important to qualitatively and quantitatively describe the large-scale control of the energy cascade.

Eddies are vortical, rotating phenomena and are most conveniently described with vorticity, the curl of the velocity gradient,

$$\omega = \nabla \times \mathbf{u}. \tag{3.9}$$

Enstrophy $\mid \omega^2 \mid$, the square of vorticity, is plotted for weak stratification in Fig. (3.14). Isotropic turbulence is characterized by vortical tube-like structures which move about the domain interacting with one-another. The weakly stratified enstrophy structures resemble isotropic turbulence because buoyancy effects are weak relative to inertial effects. At strong stratification, vertical motions are restricted by buoyancy resulting in anisotropic but axisymmetric turbulence. The enstrophy structures, shown in Fig. (3.15), resemble 'pancake' shapes. These 'pancake' structures have been observed by many studies (e.g. Metais & Herring, 1989; Holt *et al.*, 1992; Kimura & Herring, 1995; Venayagamoorthy & Stretch, 2006). The turbulence simulated and generated in these studies is generally restricted to low and moderate Reynolds numbers, and it is unknown how findings compare with high Reynolds number ocean or atmospheric flows (Riley & deBruynKops deBruynKops, 2003).

The evolution of enstrophy structures for weak, moderate, and strong stratification are shown in Fig. (3.16), where the isosurface is 2.5 times the root-mean-square enstrophy in each subplot. Horizontal layering form at later times for moderate stratification but none

for weak stratification. The 'pancake' structures form very quickly for strong stratification and become very pronounced at later times times. The remaining energy at later times of strongly stratified turbulence is higher than that of weakly stratified turbulence because the dissipation rate of turbulent kinetic energy is less for strong stratification. Thus, the corresponding isosurface values between Figs. (3.16i-l) at later times are not directly comparable. Animations show 'pancake' structures for strong stratification at $4T_0$ moving rapidly within their respective layers while the turbulent structures for weak stratification are mostly dead. Cross-sections of enstrophy through the center of the domain are plotted in Fig. (3.17), which further illustrates the strongly anisotropic structures for $Ri = 1000$ but mostly isotropic structures for $Ri = 0.1$ and 10. After two eddy turnovers, the center of enstrophy structures for weaker stratification contain higher vorticity than for stronger stratification.

As shown in Fig. (3.5), turbulent kinetic energy of strongly stratified turbulence is mostly in the horizontal direction, which explains why 'pancake' structures move within their respective layers with little interaction between layers. The evolution of the horizontal and vertical vorticity are plotted in Figs. (3.18) and (3.19), respectively. For weak stratification, the vertical vorticity structures are tall vortex tubes while for strong stratification, the vertical vorticity structures are restricted to horizontal layering. The 'pancake' shaped structures are dominated by strong horizontal vorticity as the magnitude of vertical vorticity is much lower. Lagrangian visualizations of strongly stratified turbulence by Venayagamoorthy & Stretch (2006) illuminate how particles undulate within enstrophy structures but have little interaction between vertical layers. Thus, the rapid fluctuation of particles due to buoyancy effects at high Ri is responsible for the increased horizontal vorticity. Praud *et al.* (2005) observed the vertical vorticity in strongly stratified turbulence to be a patchwork of positive and negative regions such that enstrophy structures are contributing vorticity to one another rather than counteracting vorticity.

Majda & Grote (1997) used analytical methods to calculate the evolution of columnar dipole vortices in laminar flow. The results show that the columnar dipole vortices turn into vertically layered 'pancake' vortex sheets, similar to the observations in this work.

Although their solution is qualitative, it illustrates that 'pancake' structures can exist in non-turbulent (i.e. laminar) flows.

The strong horizontal layering at later times implies the flow is two-dimensional for strongly stratified diffusive flows. Two-dimensional turbulence is characterized by merging vorticies and an increase in their length scale, making it a very different phenomena than three-dimensional turbulence where eddies continuously decay as the flow evolves. Iida *et al.* (2009) observed a transfer of vortex energy into wave energy in a numerical study of strongly stratified turbulence. They attributed the vortex-wave triad to be responsible for the layered structures. Additionally, the inertial subrange with $-5/3$ scaling is longer for strong stratification than for weak stratification[1], and the existance of an inertial subrange is a fundamental characteristic of three-dimensional turbulence (Brethouwer & Lindborg, 2009). Although the flow is strongly anisotropic with supressed vertical motions, the simulations of strongly stratified turbulence are still three-dimensional.[2]

[1] See Fig. (3.2) for energy cascade plots.

[2] The near two-dimensional turbulence at high N is fundamentally different than quasi-geostrophic turbulence, where both stratification and rotation are significant and the layers are strongly coupled (Kimura & Herring, 2002).

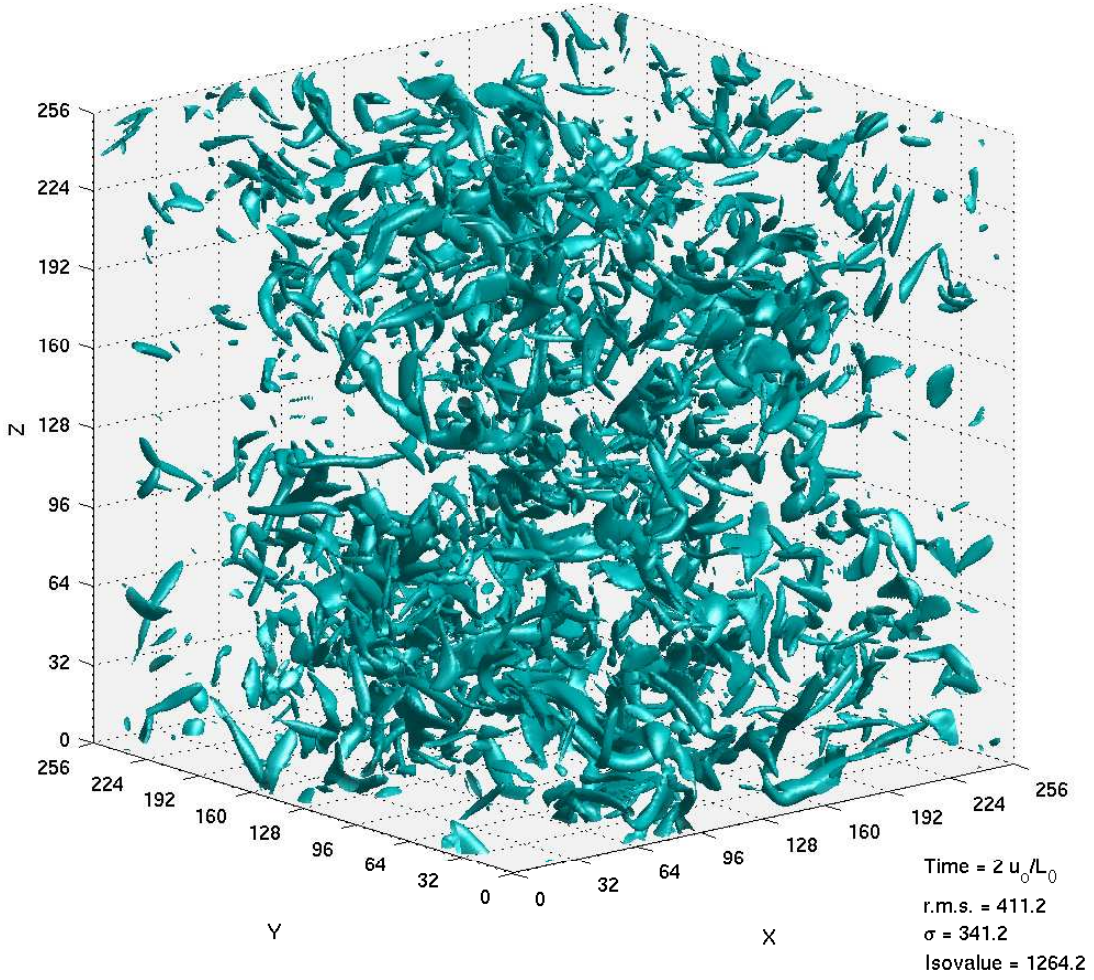

Figure 3.14: Isotropic enstrophy structures - The enstrophy structures of weak stratification ($Ri = 0.1$) after two eddy turnover times resemble vortex tubes associated with classic isotropic turbulence (e.g. Vincent & Meneguzzi, 1991). Isosurfaces are 2.5 times the root mean square enstrophy.

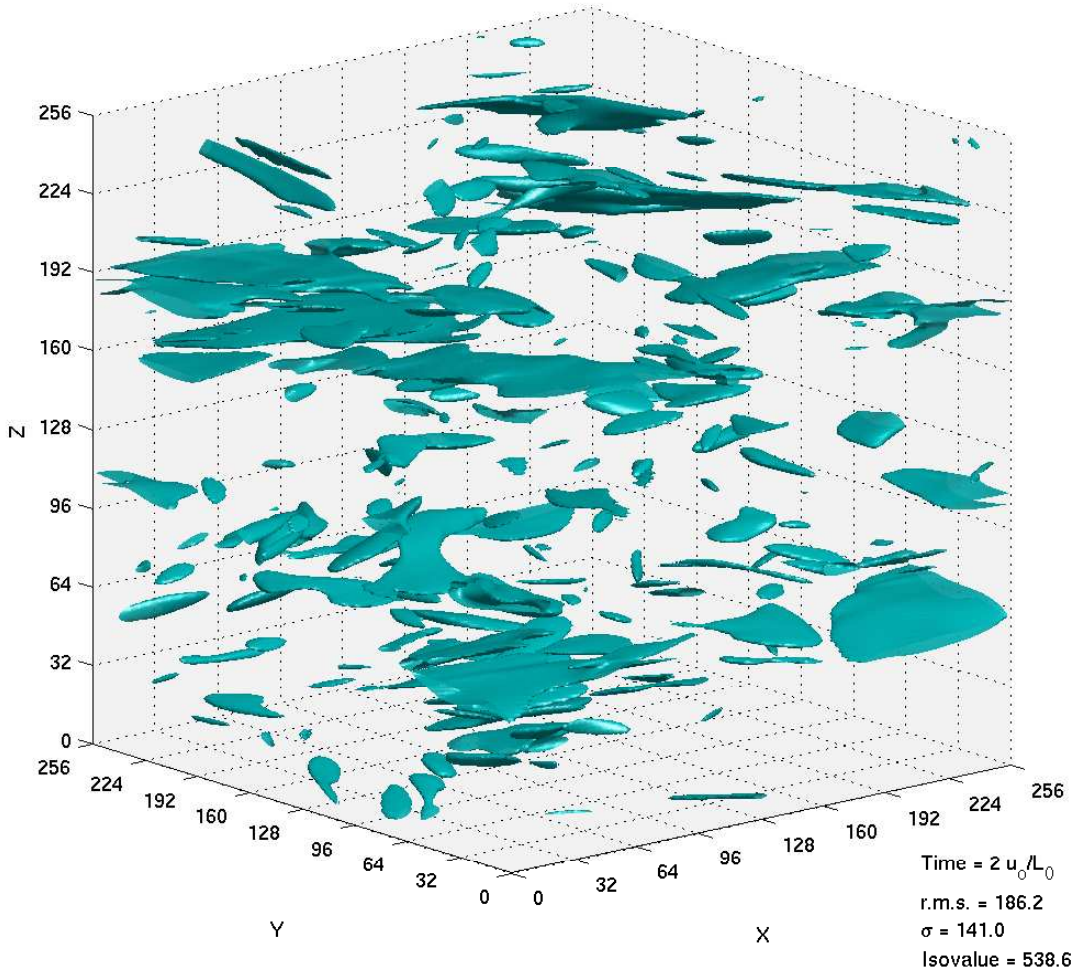

Figure 3.15: Pancake enstrophy structures - The enstrophy structures of strong stratification ($Ri = 1000$) after two eddy turnover times are strongly anisotropic. The structures are commonly described as having 'pancake'-like appearances. Isosurfaces are 2.5 times the root mean square enstrophy.

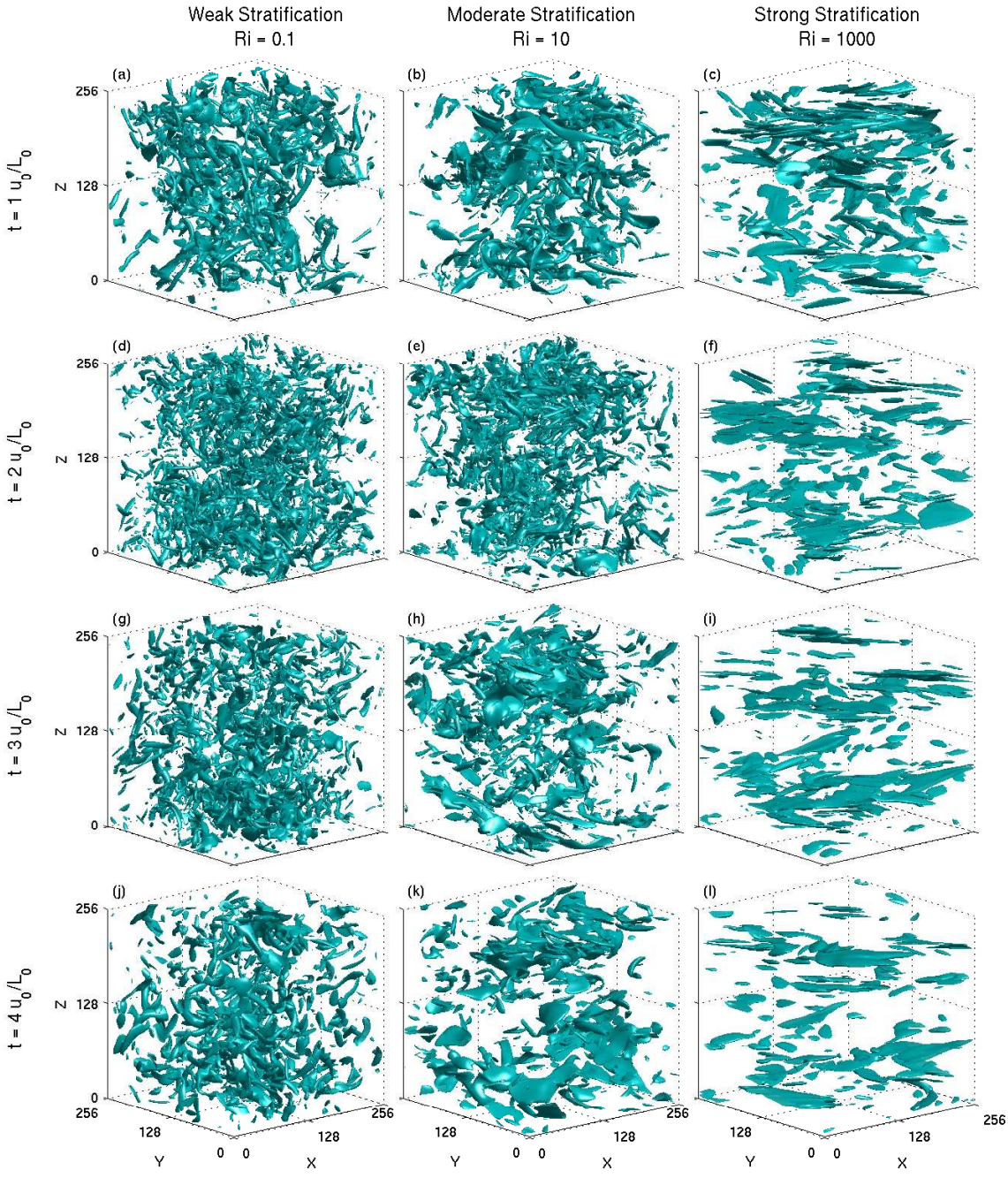

Figure 3.16: Evolution of enstrophy structures - Enstrophy isosurfaces for $Ri = 0.1, 10, 1000$ at eddy turnover times 1-4. Isosurface levels are 2.5 times root mean square.

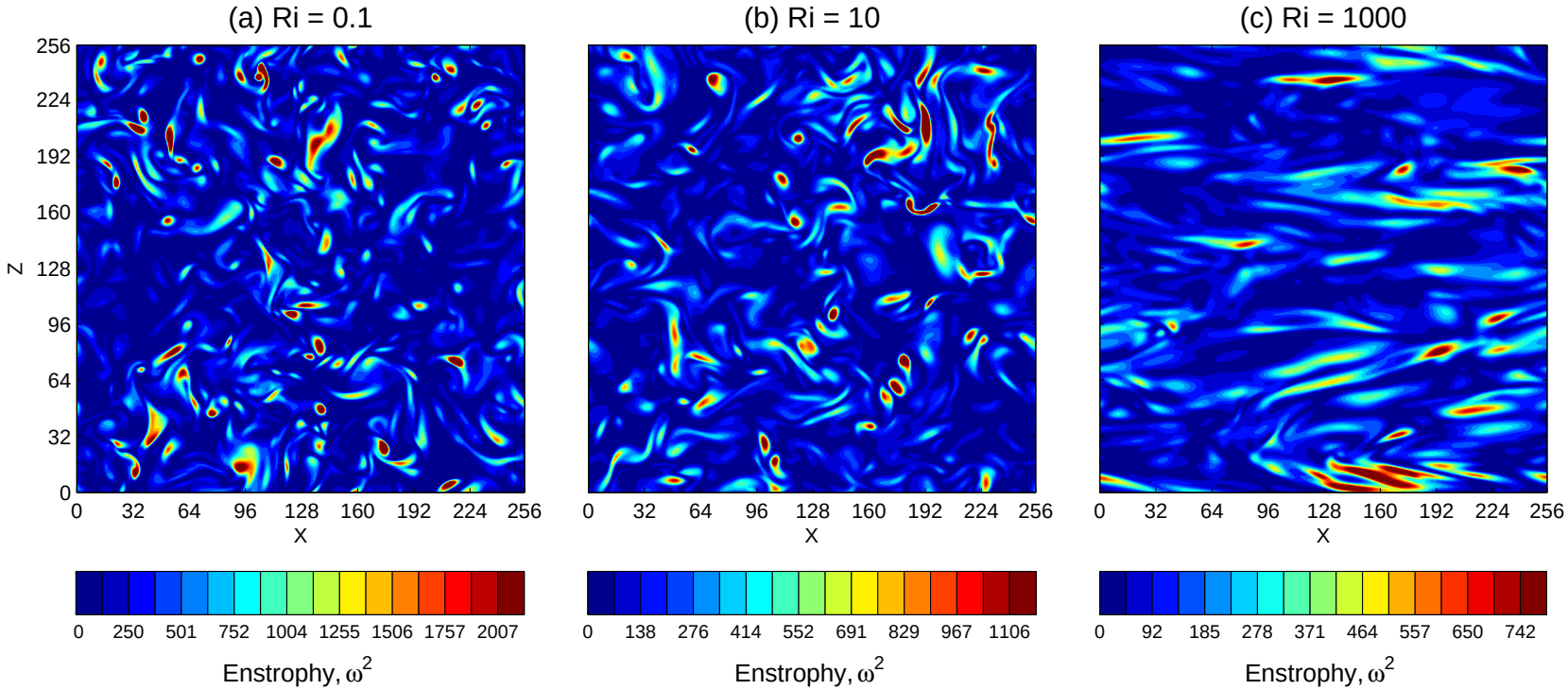

Figure 3.17: Cross-sections of enstrophy fields - Cross-sections of enstrophy through the center of the domain (i.e. $y = 128$) at $t = 2T_0$ reveals strongly anisotropic structures for $Ri = 1000$ but mostly isotropic structures for $Ri = 0.1$ and 10. The center of enstrophy structures in weaker stratification contain higher vorticity than in stronger stratification.

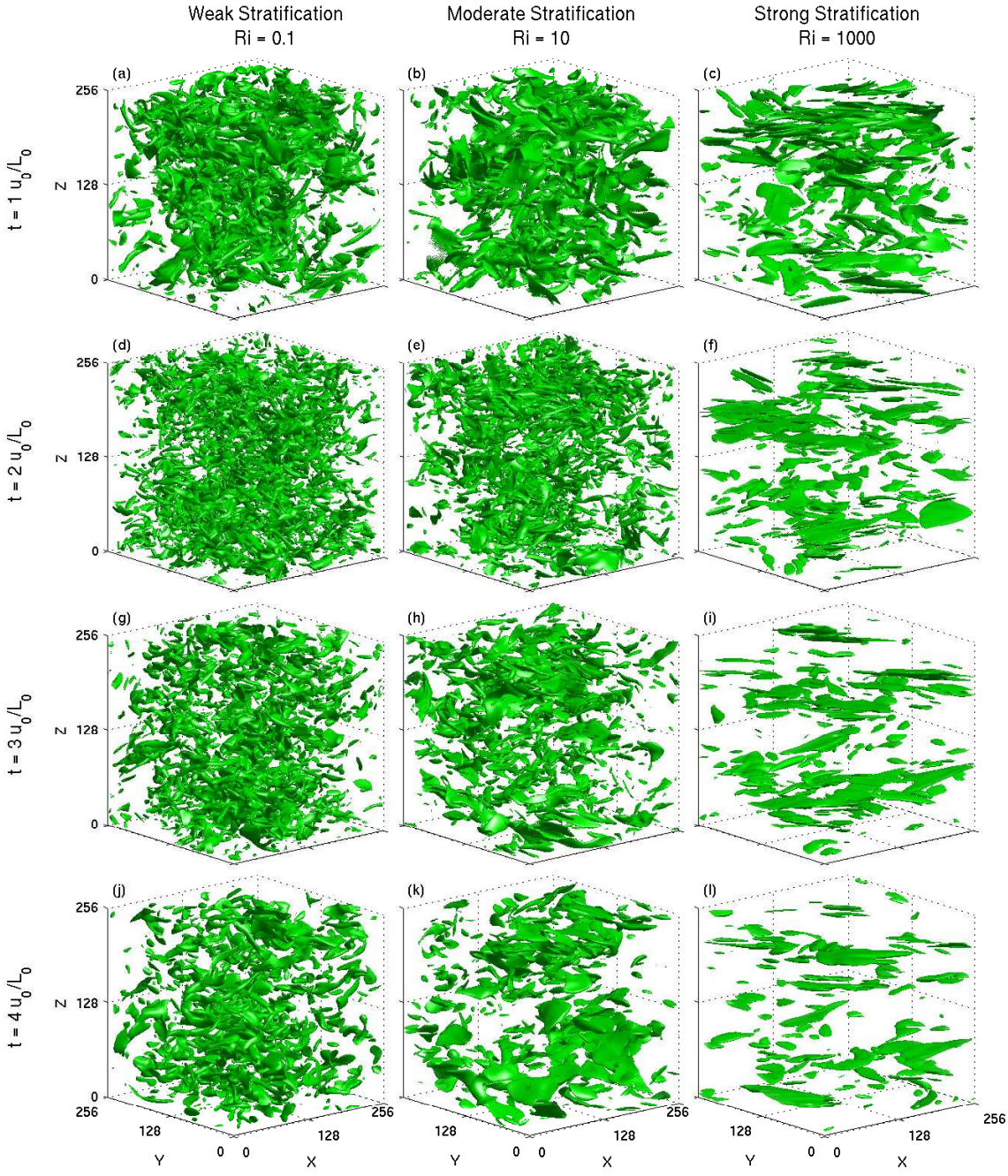

Figure 3.18: Evolution of horizontal vorticity structures - Horizontal vorticity isosurfaces for $Ri = 0.1, 10, 1000$ at eddy turnover times 1-4. Isosurface levels are 2 times root mean square.

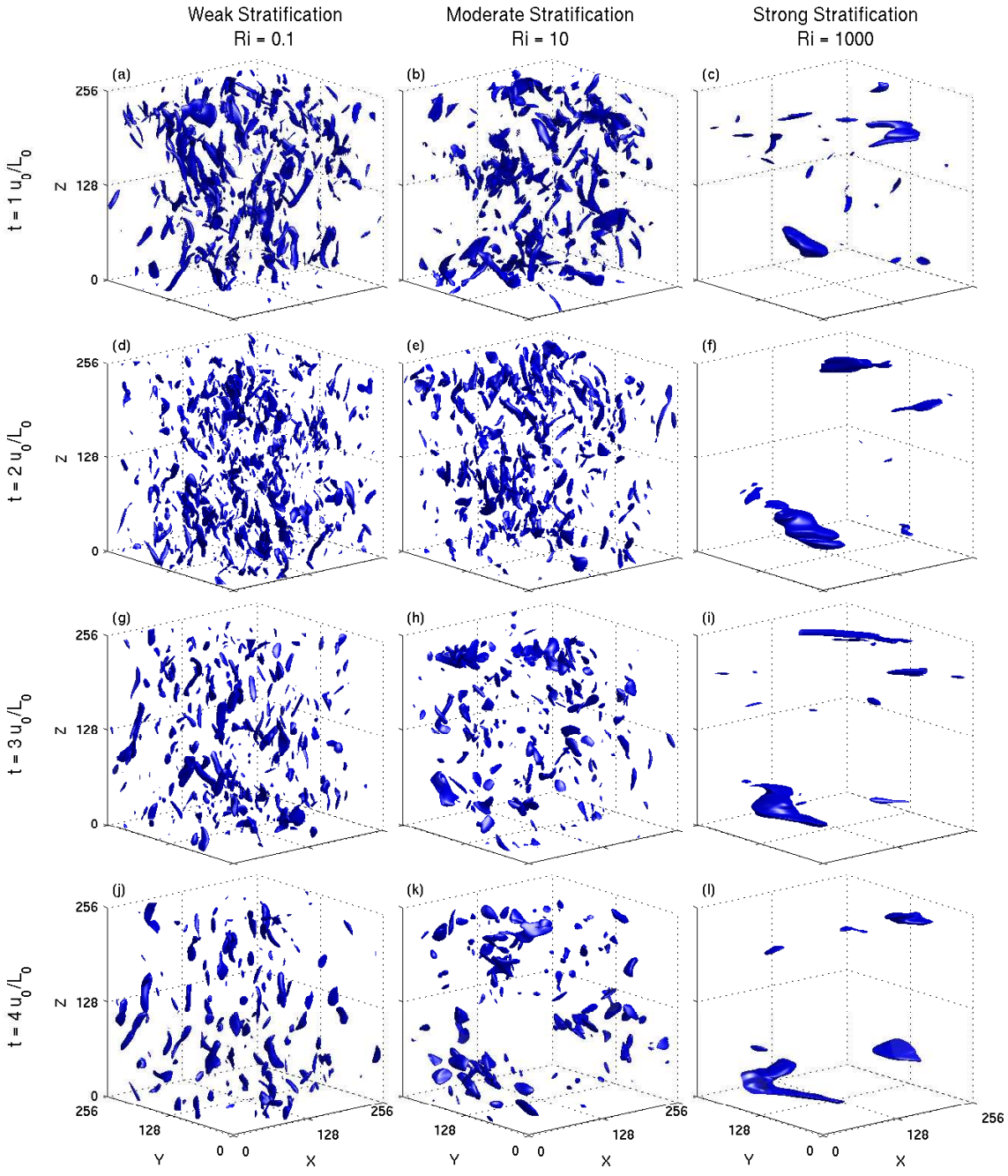

Figure 3.19: Evolution of vertical vorticity structures - Vertical vorticity for $Ri = 0.1, 10, 1000$ at eddy turnover times 1-4. Isosurface levels are 2.5 times root mean square.

3.6 Diffusivity

Scalar diffusivity is a product of both molecular and turbulent processes. The influence of molecular diffusion is accounted for in the density transport equation (Eq. 2.7) through the molecular diffusion coefficient κ. The influence of turbulent diffusion can be quantified with eddy diffusivity K_ρ,

$$K_\rho = -\frac{\overline{\rho' w'}}{\partial \overline{\rho}/\partial z}. \tag{3.10}$$

The concept of eddy diffusivity arises from the gradient-diffusion hypothesis, i.e. turbulent transport is assumed down the mean scalar gradient. The effective diffusivity κ_{eff} is the sum of both κ and K_ρ.

Eddy diffusivity is parametrized by the Osborn-Cox model as (Osborn, 1980)

$$K_\rho = \frac{Rf}{1 - Rf}\frac{\epsilon_k}{N^2}. \tag{3.11}$$

The definition of Rf requires convergence to zero with the gradient Richardson number Ri_g and Ri. Physical experiments and direct measurements of large scale flows agree that Rf approaches a constant at high Ri_g (Pardyjak *et al.*, 2002; Strang & Fernando, 2001). Parametrizations of Rf versus Ri_g by Mellor & Yamada (1982) and Nakanish (2001) capture this trend, but different flow types converge upon different values at high Ri_g. It is generally agreed among oceanographers that Rf for energetic ocean flows is approximately equal to 0.17 (i.e. $\Gamma = 0.2$) (Thorpe, 2005). Measurements in the upper atmosphere reveal Rf to be slightly higher than in ocean flows (Pardyjak *et al.*, 2002). An additional complexity from field measurements is that Rf may have high spatial and temporal variability (Oakey, 1982; Pardyjak *et al.*, 2002). Additionally, a constant mixing efficiency may only be appropriate for an isolated patch in the interior and be meaningless to relate fluxes between the patch and the outside ambient fluids because flows are rarely in a quasi-steady-state condition (Ivey *et al.*, 2008). Parametrization of Rf is an important problem in fluid flow modeling. This section explores the value of Rf from DNS and results are compared with grid-tow experiments. Prandtl number effects of mixing efficiency are investigated in Sec. (3.6.1) and

are compared with laboratory experiments in Sec. (3.6.2).

The value of Rf is explored further using RDT in Secs. (3.7.2)-(3.7.3).

3.6.1 Prandtl number effects

The relative influence of viscosity ν to the molecular diffusivity κ is given by the Prandtl number $Pr = \nu/\kappa$. If $Pr \gg 1$, viscosity (i.e. momentum diffusivity) is dominant and if $Pr \ll 1$, molecular diffusivity is dominant.

The flux Richardson number Rf was calculated for all runs performed in the main parametric study, where Ri was varied from 0.1 to 1000 and Pr was varied from 0.1 to 2. The results for all runs are plotted in Fig. (3.20).

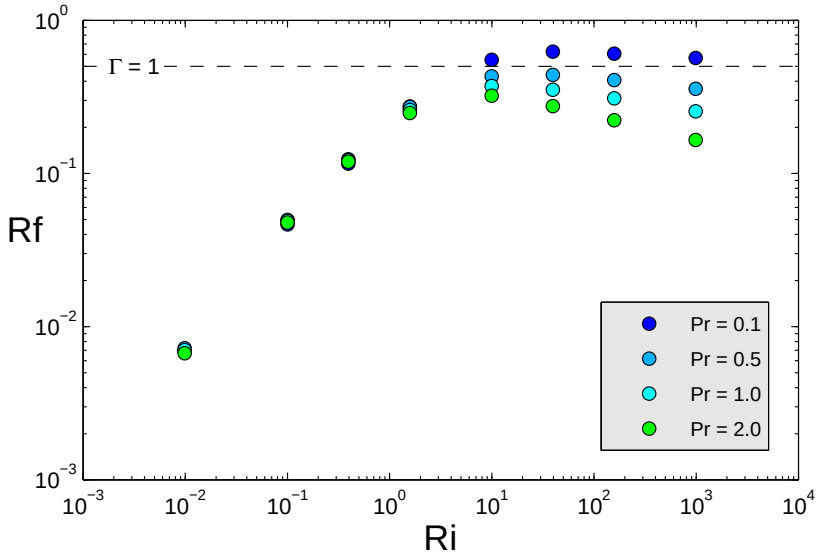

Figure 3.20: Prandtl number effects - Flux Richardson number versus gradient Richardson number with varying Prandtl numbers. For strong stratification Rf separates for varying Pr.

In Fig. (3.20), for $Ri \lesssim 10$ all results collapse with no apparent dependence of Rf on Pr. The results scale as per scaling arguments for weak and moderate stratification regimes discussed in Sec. (3.4.1). When $Ri \gtrsim 10$ the results begin to separate suggesting Rf is dependent on Pr for these low Reynolds number flows with strong stratification. For $Pr = 0.1$, Rf is approximately constant across Ri but when $Pr \geq 0.5$, Rf gradually decreases as Ri increases.

To further investigate the irreversible effects, the mixing efficiency Γ (i.e. the ratio of irreversible conversion of kinetic energy into potential energy) can be related to Rf as

$$\Gamma = \frac{Rf}{1 - Rf}. \tag{2.33}$$

If the kinetic energy and potential energy dissipations are equal, then $\Gamma = 1$ and $Rf = \frac{1}{2}$. If $\Gamma > 1$ then potential energy is dissipated faster than kinetic energy and $\frac{1}{2} < Rf < 1$. The kinetic and potential energy dissipation rates contain the coefficients ν and κ, respectively, in addition to terms $\overline{(\partial u_i/\partial x_j)^2}$ and $\overline{(\partial \rho'/\partial x_j)^2}$, respectively. For highly turbulent flows the tensor terms are of leading order and ν and κ do not control the flow. However, for diffusive flows, Fig. (3.20) suggests ν and κ become dominant. It follows that as Pr decreases Γ must increase. At $Ri = 1000$, Pr decreases from 2 to 0.1 and Γ increases from 0.2 to 1.3. Rf must be less than unity for decaying or stationary turbulence and as $Pr \to 0$, Rf should converge to 1.

When κ and ν are equally partitioned, the simulations indicate $\epsilon_k > \epsilon_p$ (i.e. $\Gamma < 1$). The Pr threshold where potential energy is dissipated more efficiently than kinetic energy (i.e. $\Gamma > 1$) is between $Pr = 0.1$ and 0.5. For $Pr = 0.1$, the highest Γ is 0.59 at $Ri = 10$.

To further investigate irreversible effects, the evolutions of the irreversible form of instantaneous mixing efficiency (Eq. 2.26) for $Ri = 1000$ and all Pr are plotted in Fig. (3.21). It can be seen that the instantaneous mixing efficiency for $Pr = 0.1$ is substantially higher than unity during the first two eddy turnover times, but for $Pr = 1$ the instantaneous mixing efficiency is always below unity. Thus, it follows that for the diffusive DNS simulations $\epsilon_k < \epsilon_p$ when $Pr \ll 1$.

The Pr effects observed in DNS are expected to diminish for energetic and strongly stratified flows and converge upon a single value. Rf is plotted versus R_b in Fig. (3.22) to investigate the activity level of the flows. The energetic simulations correspond with weak stratification and diffusive simulations with strong stratification. Prandtl number effects are only present for $R_b \lesssim 100$, which corresponds with diffusive and intermediate flows. From DNS (with $N = 32$), Ivey *et al.* (1992) observed similar Pr effects at low R_b. These

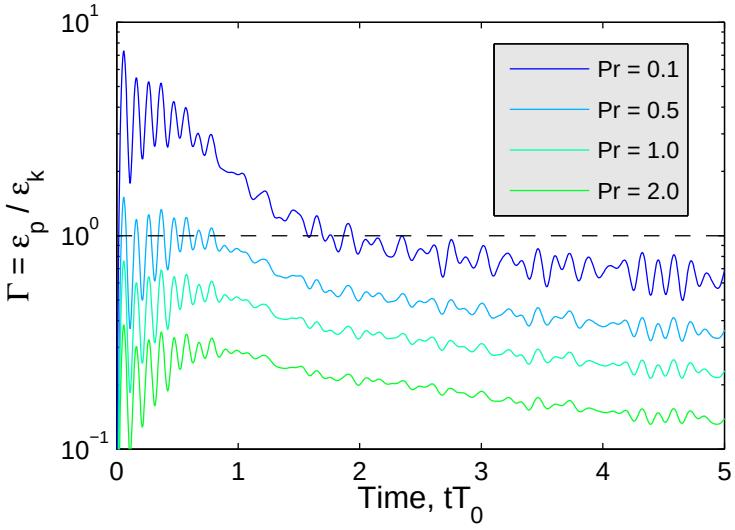

Figure 3.21: Evolution of instantaneous mixing efficiency - The Prandtl number ranges from 0.1 to 2 and $Ri = 1000$. If $Pr \ll 1$ then $\epsilon_k < \epsilon_p$ for the first two eddy turnovers.

results imply that the observed Pr effects are only a product of the flow being diffusive.

Overturns are a fundamental mechanism of advective mixing, and lack there-of implies a more diffusive flow. Diffusive flows correspond with weak or rare overturns. Gibson (1980) found small dissipation rates and rare overturning for $R_b < 30$. Stillinger *et al.* (1983) and Itsweire *et al.* (1986) similarly found minimal overturning when $R_b < (15 - 21)$ in physical experiments. The weak overturning in strongly stratified flows is the product of strong buoyancy effects exemplified by the majority of kinetic energy being channeled into the horizontal directions. The effective diffusivity normalized by the molecular diffusivity in Fig. (3.23) illustrates the decreased vertical mixing in for diffusive flows.

For $Ri \lesssim 10$ the flows are energetic and the turbulence is generally isotropic resulting in strong overturning, strong vertical advective mixing relative to molecular mixing, and negligible Prandtl number effects. For $Ri \gtrsim 10$, the turbulence is diffusive with strong anisotropy resulting in minimal vertical advective mixing and strong Prandtl number effects. Thus, mixing efficiency is a property of the fluid for diffusive flows but becomes a property of the flow for energetic flows.

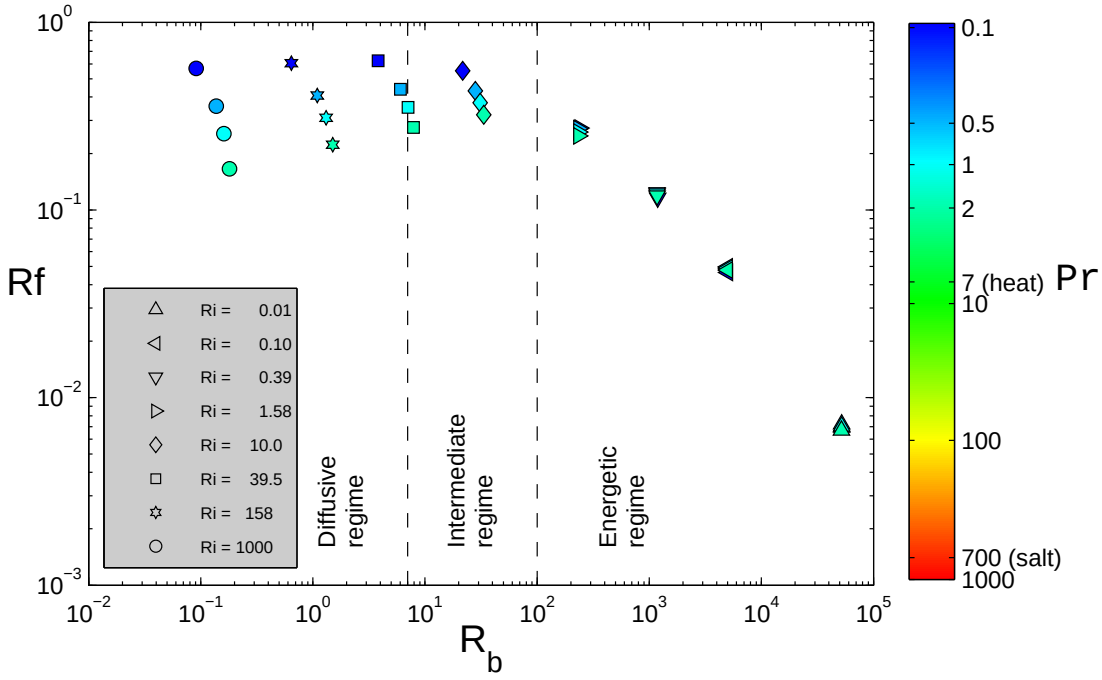

Figure 3.22: Flux Richardson number versus buoyancy Reynolds number - The energetic simulations correspond with weak stratification and diffusive simulations with strong stratification. Pr effects are only present for diffusive and intermediate flows.

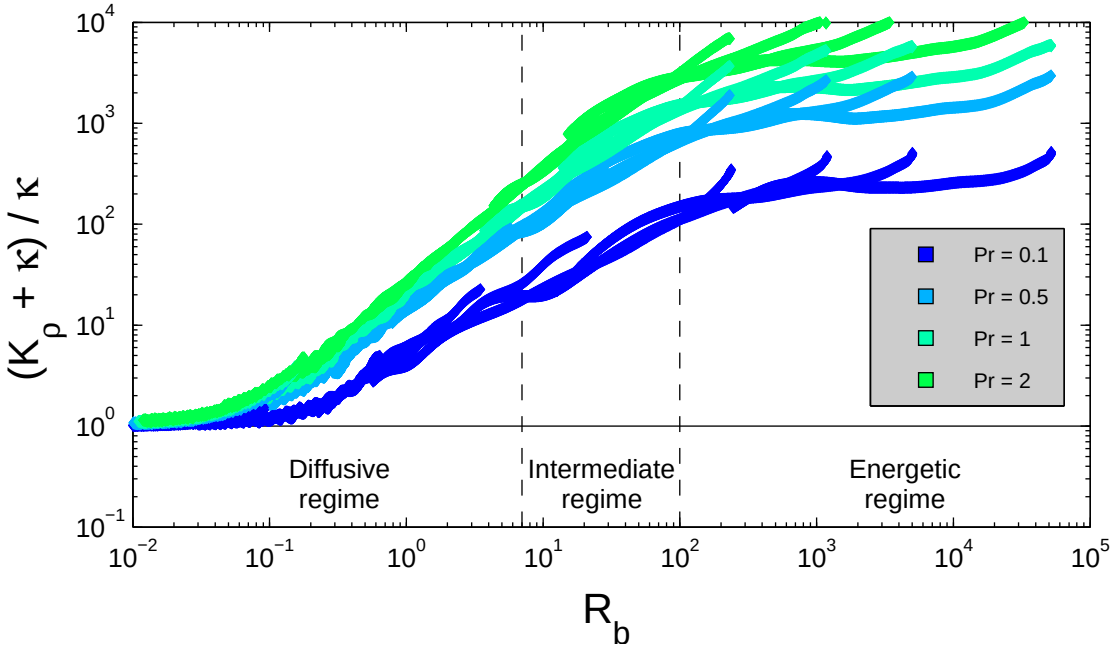

Figure 3.23: Total eddy diffusivity normalized with molecular diffusivity - For diffusive flows the dominant scalar diffusivity is the molecular diffusivity κ while for energetic flows the eddy diffusivity K_ρ is many orders larger than κ.

3.6.2 Comparison with physical experiments

In grid-tow experiments, an initial Richardson number Ri can be defined from initial conditions allowing direct comparison between DNS and physical experiments. The DNS results are plotted in Fig. (3.24) with results from grid-tow experiments performed by Britter (1985), Rottman & Britter (1986), and Rehmann & Koseff (2004). The physical experiments were performed using either heat in water ($Pr = 7$) or salt in water ($Pr = 700$). There is a large discrepancy between the grid-tow dataset and DNS results. Stretch *et al.* (2010) plotted the same grid-tow dataset with $N = 128$ DNS results and noted a similar discrepancy. No DNS were performed for high Pr because Reynolds number sacrifices are too great as the lower spatial resolution limit L_B increases as $Pr^{1/2}$. Grid-tow experiments are limited to $Pr = 7$ and 700 and there are no results available for $Ri > 10$. Thus, it is unclear from Fig. (3.24) how the numerical and physical experiments compare.

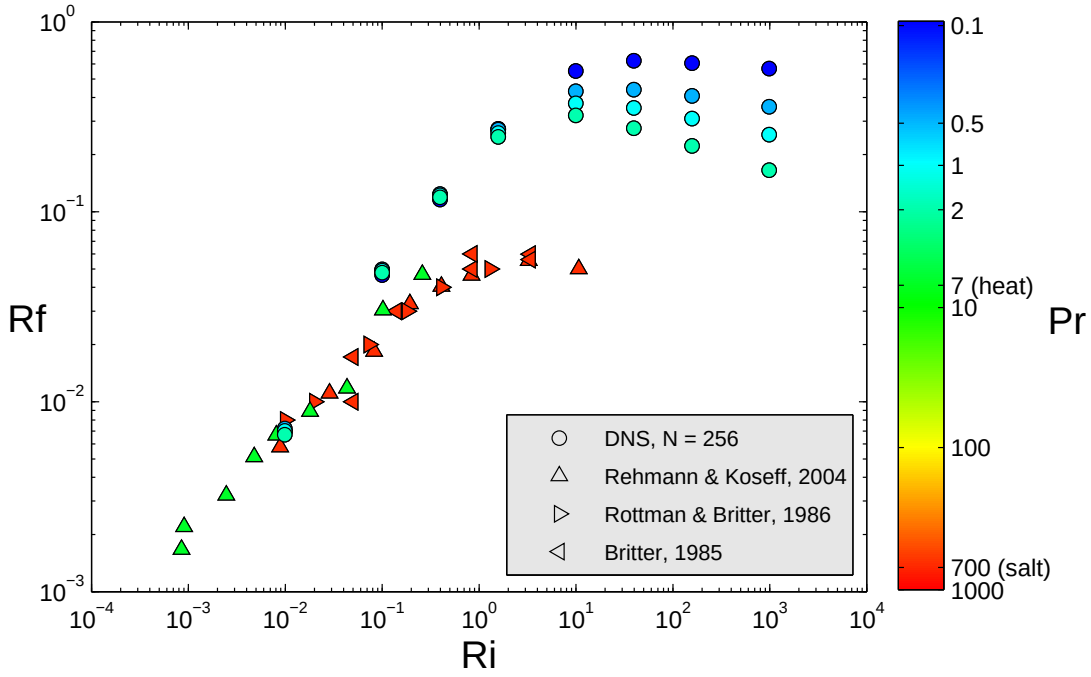

Figure 3.24: Comparison of flux Richardson numbers from grid-tow and DNS - The flux Richardson number Rf is plotted versus Ri for DNS and grid-tow experiments. The color of the marker represent the Prandtl number and the shape represents the experiment source. It was not possible to perform DNS for high Pr. Similarly, Rf from physical experiment are available only for $Pr = 7$ (heat in water) and 700 (salt in water) and there are no results for $Ri > 10$.

Stretch *et al.* (2010) attributed the discrepancy to two potential sources of error. The first is non-matching initial conditions resulting in Ri not being directly comparable between DNS and RDT. The second is that not all energy in grid-tow experiments was transfered into turbulent kinetic energy because surface waves were observed in the tanks, among other losses. It was assumed in physical experiment studies that all energy input E_{input} was transfered directly into k. Stretch *et al.* argue that if only 45% of E_{input} was transfered into k it would result in a fivefold increase of Rf. This would raise Rf from physical experiments closer to numerical experiments.

For DNS with $Ri < 1$, all Rf collapse without apparent Pr effects. In this range numerical and physical experiments are within reconcilable error as the steeper scaling in Fig. (3.24) may be evidence of non-matching initial conditions. As Ri increases the difference between physical and experiments grows larger in addition to DNS Pr effects developing. To investigate this trend, Rf is plotted versus Pr in Fig. (3.25) for DNS with $Ri = 10$ and a grid-tow experiment with $Ri = 10.7$ (the highest Ri achieved by Rehmann & Koseff). The trend suggests Rf continuously decreases as $Pr^{-0.32}$. In Fig. (3.24) it can be seen that this trend steepens as Ri increases. If the difference between physical and numerical experiments is due to Pr effects then Rf must decrease when $Ri > 10$ for $Pr = 700$. Although this trend was not observed in grid-tow experiments, it was argued by dimensional reasoning to occur by Rehmann (2004). Scaling at the diffusive limit is explored further in Sec. (3.7.3) using RDT.

3.7 Rapid-Distortion Theory

RDT is a linearization of the governing equations where the non-linear advection and diffusion terms are neglected. In Sec. (3.7.1) RDT is used as a tool to further investigate the decoupling between vertical and horizontal dynamics for strong stratification. RDT is not bound by similar computational restrictions as DNS because RDT is a linearize form of the governing equations, and can therefore be used to investigate trends outside DNS constraints. In Sec. (3.7.2) RDT and DNS parameteric studies were performed to further

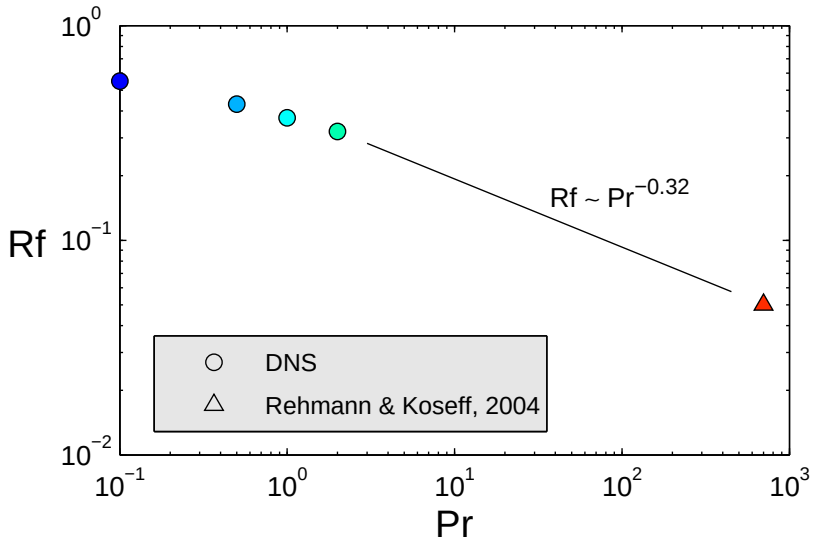

Figure 3.25: Flux Richardson number versus Prandtl number for DNS and grid-tow. - The difference between numerical and physical experiments may be due to Prandtl number effects. The physical experiment is for $Ri = 10.7$ from Rehmann & Koseff (2004) and DNS are for $Ri = 10$. For $Ri = 10$ it appears $Rf \sim Pr^{-0.32}$ for $Ri = 10$, which assumable steepens as Ri increases.

explore Reynolds number effects. In Sec. (3.6.1) a RDT parametric study was performed to further exploring Prandtl number effects.

3.7.1 Decoupling of horizontal and vertical dynamics

DNS and RDT models for $Ri = 1000$ predict very similar time evolutions of the ensemble-average buoyancy flux b. RDT can be used to model b for strongly stratified flows because the controlling time scale N is a linear process. Fig. (3.26) confirms b from DNS and RDT are closely related, which allows the vertical dynamics to be modeled using RDT.

In weakly stratified flows the buoyancy period T_{BV} is much longer than the duration of the event while DNS revealed b to peak at approximately T_0. RDT models were performed for weak stratification and it was found b peaks at approximately T_{BV}, which is inconsistent with DNS. Thus, RDT can only be used for strong stratification where buoyancy effects are strong and T_{BV} is much shorter than T_0. This is consistent with theoretical basis of RDT discussed in Sec. (2.6.3).

Contrary to vertical dynamics, the turbulent structures modeled by RDT are very dif-

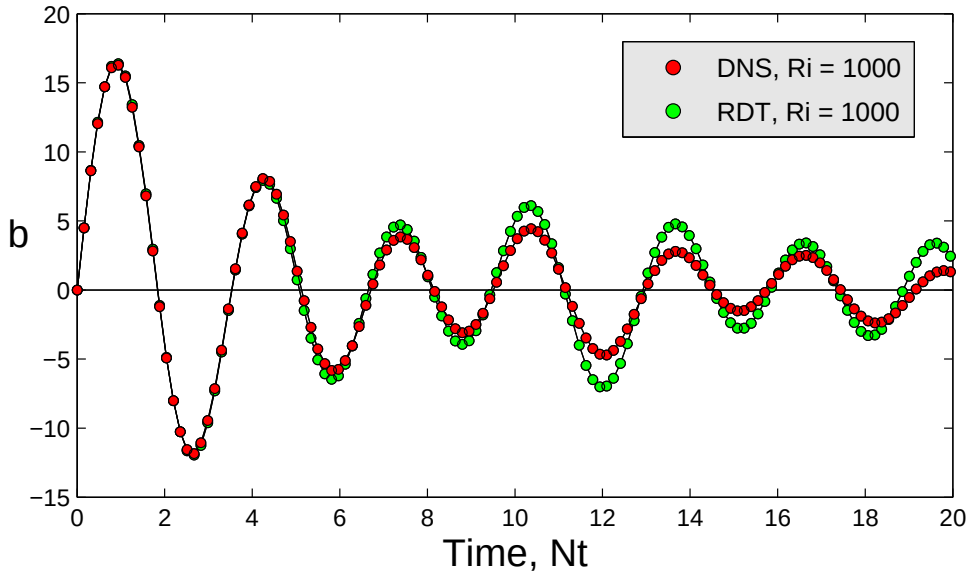

Figure 3.26: Comparison of DNS and RDT buoyancy flux - The volume-average non-dimensional buoyancy flux b of DNS and RDT for $Ri = 1000$ are plotted as a function of time non-dimensionalized with N. RDT and DNS predict similar vertical dynamics for strong stratification allowing vertical dynamics to be modeled with RDT.

ferent than DNS. In Fig. (3.27) the turbulent structures of RDT lack the chaotic nature and range of scales characteristic to turbulence. The RDT model does not predict anisotropic structures as does the strongly stratified DNS. Weak and strong stratification RDT models predict structures of very similar geometry but are differentiated by the rate at which enstrophy structures move about the domain. The buoyancy flux is a phenomena of vertical motions and is independent of non-linear effects while the turbulent structures are a product of the non-linearity. Thus, RDT illustrates the decoupling which occurs between vertical and horizontal dynamics at strong stratification.

3.7.2 Reynolds number effects

To test the conjecture that the Prandtl number effects are an effect of the low Reynolds numbers, a comparative Reynolds number DNS and RDT studies was performed. Re_0 was varied between 100 and 625 for $Pr = 0.1$, 0.5, and 1 for the DNS study. All twelve DNS runs are for $Ri = 1000$ and are summarized in Table (A.2). Five models were run for Re_0 ranging from 100 to 1000 for the RDT study. The Reynolds number DNS and RDT studies

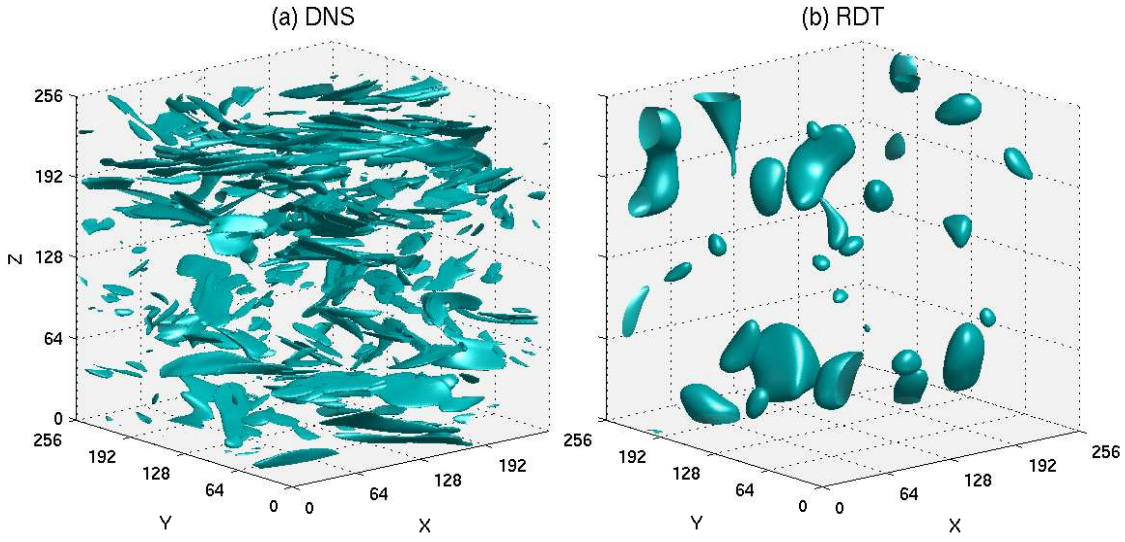

Figure 3.27: Comparison of DNS and RDT enstrophy structures - The enstrophy structures of DNS and RDT with $Ri = 1000$ after one eddy turnover time are very different. The RDT enstrophy structures lack small scale turbulent structures and are not anisotropic.

are summarized in Table (A.3).

Using RDT models to estimate Rf outside DNS constraints has been previously done by Stretch *et al.* (2010) with $N = 128$ simulations. Fig. (3.32) shows that RDT and DNS predict similar convergence of $\int b dt$ and $\int \epsilon_p dt$. Rf can therefore be estimated as a function of ϵ_p and ϵ_k using Eq. (2.32).

Rf is plotted versus Re_λ in Fig. (3.28) . Rf increasing with Re_λ for all Pr is intuitive as increased stirring will convert kinetic energy more efficiently into potential energy. However, Fig. (3.28) does not suggest Pr effects will diminish with higher Reynolds numbers because Rf for $Pr = 0.1$ increases more rapidly with the Reynolds number than does $Pr = 1$.

In Fig. (3.29), RDT is used to model Rf outside DNS constraints. RDT predicts R_f is Reynolds number independent.

The grid Reynolds number Re_M from grid-tow experiments, defined from mesh geometry and tow velocity, is assumed to be synonymous with Re_0 in DNS, defined from L_0 and u_0. Grid-tow experiments from Rehmann & Koseff (2004) were performed for Re_M ranging from 1300 to 15400, which are substantially higher than $Re_0 = 625$ achieved in DNS. The weak Reynolds number dependence in Fig. (3.28) suggests comparison of DNS with grid-tow

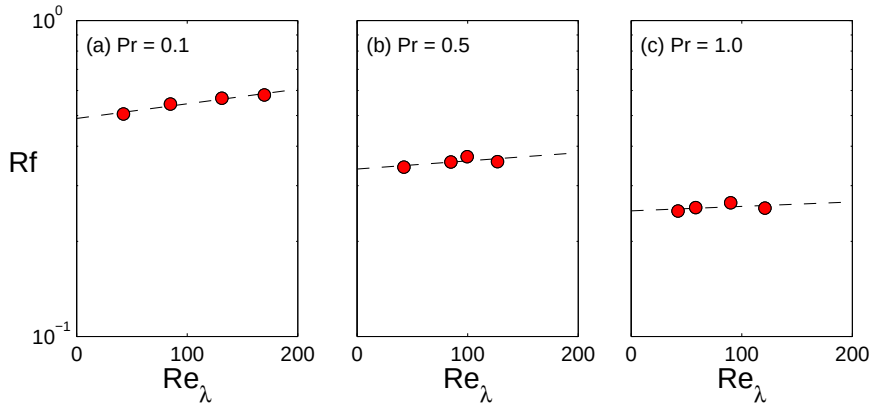

Figure 3.28: Reynolds number effects - To investigate Reynolds number effects, Rf is plotted as a function of the Taylor Reynolds number Re_λ for $Ri = 1000$. The trends suggest small Reynolds number dependence of Rf, and are not clear evidence that Prandtl number effects will decrease at high Reynolds numbers.

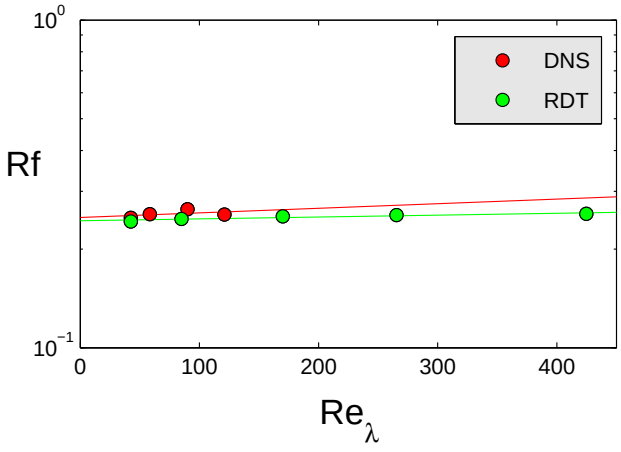

Figure 3.29: RDT and DNS Reynolds number effects - For both DNS and RDT, Rf increases as Re_λ increases. Solid lines are linear regression curve-fits. The Prandtl number is 1.

experiments is appropriate.

Hanazaki & Hunt (1996) showed through dimensional arguments that RDT is not valid for high Reynolds numbers. RDT is essentially a linear wave approximation and therefore a model of the diffusive limit. Density isosurfaces of DNS and RDT are shown in Fig. (3.30). RDT neglects non-linearity, resulting in linear waves traveling continuously through the domain without vertical advective mixing because overturning is absent.

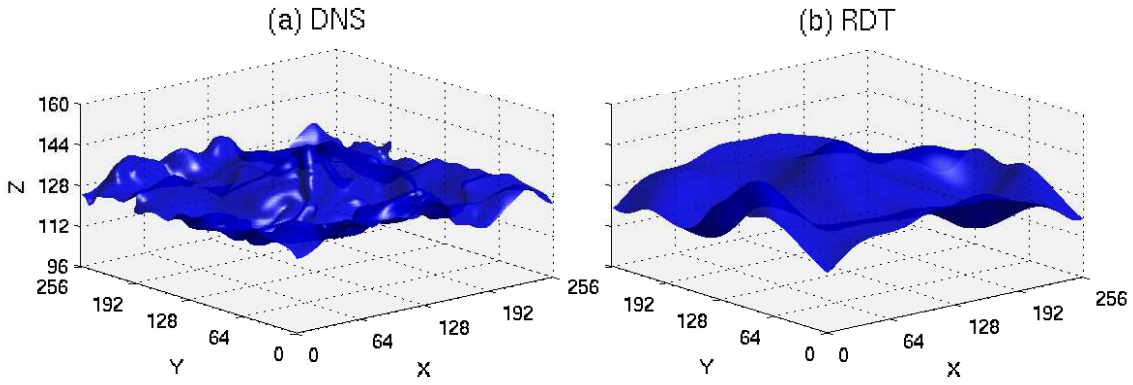

Figure 3.30: Comparison of DNS and RDT density isosurfaces - The density isosurface at the center of the domain is plotted for DNS and RDT. RDT predicts linear internal waves without overturning from unstable conditions.

At high Reynolds numbers, RDT models are still absent of reversible vertical mixing and therefore cannot predict realistic physics of energetic turbulence. The inviscid and non-diffusive limits were explored with a series of RDT models to understand how Rf behaves. This study, summarized in Table (A.4), was performed with Re_0 ranging from 10^2 to 10^6 and with $Pr = 1000$. The results, plotted in Fig. (3.31), predict that mixing at the diffusive limit is independent of Reynolds number. The results are not representative of actual physics as high Reynolds number flows are energetic flow with overturning and RDT neglects all overturning. RDT is therefore only an appropriate model for strongly stratified and diffusive flows.

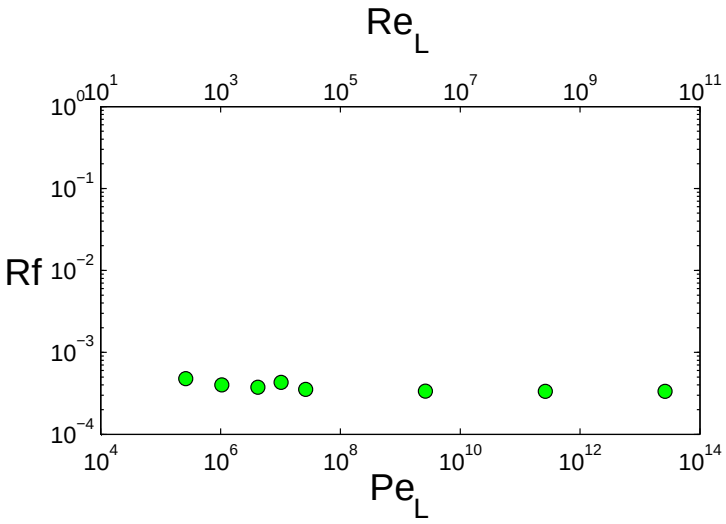

Figure 3.31: Inviscid and non-diffusive limit of RDT - Rf is plotted as a function of the turbulent Reynolds number Re_L and the turbulent Peclet number Pe_L. RDT, a linear wave approximation, predicts equal mixing at all Re_L and Pe_L for $Pr = 1000$.

3.7.3 Prandtl number effects, revisited using RDT simulations

A major shortfall in the comparison between numerical with physical experiments in Sec. (3.6) is that experiments with comparable Pr for strong stratification are not available. The difference between physical and numerical experiments was attributed to the Prandtl number arguments presented in Sec. (3.6.1). In this section the Prandtl number arguments are further explored with a parametric RDT study.

Seven RDT models were run with Pr ranging from 0.1 to 1000. Due to dissipation rates being lower for RDT than DNS, the duration of RDT runs were $20T_0$. All runs analyzed in Prandtl number RDT study are summarized in Table (A.5).

In Sec. (3.6.1) it was argued that Pr effects can be used to explain the difference between physical and numerical experiments. Using DNS and physical experiment for $Ri = 10$, it was found that Rf scales as $Pr^{-0.32}$. However, Rf versus Pr trends at strong stratification could not be further investigated using physical experiments because the highest Ri available from physical experiments is $Ri = 10.7$. Therefore, RDT was used to predict the relationship between Rf and Pr for $Ri = 1000$.

Rf is plotted versus Pr for DNS and RDT in Fig. (3.33). Both DNS and RDT agree

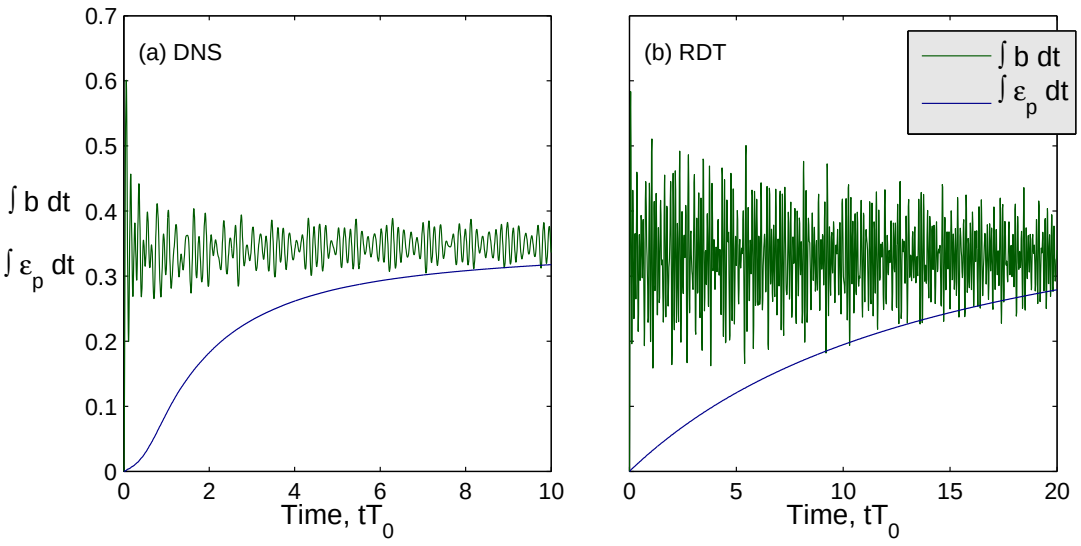

Figure 3.32: Integrated buoyancy flux and potential energy dissipation of DNS and RDT - RDT can be used to approximate Rf using Eq. (2.32) because $\int \epsilon_p dt$ converges with $\int bdt$ at later times.

for small Pr and appear to converge towards 1, which is consistent with theory that the maximum $Rf = 1$ for decaying or stationary turbulence. For high Pr, RDT predicts Rf scales as Pr^{-1}. Stretch *et al.* (2010) found the relationship to be $Rf \sim Pr^{-1/2}$ at lower Reynolds numbers.

3.8 Conclusion

A variety of DNS parametric studies were performed for varying levels of stratification, Prandtl numbers, and Reynolds numbers. Plots of energy cascades revealed a lack of a clear inertial subrange, which is an indication the simulations are diffusive because large, energy containing scales are interacting directly with the small, dissipative scales. Nonetheless, DNS studies continue to be an important avenue to further explore fundamental physics of turbulence flows and the increased resolutions attained in this work are an important improvement upon previous work. The limitations of DNS are illustrated well when simulations are plotted on a buoyancy Reynolds number versus Froude number plane. Simulations are limited to being either moderately stratified and energetic or strongly stratified and diffusive. The ultimate goal is to understand strongly stratified and energetic turbulence.

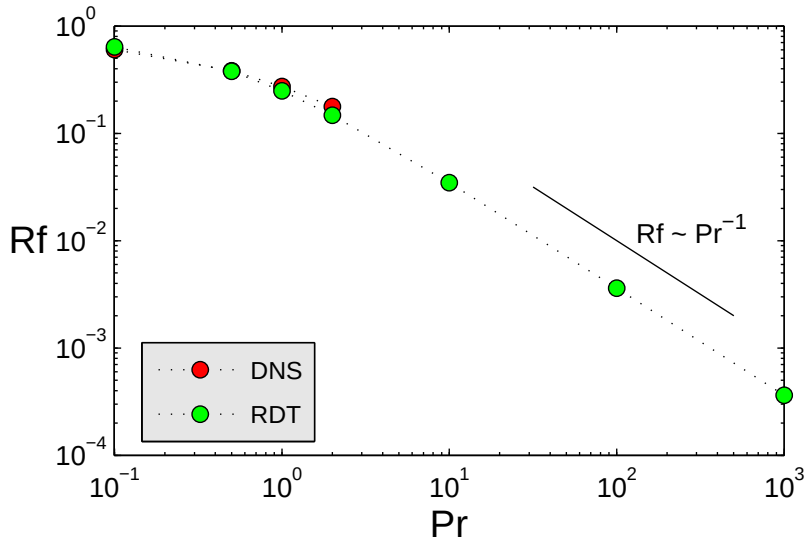

Figure 3.33: RDT estimation of Prandtl number effects for strong stratification - RDT is used to estimate Rf for Pr ranging from 0.1 to 1000. RDT suggests $Rf \sim Pr^{-1}$ for high Pr. At lower Reynolds numbers Stretch *et al.* (2010) found $Rf \sim Pr^{-1/2}$ for high Pr.

Following are summarized conclusions to the main questions addressed in Chapter 3.

(i) What are the dynamics of decaying stratified turbulence at high Reynold numbers?

The external gravity force is only manifested in the governing equations through the buoyancy flux in the vertical Navier-Stokes equation. The buoyancy flux is the mechanism in stratified turbulence which transfers energy between kinetic and potential forms. Turbulent kinetic and potential energy oscillate in anti-phase with the buoyancy frequency, the time scale control of the buoyancy flux. Isotropic turbulence has an equi-partitioning of kinetic energy in all spatial directions. Stratification suppresses vertical motions resulting in kinetic energy to be primarily projected into horizontal directions. Simulations of weakly stratified flows decay very rapidly, while strong stratification reduces the dissipative effect of turbulence and sustains turbulent events.

After initial conditions, dissipation rates increase and peak at approximately one eddy turnover, at which time the flow is fully developed and momentarily stable. Reynolds numbers prior to the decay point after one eddy turnover are unrealistically high given the

numerical restrictions of DNS and have no physical significance. The representative peak Taylor Reynolds numbers of the flow are taken to occur at the decay point, and ranged from 65 for very weak stratification to 130 for very strong stratification.

(ii) What coherent turbulent structures emerge from simulation of decaying stratified turbulence?

Enstrophy plots of weak stratification reveal the presence tall vortex tubes randomly distributed throughout the domain. Vertical motions are suppressed in strong stratification and the enstrophy structures evolve into coherent 'pancake' shaped axisymmetric anisotropic structures. The structures are horizontally layered and move rapidly about their respective layers with minimal vertical interaction between layers. Although the turbulence appears to be two-dimensional, the mechanism is a three-dimensional phenomena due to the existence of a separation of scales in the energy cascade. Shear between layers leads to additional instabilities, which others have argued leads to subsequent overturning and decay of scales.

(iii) What is the dependence of mixing efficiency on stratification, the Reynolds number, and the Prandtl number, and how do trends compare with physical experiments?

The flux Richardson number Rf is a measure of mixing efficiency. Previously used formulations of Rf contained reversible fluxes and required the majority of turbulent kinetic energy to be dissipated for Rf to converge. A formulation of Rf based only on irreversible fluxes was used instead, which allows Rf of moderately and strongly stratified flows to converge within approximately two eddy turnovers.

Both DNS and grid-tow experiments confer that Rf scales differently for three distinct regimes of Ri. Scaling arguments by others show that Rf linearly scales with Ri for weak stratification because the turbulent time scale is the controlling time scale. For strong stratification the controlling time scale is the buoyancy frequency and scaling arguments, grid-tow experiments, and measurements of environmental flows find Rf to be constant and independent of Ri. For strongly stratified DNS, Rf is very dependent on the Prandtl

number and only constant when $Pr \approx 0.5$.

The fundamental inconsistency between results from low Reynolds number laboratory and DNS experiments and highly energetic environmental flows is the strongly stratified and energetic asymptote of mixing efficiency. Models will predict a large difference if a mixing efficiency value of 0.2 or 0.02 is used for the Osborne-Cox parametrization of eddy diffusivity (Ivey *et al.*, 2008). It is argued that the disagreement between grid-tow and DNS experiments for strongly stratified flows is due to both being diffusive, and Rf becomes a property of the fluid. The Prandtl number effects observed in DNS illustrates that Rf is a property of the fluid and could reconcile the difference between DNS, where the maximum Prandtl number is 2, and grid-tow experiments, where the comparable Prandtl number is 700. It stands that for energetic and strongly stratified flows, a combination (to the author's knowledge) not achieved by either DNS or laboratory experiments, Rf will converge to the generally accepted range $0.17 - 0.2$.

(iv) Can rapid-distortion theory (RDT) be used to explain Prandtl number effects?

RDT is a linearization of the governing equations where non-linear advective and diffusive terms are neglected. RDT is a gross approximation of turbulence and is not bound by the numerical constraints of DNS. However, it accurately predicts vertical linear dynamics of very strong stratification, and can therefore be used to estimate Rf. RDT does not predict horizontal dynamics because it is a non-linear process. Flow field visualization of RDT illustrate that RDT is a linear wave approximation without overturning or other non-linear effects. Therefore, RDT neatly illustrates the decoupling effect between vertical and horizontal dynamics of strongly stratified flow.

RDT parametric studies were performed to explore Reynolds number and Prandtl number effects outside DNS constraints. No important Reynolds number trends were found, which confers with work by others that RDT simulations are invalid for high Reynolds number stratified flows. Flow field visualizations reveal that RDT is only comparable to strongly stratified flows in the diffusive limit. RDT predicts Rf in the diffusive limit scale

as Pr^{-1}. Stretch *et al.* (2010) similarly performed RDT simulations and found Rf to scale as $Pr^{-1/2}$.

Chapter 4

Overturns

4.1 Introduction

An overturn is an unstable condition that occurs when a heavier fluid resides above a lighter fluid. The stabilizing effect of gravity will transform the potential energy back into a combination of local turbulent kinetic energy and internal gravity waves, signifying active stirring and mixing. Overturns are an essential process for vertical advective mixing to occur, and lack thereof implies a diffusive flow. The vertical size of an overturn is an insight into flow energetics as the size of an overturn is restricted to the available kinetic energy. Length scales corresponding to overturns are valuable tools to analyze turbulent processes.

The main questions addressed in this section are:

(i) What is the nature of overturning regions in simulations of decaying stratified turbulence?

(ii) What are the relationships between overturning length scales and under what conditions are such relationships appropriate?

Overturning structures observed in DNS are investigated in Sec. (4.2). The nature of a variety of overturning length scales and their relations are explored in Sec. (4.3). Findings are summarized in Sec. (4.4).

4.2 Overturning structures

Overturns occur when a heavier fluid is above a lighter fluid, and can therefore be easily identified in density profiles by 'Z'-shaped signatures. The core of the overturn region is unstable (i.e. $\partial\rho/\partial z > 0$) while the top and bottom are stable. It is not a simple process to identify an entire overturning structure as one must decide where the overturn begins and

ends. Additionally, the interaction of overturning structures in active turbulence blurs the distinction between individual structures. However, the cores can be identified as positive regions of vertical density gradients.

The dependence of overturns on stratification and their temporal evolution is discussed in Sec. (4.2.1). The relation between overturning structures of vorticity is analyzed in Sec. (4.2.2). A single overturn is further explored in Sec. (4.2.3).

4.2.1 Overturns and stratification

The nature of overturning regions are strongly dependent on the strength of stratification. Cross-sections of density fields are plotted in Fig. (4.1) for weak, moderate, and strong stratification. It is difficult to discern individual overturning events for weak stratification as there is strong interaction between structures. The size of overturning structures for the moderately stratified case qualitatively appear smaller. The strongly stratified case contains no visible overturning, but rather gentle density fluctuations signifying internal gravity waves.

The evolution of unstable regions is plotted in Fig. (4.2). The weak stratification case contains much overturning and is highly energetic. The moderate stratification case is initially energetic with much overturning but becomes stable as the total energy decreases to low levels after about four eddy turnover times. The strong stratification case is extremely stable without any overturning structures captured. Overturning structures do exist (see Thorpe scale measurements in Table B.1) but have very short lifespans.

4.2.2 Overturns and vorticity

It is has been suggested by Lindborg (2006) that vertically layered 'pancake' vortex structures in strongly stratified turbulence produce local shear instabilities due to sharp vertical gradients and subsequent overturning. Unstable regions are plotted with the enstrophy field in Fig. (4.3). Overturns appear to be concentrated around regions of high enstrophy.

To further investigate the nature of overturning structures, probability density functions (PDFs) of vorticity inside and outside overturning regions are plotted in Figs. (4.4)-(4.6).

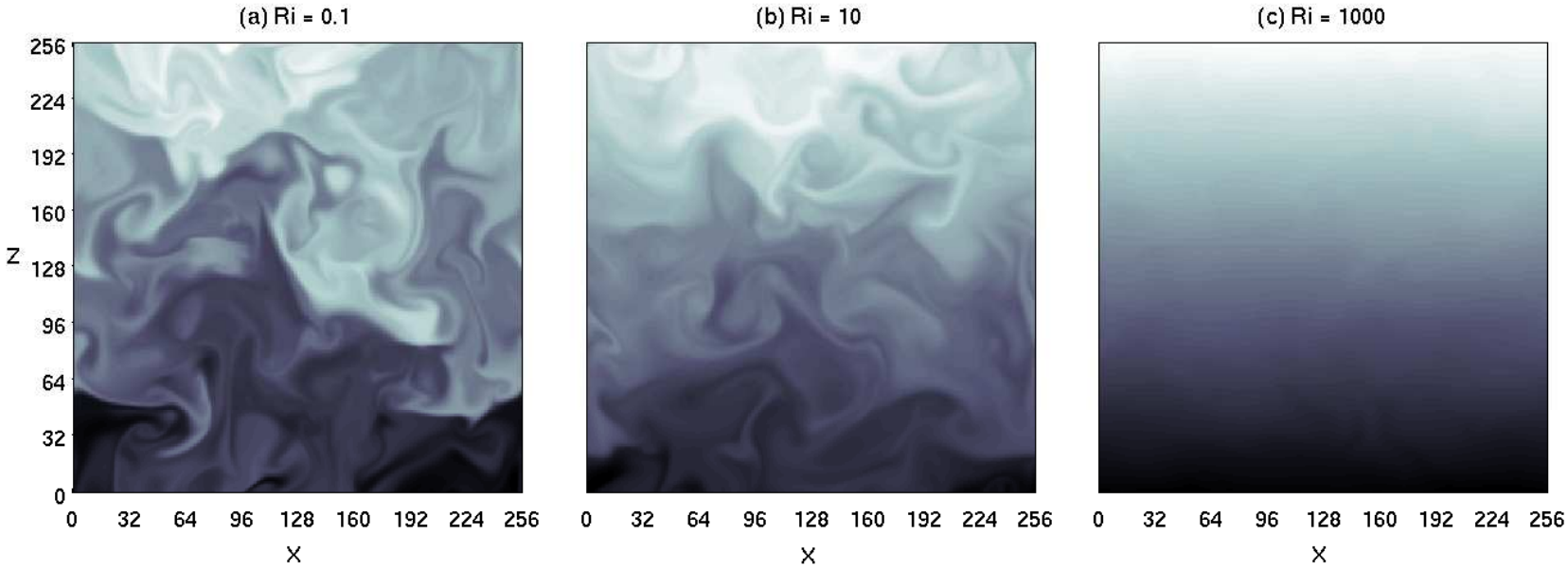

Figure 4.1: Cross-section of density fields - The cross-section of the density field through the center of the domain (i.e. $y = 128$) at $t = 1u_0/L_0$ reveals strong overturning for $Ri = 0.1$ and 10. The case for $Ri = 1000$ contains horizontal density gradients signifying internal gravity waves but is primarily gravitationally stable.

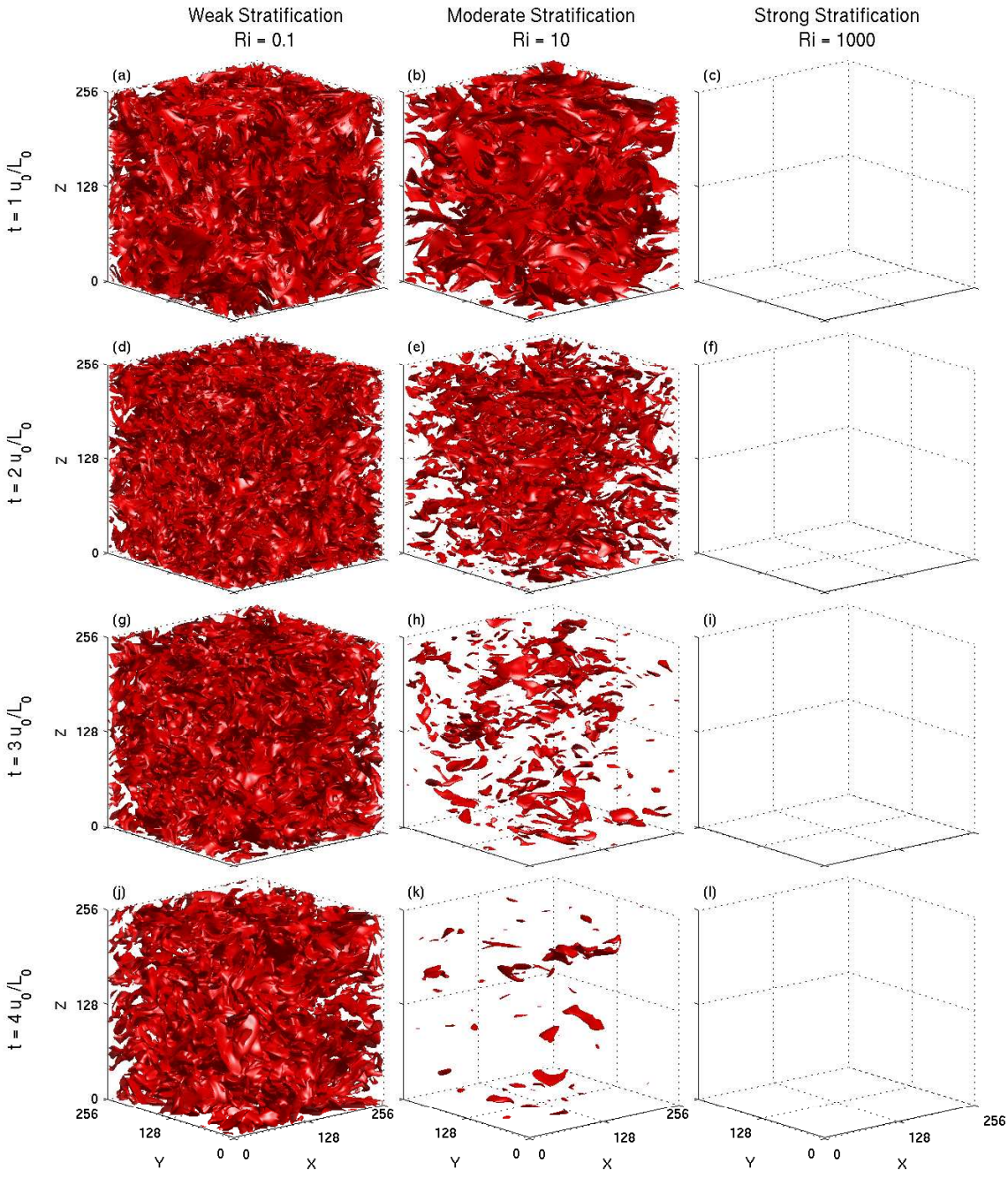

Figure 4.2: Evolution of unstable regions - Instability isosurfaces for $Ri = 0.1, 10, 1000$ at eddy turnover times 1-4. The isosurface level $\partial\rho/\partial z = 0$ marks the core of overturning structures.

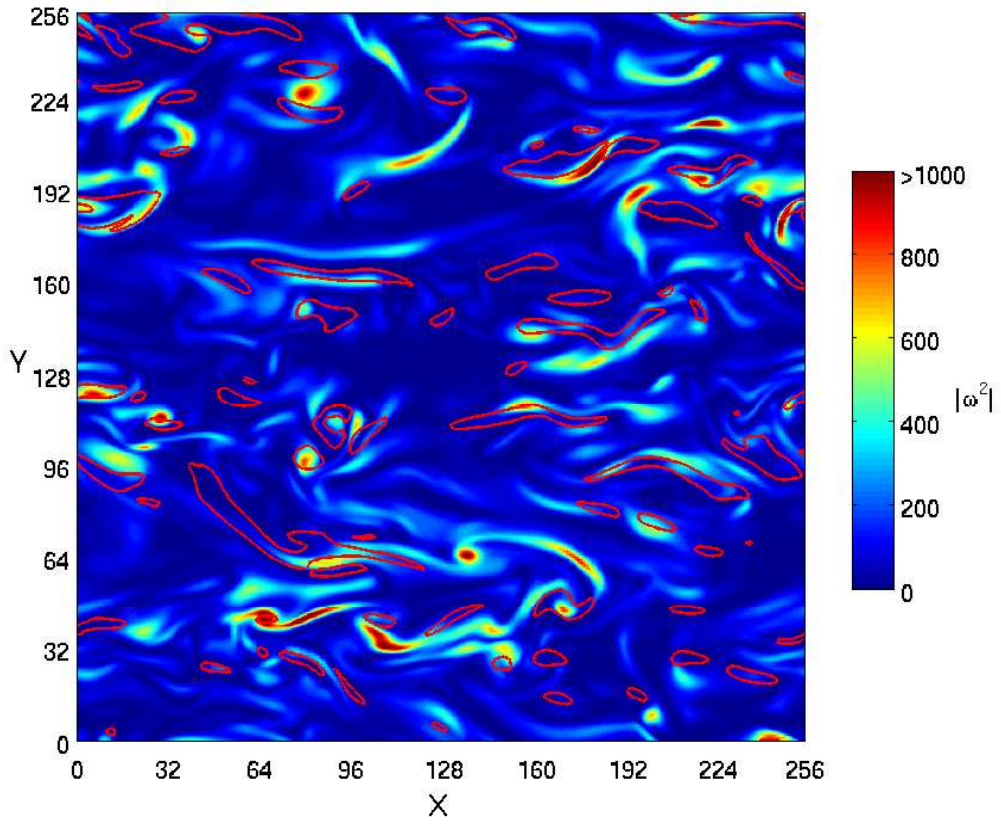

Figure 4.3: Unstable regions in enstrophy field - Unstable regions are outlined in red on enstrophy field. Flow field is for $Ri = 40$ at $t = 2u_0/L_0$ at $y = 96$.

For weak stratification, the average vorticity inside and outside overturns is approximately equal. The PDFs of horizontal and vertical vorticity for weakly stratified turbulence are similarly distributed but the mean vertical vorticity is much lower than the mean horizontal vorticity. As stratification increases overturning structures are increasingly correlated with regions of higher horizontal vorticity while the PDFs of vertical vorticity is approximately constant. For strong stratification, overturning structures are strongly correlated with high enstrophy.

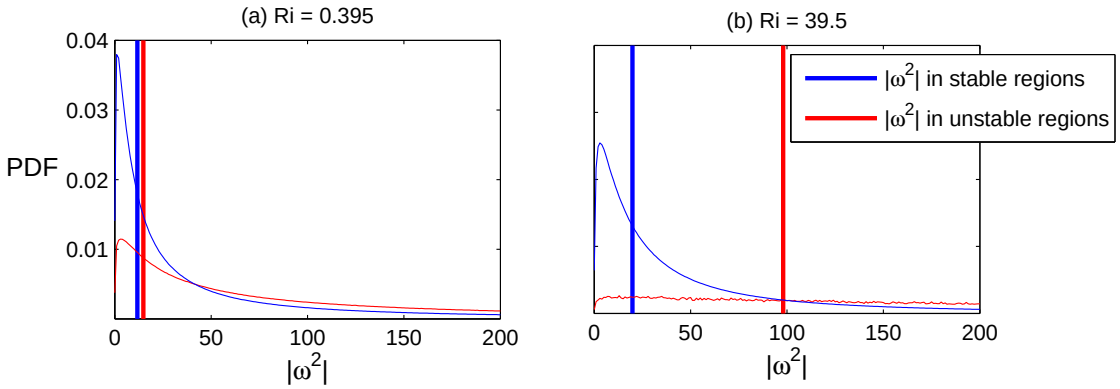

Figure 4.4: PDF of enstrophy inside and outside unstable regions - Mean values are represented with vertical bars. The sampling bin size is $1|\omega^2|$. Statistics were calculated for parameter fields from 1-5 eddy turnovers at $0.25T_0$ intervals.

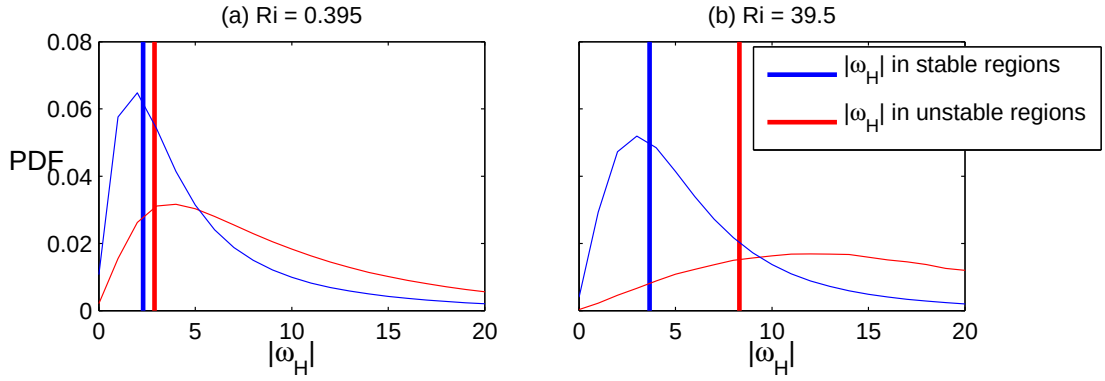

Figure 4.5: PDF of horizontal vorticity inside and outside unstable regions - Mean values are represented with vertical bars. The sampling bin size is $1|\omega_H|$. Statistics were calculated for parameter fields from 1-5 eddy turnovers at $0.25T_0$ intervals.

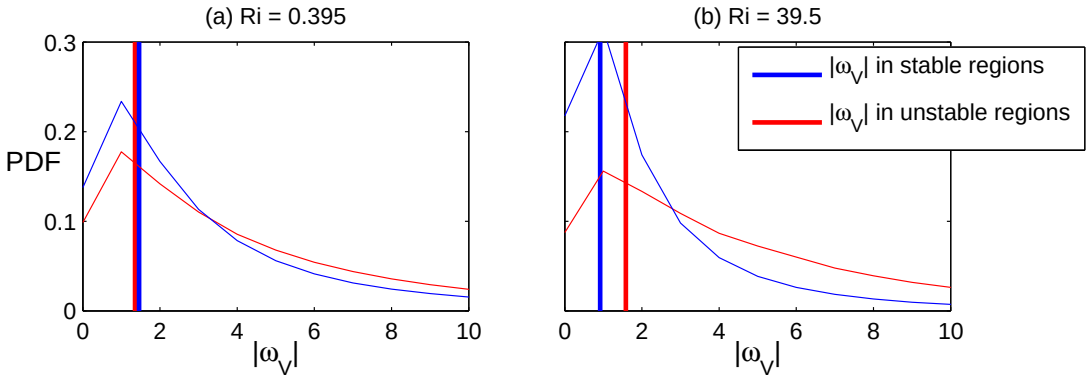

Figure 4.6: PDF of vertical vorticity inside and outside unstable regions - Mean values are represented with vertical bars. The sampling bin size is $1|\omega_V|$. Statistics were calculated for parameter fields from 1-5 eddy turnovers at $0.25T_0$ intervals.

4.2.3 Investigation of an overturn

An overturn for $Ri = 40$ is plotted in Fig. (4.7). The overturn region contains both stable and unstable regions. The boundary of the unstable region is plotted in Fig. (4.7a). The 'Z'-shaped signature can be clearly seen on the density profile in Fig. (4.7b). Defining the boundary of an overturn can be vague as overturning structures should be larger than just the unstable region. Sorting individual profiles allows for the top and bottom bounds of the overturn to be defined as where the density profile reattaches to the sorted profile. The top and bottom bounds are also shown in Fig. (4.7b). This classification method defines overturning structures as much larger than just the unstable regions.

The density field and vorticity fields of the same overturn are plotted in Fig. (4.8). An overturn classically forms from breaking internal waves or a large vertical vortex. The ambient fluid is wrapped into the vortex core resulting in unstable isopycnals (Diamessis & Nomura, 2004). The unstable region will collapse into smaller turbulent eddies. Although overturns are a vertical process, the core of the overturning structure is primarily associated with horizontal vorticity rather than vertical vorticity. The localized horizontal vorticity may have produced a horizontal shear instability which resulted in low, but sufficient, vertical vorticity for ambinet fluid to be wrapped into the vortex core. Overturns may also form from horizontal vorticity when lighter fluid is rotated into heavier fluid.

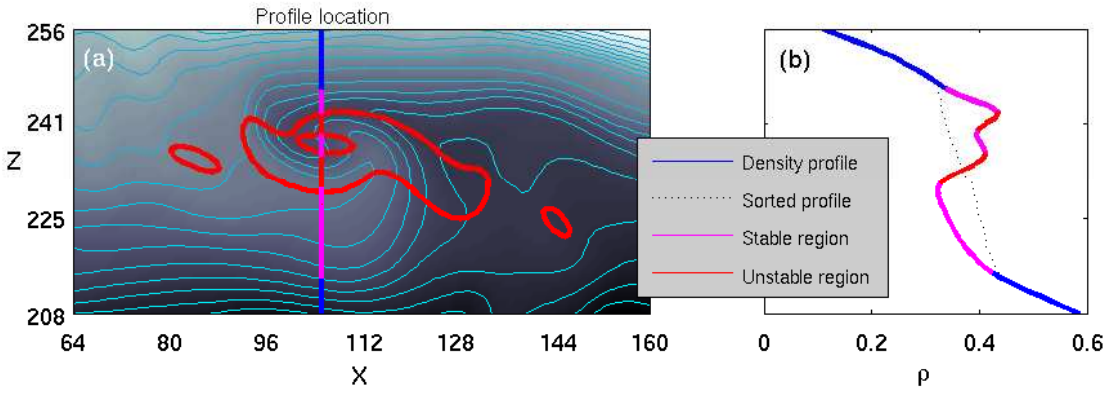

Figure 4.7: Density field and profile of an overturn - In (a) the boundary of the unstable region is plotted on the density field in red. A density profile through the center of the overturn is shown in (b). The top and bottom bounds of the overturn are defined as where the density profile reattaches to the sorted profile. The overturn is for $Ri = 40$ at $t = 2.5u_0/L_0$ and $y = 64$.

4.3 Overturning length scales

Overturns are commonly characterized with the Thorpe and Ozmidov length scales. In Sec. (4.3.1) two formulations of the Thorpe scale, L_T and L_{T3D}, are compared. In Sec. (4.3.2) the relationship between Ozmidov and Thorpe scales is explored. Dissipation rates are commonly inferred from the assumption that $L_T \approx L_O$, which is explored in Sec. (4.3.3). A variety of other length scales characterizing the energy containing range are compared with the Thorpe scale in Sec. (4.3.4).

4.3.1 The Thorpe scale

The Thorpe scale, reviewed in Sec. (2.4.8), is a measure of the mean vertical displacement d' that a particle must travel to a gravitationally stable position. Two different Thorpe scales are discussed in this section; the classic Thorpe scale L_T and the 3D Thorpe scale L_{T3D}.

The Thorpe displacements d' to calculate L_T are determined by sorting a single density profile for gravitational stability and calculating vertical displacements of particles. L_T is calculated from individual profiles, which may vary considerably. The spatial ensemble-average L_T removes statistical variation and provides a better measure of overturns. Oceanog-

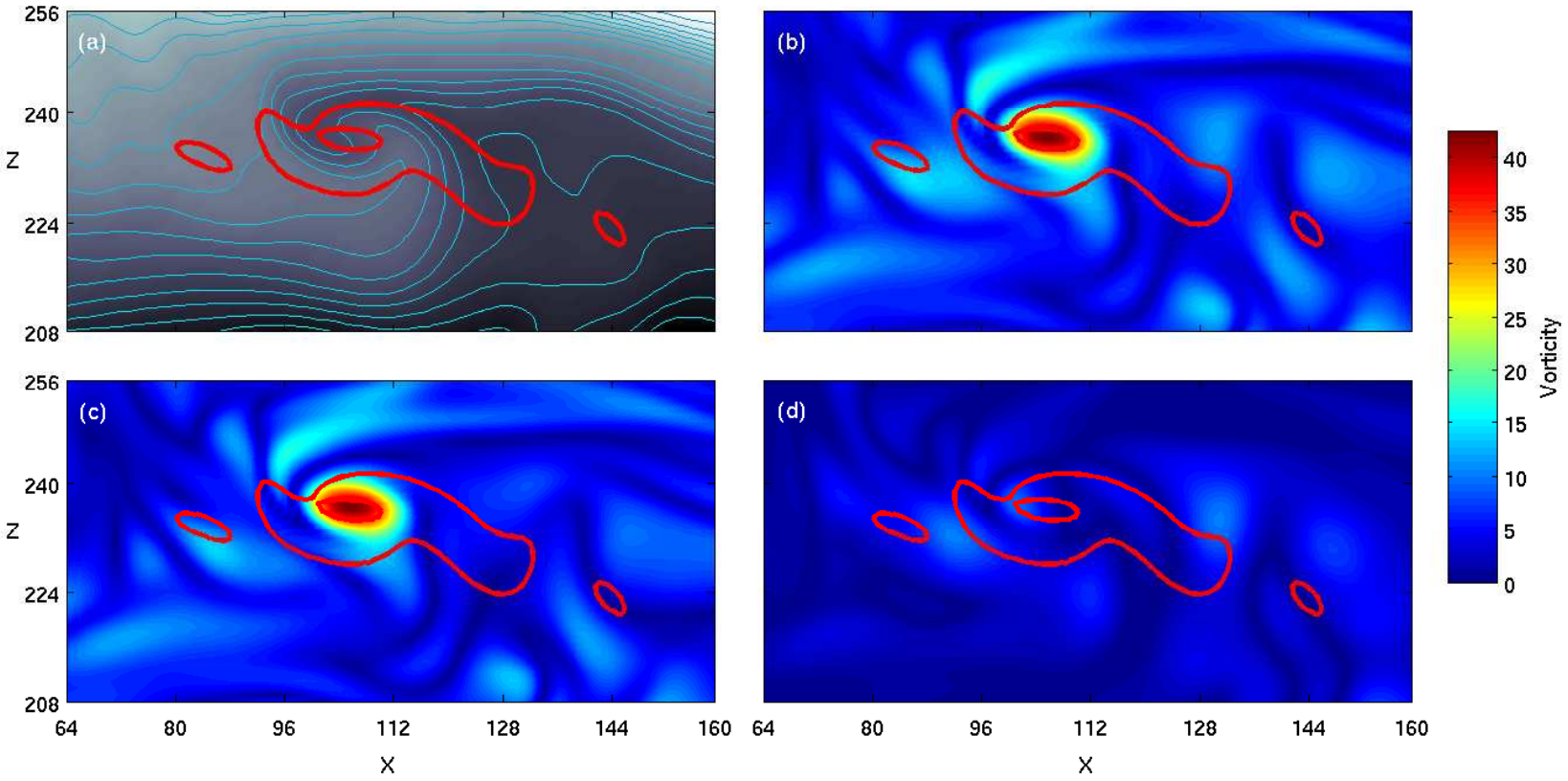

Figure 4.8: Vorticity fields of an overturn - The density profile of an overturn is shown in (a) with the boundary of the unstable region marked in red. The total vorticity $|\omega|$ is plotted in (b), the horizontal vorticity $|\omega_H|$ is plotted in (c), and the vertical vorticity $|\omega_V|$ is plotted in (d). The core of the unstable region is associated with high horizontal vorticity and low vertical vorticity. The overturn is for $Ri = 40$ at $t = 2.5u_0/L_0$ and $y = 64$.

raphers use many measurements to increase the accuracy of L_T. The procedure to calculate L_T is described in Appx. (B). Calculated L_T and corresponding standard deviations are tabulated in Table (B.1). Hereafter L_T implies an ensemble-average Thorpe scale.

In regions of density fluctuations but void of overturns, such as a stable internal gravity wave, the density profile and sorted density profile $\langle\rho\rangle$ are equal resulting in zero d'. L_T is only calculated from non-zero d' and is therefore solely a measure of overturns and not of stable scalar fluctuations. The 3D Thorpe scale L_{T3D} includes the effect of stable density fluctuations, where d' are calculated from a globally sorted density profile $\langle\rho\rangle_{3D}$. The procedure to calculate $\langle\rho\rangle_{3D}$ is described in Appx. (B). The benefits of sorting an entire domain is that lateral instabilities are avoided and $\langle\rho\rangle_{3D}$ becomes a measure of the background density profile.

Individual and 3D sorted density profiles are compared with the instantaneous density profile in Fig. (4.9). It can be seen in Fig. (4.9b) that displacements from $\langle\rho\rangle$ are very small or zero while displacements from $\langle\rho\rangle_{3D}$ are much larger and non-zero. Even for very stable profiles d' are usually non-zero due to stable scalar fluctuations such as internal gravity waves, which contribute to the magnitude of L_{T3D}. L_{T3D} is a length scale characterizing scalar fluctuations rather than specifically overturning structures.

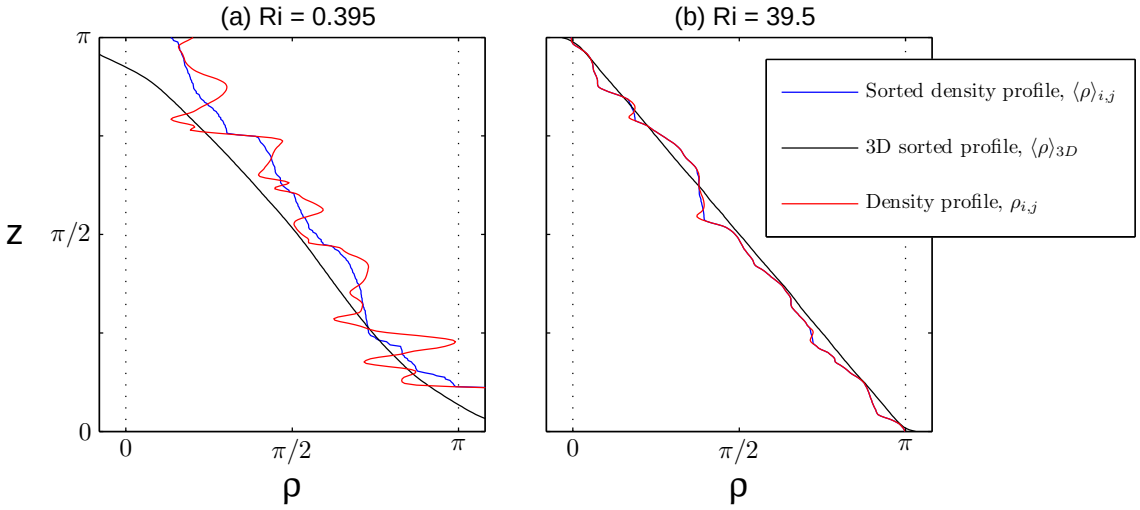

Figure 4.9: Individual and 3D sorted density profiles - The density profile ρ through the center of the domain (i.e. $x = 128, y = 128$) is plotted with the corresponding sorted density profiles $\langle\rho\rangle$ and the 3D sorted density profile $\langle\rho\rangle_{3D}$.

The two Thorpe scales are plotted for all Ri with $Pr = 1$ in Fig. (4.10). There is good agreement between L_T and L_{T3D} except at high Ri. At $Ri = 1000$ after $2T_0$ the flow is very diffusive without overturns resulting in zero L_T while L_{T3D} is continues to be non-zero. Although L_{T3D} is a measure of general scalar fluctuations and L_T of actual overturns, there is good agreement between the two Thorpe scale formulations. The simulations were initialized with $L_0 = 1$ as the size of the largest eddies. As the simulations are decaying it stands that the largest eddies should be smaller than L_0 for low stratification and much smaller than L_0 for strong stratification due to the decaying behavior of turbulence. The largest Thorpe scales in Fig. (4.10) are approximately equal to L_0.

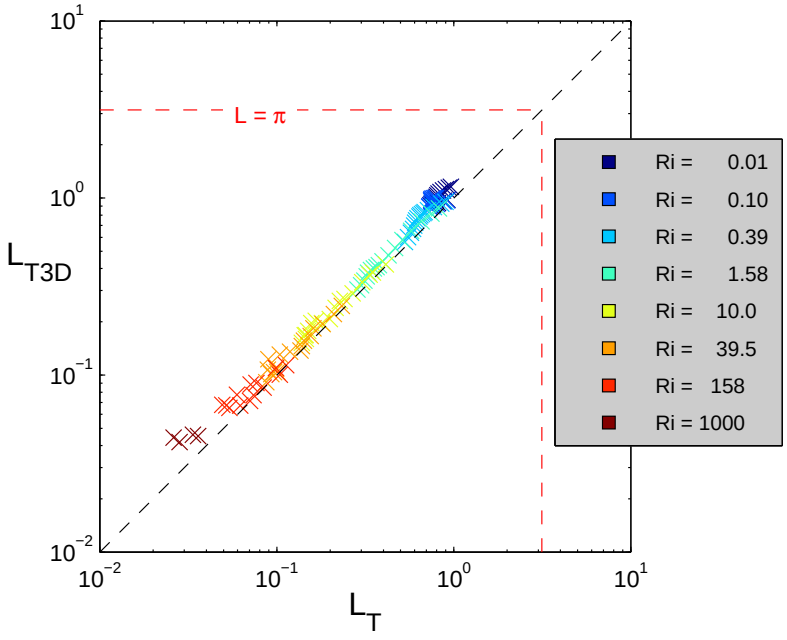

Figure 4.10: Comparison of ensemble-average and 3D Thorpe scales - Although L_{T3D} is a measure of general scalar fluctuations and L_T of actual overturns, there is good agreement between the two Thorpe scale formulations. Thorpe scales are calculated for $Pr = 1$ at 1-5 eddy turnovers with $0.25T_0$ increments.

4.3.2 Thorpe-Ozmidov relation

The Ozmidov scale L_O is a measure of the largest overturn possible based on dimensional arguments of inertial effects using ϵ_k and buoyancy effects using N. A very widely used assumption in oceanography is that L_T is of order and linearly related to L_O. However, L_T

is a statistical quantity based on measurements and there is no rigorous relation between L_O and L_T. The assumption $L_O \approx L_T$ is very valuable as L_T is easily measured and equating the two provides knowledge about dissipation rates. However, it is not appropriate for all flow conditions. From oceanography data Dillon (1982) found that $L_O = 0.8L_T$ in the interior of wind-forced regions and in the thermocline. For near-surface measurements Dillon did not find clear correlations between L_O and L_T. Dillon attributes the discrepancy at near-surface flows to intermittency with non-constant stratification and dissipation rates (i.e. varying flux and gradient Richardson numbers).

L_T and L_O are plotted in Fig. (4.11). Using linear regression the two scales are related as $L_O = 1.40L_T^{1.69}$, a non-linear relation. L_T grows more than one order of magnitude larger/smaller than L_O at very low/high Ri.

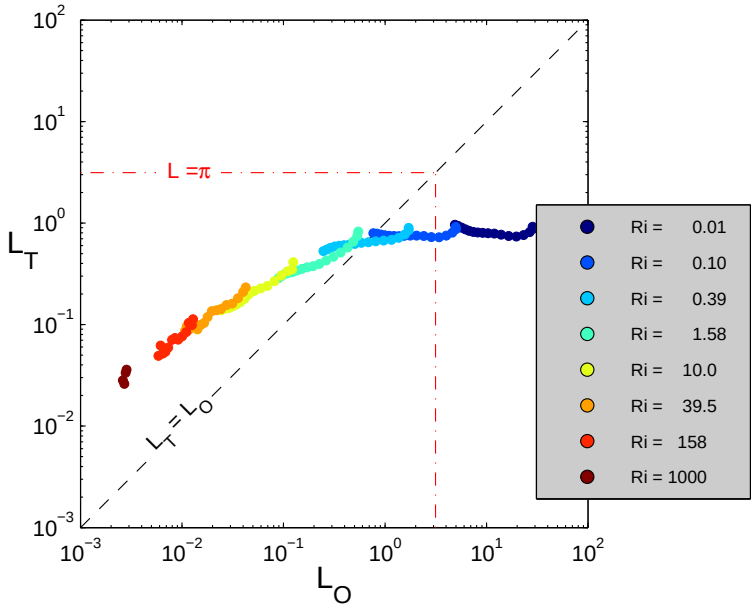

Figure 4.11: Ozmidov and Thorpe scale relation - The Thorpe scale L_T and Ozmidov scale L_O are plotted for times $t = 1$ to 5 at $0.25t$ intervals. L_T and L_O are not linearly related and L_T is more than one order of magnitude larger/smaller than L_O at low/high Ri. Time evolutions for each Ri are approximately from right to left.

In Fig. (4.11) the Thorpe scales appear to converge on the initial scale L_0 while L_O grows up to an order of magnitude larger than the domain size $\mathcal{L}$. The flow type at low Ri changes from a simulation comparable to deep ocean turbulence to a flow with a "cap",

such as the ocean bottom or a sill. L_O loses traditional interpretation as eddies larger than L_0 are predicted. As stratification goes to zero L_O grows to infinity. Thus, at the weakly stratified limit the assumption $L_T \approx L_O$ is an inappropriate assumption.

The Thorpe-Ozmidov relation L_T/L_O is plotted as a function of Re_L in Fig. (4.12). The spread of Reynolds numbers is too small to conclusively discern trends because all runs are initialized with identical Reynolds numbers. The single order of magnitude Re_L spans suggests $L_T \approx L_O$ is an appropriate assumption for lower Reynolds number flows. However, this observation is inconsistent with very high Reynolds number ocean measurements where good agreement has been claimed.

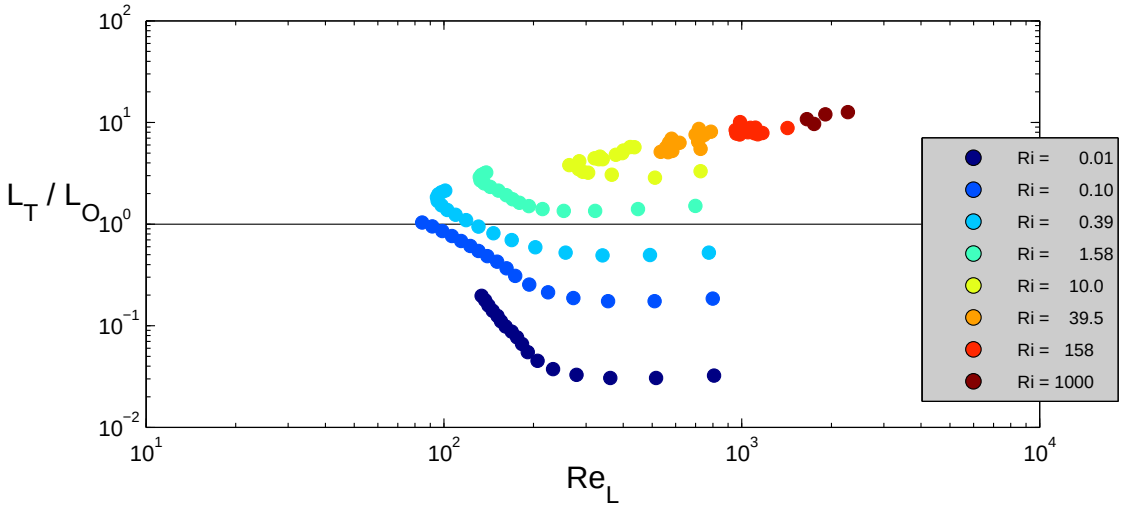

Figure 4.12: Reynolds number influence on Thorpe-Ozmidov relation - The relationship between L_T and L_O is plotted as a function of the turbulent Reynolds number Re_L. The Reynolds number span is very small due to all runs being initialized with the same Reynolds number.

The turbulent Froude number spans a much larger range than Re_L. L_T/L_O is plotted as a function of Fr in Fig. (4.13). When $Fr > 1$ the flow is energetic and dissipation exceeds the available potential energy in overturns resulting in the rapid decay of events, but when $Fr < 1$ dissipation is less than the available potential energy in overturns and the potential energy must be balanced by kinetic energy fluctuations (Ivey & Imberger, 1990). Fig. (4.13) suggests $L_T \approx L_O$ is only valid when Fr is equal to unity. The condition where $Fr = 1$ is a critical point where buoyancy and inertial effects balanced.

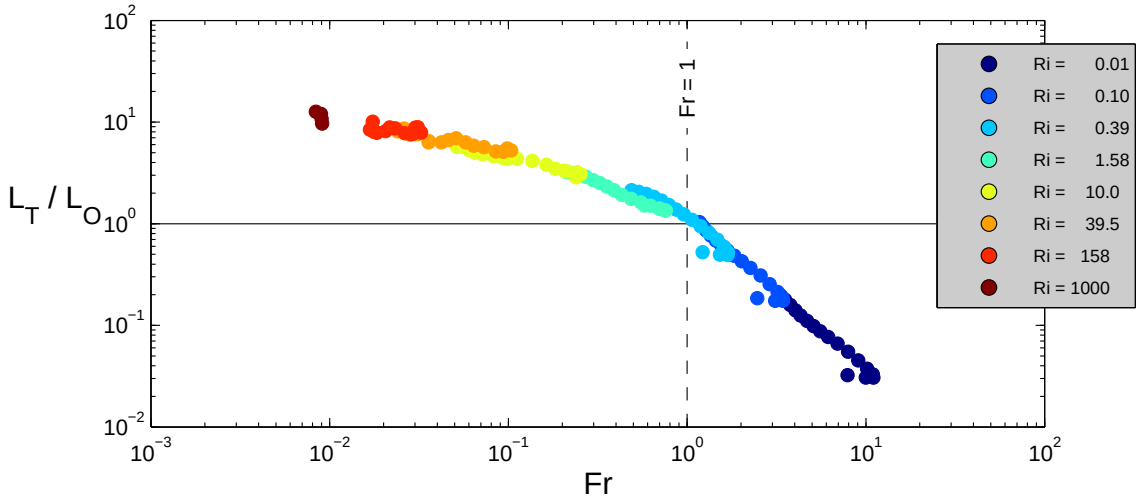

Figure 4.13: Froude number influence on Thorpe-Ozmidov relation - The relationship between L_T and L_O is plotted as a function of the turbulent Froude number Fr. Fig. (4.13) suggests $L_T \approx L_O$ is only valid when Fr is equal to unity.

The buoyancy Reynolds number R_b is a mixed parameter as it can be constructed from Fr and Re_L and captures combined trends. L_T/L_O is plotted as a function of R_b in Fig. (4.14). The assumption $L_T \approx L_O$ appears to be most appropriate at the transition between the intermediate and energetic regimes. Due to R_b being primarily a function of Fr as it spans multiple orders of magnitudes and is second order in Eq. (3.8), Reynolds number effects are suppressed in Fig. (4.14). Thus, DNS with a larger range of Reynolds numbers may contain different R_b trends.

4.3.3 Inferred dissipation

The kinetic energy dissipation rate ϵ_k is commonly inferred from the assumption that $L_T = CL_O$, where C is a regression coefficient commonly set as 0.8 (Thorpe, 2005), such that the inferred kinetic energy dissipation rate ϵ_T is

$$\epsilon_T = CL_T^2 N^3. \tag{4.1}$$

The inferred dissipation rates are plotted as a function of actual dissipation rates in Fig. (4.15). It can be seen that ϵ_T scales as ϵ_k for $Ri = 1.58$ and greater but grows up to two orders

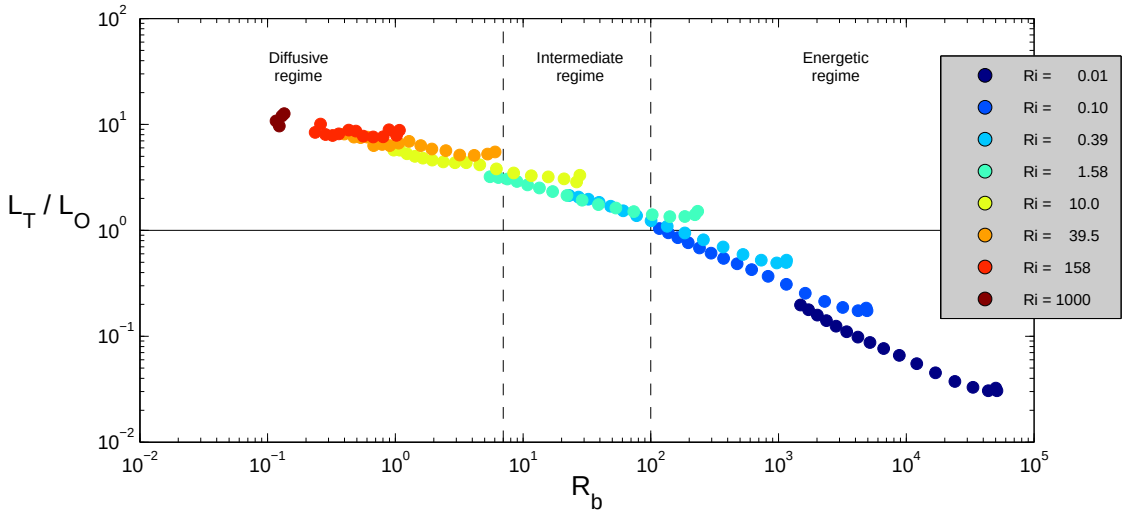

Figure 4.14: Turbulent Reynolds number influence on Thorpe-Ozmidov relation - The relationship between L_T and L_O is plotted as a function of the buoyancy Reynolds number R_b. Additionally, the R_b regimes defined by Shih *et al.* are plotted to quantify the energy level of the flow. Time evolutions for each Ri are approximately from right to left.

of magnitude larger. For low Ri the ϵ_T is independent of ϵ_k and underestimates ϵ_k by multiple orders. The error associated with the assumption $L_T \approx L_O$ is very large for the simulationed cases.

4.3.4 Other important length scale relations

The turbulent length scale L (Eq. 2.52) is plotted versus L_T in Fig. (4.16). The turbulent length scale characterizes the largest eddies in isotropic turbulence. Thus, for weakly stratified turbulence L should be an approximate measure of the largest eddies, which should be smaller than the initial length scale L_0. In Fig. (4.16) it can be seen that for weakly stratified turbulence L agrees well with L_T estimates that the largest eddies are slightly smaller than L_0. However, L does not agree with L_T for anisotropic turbulence with moderate and strong stratification. For strong stratification L is multiple orders larger than L_T.

The buoyancy scale L_b (Eq. 2.54) is the vertical distance a particle could travel if all vertical kinetic energy were transferred into potential energy. L_B is plotted versus L_T in Fig. (4.17). For weak and moderate stratification L_b is significantly smaller than L_T, suggesting horizontal kinetic energy is an important mechanism for overturning. As strat-

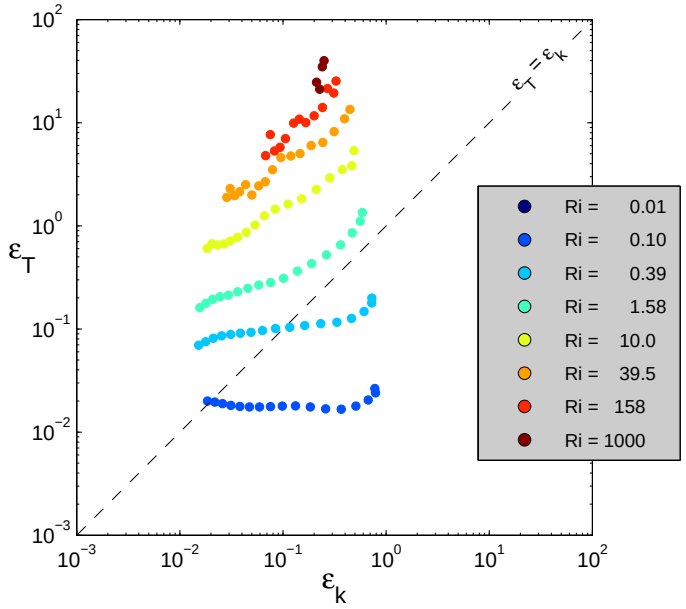

Figure 4.15: Inferred versus actual dissipation rates - The inferred dissipation rate ϵ_T from L_T grows larger than the actual dissipation rate ϵ_k as Ri increases until $Ri > 158$, after which ϵ_T relative to ϵ_k decreases. The inferred dissipation rate ϵ_{T3D} from L_{T3D} grows larger than ϵ_k as Ri increases for all Ri.

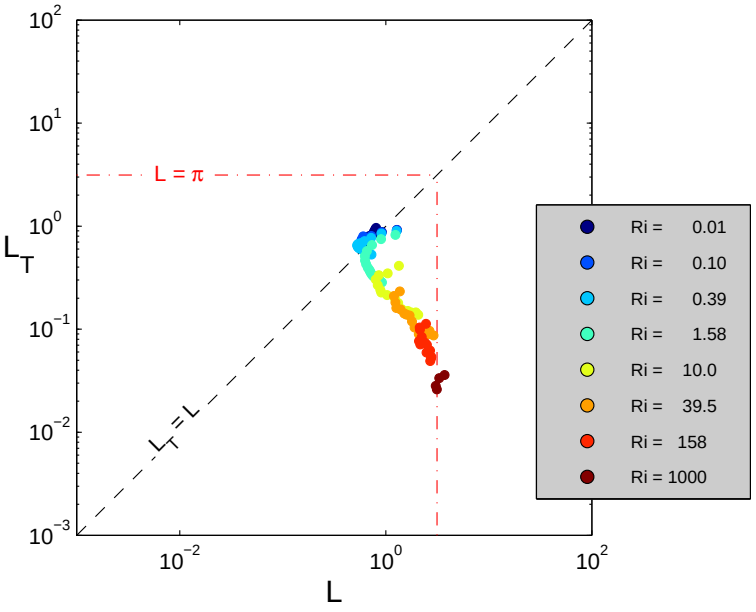

Figure 4.16: Turbulent scale and Thorpe scale relation - The Thorpe scale L_T and turbulent scale L are plotted for times t = 1-5 at $0.25T_0$ intervals. L and L_T only agree for weakly stratified isotropic turbulence.

ification goes to zero, L_b grows infinitely large. Thus, for weak stratification L_b loses interpretation as the vertical height of overturns.

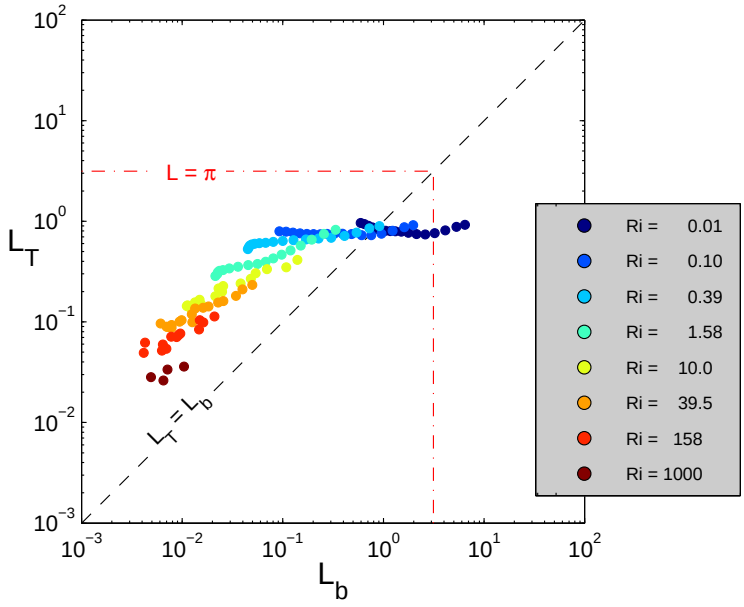

Figure 4.17: Buoyancy scale and Thorpe scale relation - The Thorpe scale L_T and buoyancy scale L_b are plotted for times t = 1-5 at $0.25T_0$ intervals.

The Ellison scale L_E is a measure of scalar fluctuations similar to L_{T3D}. L_E is plotted versus L_T in Fig. (4.18). In agreement with findings by Itsweire (1984) and Smyth *et al.* (2001), it can be seen that L_E and L_T agree well for all Ri.

4.4 Conclusion

Following are summarized conclusions to the main questions addressed in Chapter 4.

(i) What is the nature of overturning regions in simulations of decaying stratified turbulence?

The prevalence of overturning regions is dependent on the strength of stratification. Strongly stratified flows are very stable resulting in small overturns with short lifetimes. The classic overturn forms from a breaking gravity wave or other large vortex. The ambient fluid is wrapped inside the vortex against gravity creating instabilities. Statistical analysis showed

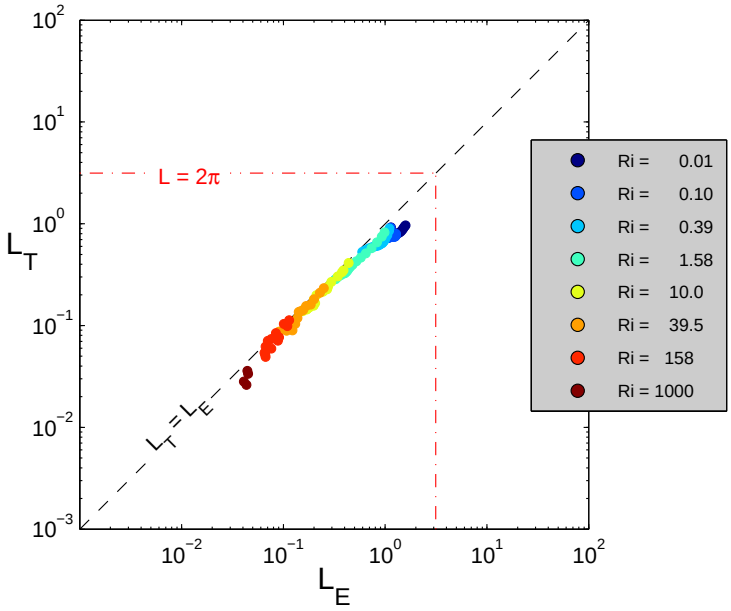

Figure 4.18: Ellison scale and Thorpe scale relation - The Thorpe scale L_T and Ellison scale L_E are plotted for times t = 1-5 at $0.25T_0$ intervals.

overturns to be correlated with horizontal vorticity for strong stratification. Others have suggested that overturns form from local shear instabilities from sharp local gradients between 'pancake' shaped enstrophy structures. Another potential formation of overturns in strongly stratified flows is when horizontal vorticity rotates a lighter into heavier fluid.

Overturn structures are characterized with unstable regions and are identified on density profiles with 'Z'-shaped signatures. A method to discern the larger overturning structure not limited to the unstable region is to gravitationally sort the profile and locate the points where the sorted profile reattaches to the original profile.

(ii) What are the relationships between overturning length scales and under what conditions are such relationships appropriate?

The Thorpe scale is an objective measure of the height of overturns. The traditional Thorpe scale L_T is only a measure of vertical instability within a single profile while the 3D Thorpe scale L_{T3D} incorporates horizontal instability by globally sorting density. It was found that L_T agrees well with L_{T3D} except at strong stratification where L_{T3D} is sensitive linear waves while L_T is not. Investigations revealed L_T does not scale linearly with the Ozmidov scale

L_O and is up to multiple orders larger/smaller for strong/weak stratification. The only region with good agreement between L_T and L_O is where Fr is equal to unity. The findings that L_T is not equal to L_O has important implications for oceanography, where the two length scales are commonly assumed to be equal. Equating L_T and L_O allows for the kinetic energy dissipation rates to be inferred from density profiles. Inferred dissipation rates were compared with actual rates and it was found that dissipation rates are overestimated by up to two orders of magnitude.

The turbulent length scale L corresponds well with L_T when the flow is weakly stratified and isotropic. For strong stratification, L is multiple orders of magnitude larger than L_T. The buoyancy scale L_b is overestimated by L_T, which suggests contributions of horizontal kinetic energy are important to overturning mechanisms. The Ellison scale L_E agreed well with L_T for all Ri because the sorted density profiles similar to the background density profile.

Chapter 5

Conclusion

5.1 Summary of studies

DNS was used to better understand the dynamics of decaying stratified turbulence in this work. DNS parametric studies with varying stratification, Prandtl numbers, and Reynolds numbers were performed for Chapter 3. A focus in Chapter 3 is on mixing efficiency and its relation to stratification and Prandtl number effects. Mixing efficiency from DNS and physical experiments were compared. To further investigate trends in DNS, RDT was used to predict mixing efficiencies outside DNS constraints. RDT parametric studies were performed for varying Prandtl numbers, Reynolds numbers, and to explore the inviscid and non-diffusive limit.

Chapter 4 is the second portion of this work. The focus is on the nature of overturns and relationships between overturning length scales. Results from the main DNS parametric study with Prandtl numbers equal to unity were used. The nature of overturning structures were explored using flow visualizations of density and vorticity. Overturning length scales were explored by comparing the Thorpe scale, a length scale directly measured from density fields, with other important length scales based on dimensional arguments.

The main conclusions from Chapter 3 are summarized in Sec. (5.2) and the main conclusions from Chapter 4 in Sec. (5.3). Recommendations for further work are given in Sec. (5.4).

5.2 Conclusions from Chapter 3

A variety of DNS parametric studies were performed for varying levels of stratification, Prandtl numbers, and Reynolds numbers. Plots of energy cascades revealed a lack of a clear inertial subrange, which is an indication the simulations are diffusive because large, energy

containing scales are interacting directly with the small, dissipative scales. Nonetheless, DNS studies continue to be an important avenue to further explore fundamental physics of turbulence flows and the increased resolutions attained in this work are an important improvement upon previous work.

The external gravity force is only manifested in the governing equations through the buoyancy flux in the vertical Navier-Stokes equation. The buoyancy flux is the mechanism in stratified turbulence which transfers energy between kinetic and potential forms. Isotropic turbulence has an equi-partitioning of kinetic energy in all spatial directions. Stratification suppresses vertical motions resulting in kinetic energy to be primarily projected into horizontal directions. Simulations of weakly stratified flows decay very rapidly, while strong stratification reduces the dissipative effect of turbulence and sustains turbulent events.

As stratification increases the flow becomes more anisotropic and kinetic energy is predominantly directed into horizontal directions. An analysis of flow structures reveals the formation of 'pancake' shaped enstrophy structures for strong stratification. These structures can move rapidly within their respective planes but there is little interaction in the vertical direction suggesting a decoupling between horizontal and vertical dynamics at strong stratification. RDT models, which neglect non-linear terms, were found to accurately predict vertical dynamics without capturing non-linear turbulence structures and further support the decoupling between horizontal and vertical dynamics at strong stratification conjecture.

The flux Richardson number Rf is a measure of mixing efficiency. Previously used formulations of Rf contained reversible fluxes and required the majority of turbulent kinetic energy to be dissipated for Rf to converge. A formulation of Rf based only on irreversible fluxes was used instead, which allows Rf of moderately and strongly stratified flows to converge within approximately two eddy turnovers.

Prandtl number effects were observed for strong stratification. The numerical constraints of strongly stratified DNS resulted in diffusive flows. It was argued that the observed Prandtl number effects are a product of low Reynolds numbers because Prandtl number effects are generally considered negligible in large scale energetic flows. Comparison of Rf from DNS and physical experiments reveals a discrepancy which are argued to be a function of the

Prandtl number effects at low Reynolds numbers. When the flow is sufficiently energetic, Rf is a property of the flow, while for diffusive flows Rf becomes a property of the fluid, and hence the Prandtl number effects. RDT models are strongly diffusive due to a complete lack of vertical advective mixing and represent the diffusive limit where Rf scales as Pr^{-1} and is entirely a property of the fluid.

5.3 Conclusions from Chapter 4

The prevalence of overturning regions is dependent on the strength of stratification. Strongly stratified flows are very stable resulting in small overturns with short lifetimes. The classic overturn forms from a breaking gravity wave or other large vortex. The ambient fluid is wrapped inside the vortex against gravity creating instabilities. However, for strongly stratified flows overturns are strongly correlated with horizontal vorticity rather than vertical vorticity. Others have suggested that overturns form from local shear instabilities from sharp local gradients between 'pancake' shaped enstrophy structures. Another potential formation of overturns in strongly stratified flows is when horizontal vorticity rotates a lighter into heavier fluid.

The Thorpe scale is an objective measure of the height of overturns. The traditional Thorpe scale L_T is only a measure of vertical instability within a single profile while the 3D Thorpe scale L_{T3D} incorporates horizontal instability by globally sorting density. It was found that L_T agrees well with L_{T3D} except at strong stratification where L_{T3D} is sensitive to linear waves while L_T is not. Investigations revealed L_T does not scale linearly with the Ozmidov scale L_O and is up to multiple orders larger/smaller for strong/weak stratification. The only region with good agreement between L_T and L_O is where Fr is equal to unity. The findings that L_T is not equal to L_O has important implications for oceanography, where the two length scales are commonly assumed to be equal. Equating L_T and L_O allows for the kinetic energy dissipation rates to be inferred from density profiles. Inferred dissipation rates were compared with actual rates and it was found that dissipation rates are overestimated by up to two orders of magnitude.

5.4 Recommendations for future work

The major weakness in this work (as is the case with many other DNS studies) are the low Reynolds numbers achieved in simulations. The code is a serial code and simulations with $N = 256$ for 10 eddy turnovers takes between four and seven days depending on the Prandtl number and degree of stratification. The maximum Re_λ achieved were 65 for weak stratification and up to 130 for strong stratification. A single $N = 512$ simulation run on a 3.40GHz Intel i7-2600 processor took 17 days for one eddy turnover and required 7 GB of memory. The $N = 256$ and $N = 512$ energy spectrums are plotted in Fig. (5.1). Although Re_λ increased from 67 to 109 there is still no clear inertial subrange meaning the simulation is still diffusive. To simulate strongly stratified energetic flows would require a parallel version of the code to be run on a cluster computer. A very high resolution DNS code developed by Kaneda & Ishihara (2006) is designed so that each core solves a small DNS box with coupled boundaries. Their non-stratified fluid simulations with $N = 4096$ resulted in $Re_\lambda = 1200$ and a clear inertial subrange. It is recommended that further simulations be performed with $N = 1024$ or greater as there were no important improvements from $N = 256$ to 512.

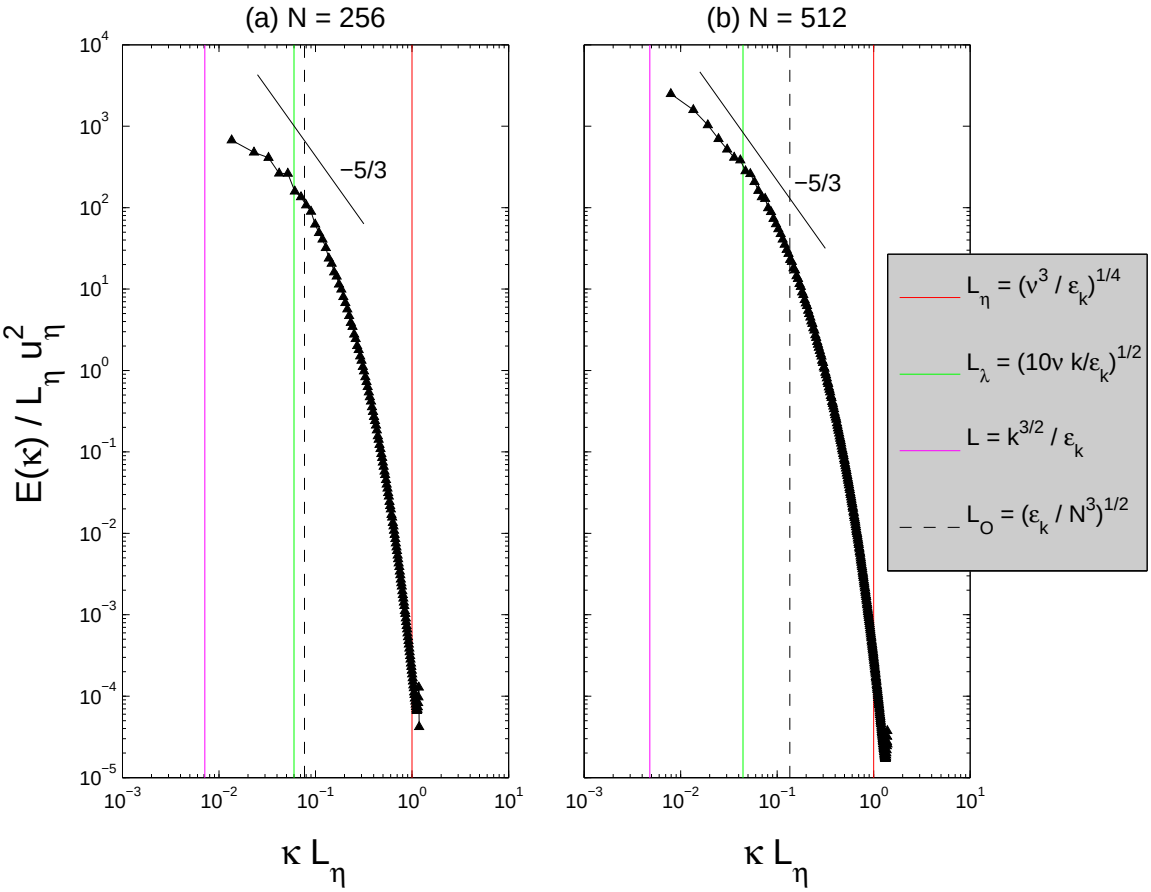

Figure 5.1: Comparison of N=256 and 512 DNS simulation - The runs are for $Ri = 10$ and $Pr = 1$. $Re_\lambda = 67$ for $N = 256$ and $Re_\lambda = 109$ for $N = 512$. There is no clear inertial subrange for $N = 512$ and it is recommended further work be performed with $N = 1024$ or greater.

References

Abarzhi, S., ed. (2011). *Mixing Efficiency in Natural Flows*, Turbulent Mixing and Beyond, Strada Costiera 11, 34014 Trieste, Italy.

Barry, M.E., Ivey, G.N., Winters, K.B. & Imberger, J. (2001). Measurements of diapycnal diffusivities in stratified fluids. *Journal of Fluid Mechanics*, **442**, 267–291.

Batchelor, G.K. (1959). Small-scale variation of convected quantities like temperature in turbulent fluid part 1. general discussion and the case of small conductivity. *Journal of Fluid Mechanics*, **5**, 113–133.

Brethouwer, G. & Lindborg, E. (2009). Numerical study of vertical dispersion by stratified turbulence. *Journal of Fluid Mechanics*, **631**, 149–163.

Britter, R. (1985). Diffusion and decay in stably-stratified turbulent flows. In J.C.R. Hunt, ed., *Turbulence and Diffusion in Stable Environments*, 3–13, Oxford.

Cooley, J.W., Lewis, P.A.W. & Welch, P.D. (1970). The fast fourier transform algorithm: Programming considerations in the calculation of sine, cosine and laplace transforms. *Journal of Sound and Vibration*, **12**, 315–337.

Davidson, P.A. (2004). *Turbulence: An Introduction for Scientists and Engineers*. Oxford University Press.

Diamessis, P.J. & Nomura, K.K. (2004). The structure and dynamics of overturns in stably stratified homogeneous turbulence. *Journal of Fluid Mechanics*, **499**, 197–229.

Dillon, T.M. (1982). Vertical overturns: A comparison of thorpe and ozmidov length scales. *Journal of Geophysical Research*, **87**.

Dougherty, J.P. (1962). The Anisotropy of Turbulence at the Meteor Level. In B. Mæhlum, ed., *Electron Density Profiles in the Ionosphere and Exosphere*, 92.

Durbin, P. & Pettersson Reif, B.A. (2011). *Statistical Theory and Modeling for Turbulent Flows*. Wiley, 2nd edn.

Fernando, H.J.S. (1991). Turbulent mixing in stratified fluids. *Annual Review of Fluid Mechanics*, **23**, 455–493.

Gibson, C.H. (1980). Fossil temperature, salinity, and vorticity turbulence in the ocean. In J.C. Nihoul, ed., *Marine Turbulence Proceedings of The 11th International Liège Colloquium on Ocean Hydrodynamics*, vol. 28 of *Elsevier Oceanography Series*, 221–257, Elsevier.

Gill, A.E. (1982). *Atmosphere-ocean dynamics*. Academic Press, New York :.

Gregg, M.C. (1987). Diapycnal mixing in the thermocline: Review. *Journal of Geophysical Research*, **92**, 5249–5286.

Hanazaki, H. & Hunt, J.C.R. (1996). Linear processes in unsteady stably stratified turbulence. *Journal of Fluid Mechanics*, **318**, 303–337.

Holt, S.E., Koseff, J.R. & Ferziger, J.H. (1992). A numerical study of the evolution and structure of homogeneous stably stratified sheared turbulence. *Journal of Fluid Mechanics*, **237**, 499–539.

Hunt, J.C.R. & Kevlahan, N.K.R. (1993). Rapid distortion theory and the structure of turbulence. In T. Dracos & A. Tsinober, eds., *Proceedings of the Monte Verit´ colloquium on turbulence*.

Iida, O., Tsuzuki, N. & Nagano, Y. (2009). Decaying homogeneous turbulence under strong density stratification at low-prandtl number. *Theoretical and Computational Fluid Dynamics*, **23**, 109–126, 10.1007/s00162-009-0101-1.

Itsweire, E.C. (1984). Measurements of vertical overturns in a stably stratified turbulent flow. *Physics of Fluids*, **27**, 764–766.

Itsweire, E.C., Helland, K.N. & Van Atta, C.W. (1986). The evolution of grid-generated turbulence in a stably stratified fluid. *Journal of Fluid Mechanics*, **162**, 299–338.

Itsweire, E.C., Koseff, J.R., Briggs, D.A. & Ferziger, J.H. (1993). Turbulence in stratified shear flows: Implications for interpreting shear-induced mixing in the ocean. *Journal of Physical Oceanography*, **23**, 1508–1522.

Ivey, G.N. & Imberger, J. (1990). On the nature of turbulence in a stratified fluid. part i: The energetics of mixing. *Journal of Physical Oceanography*, **21**, 650–659.

Ivey, G.N., Koseff, J.R., Briggs, D.A. & Ferziger, J.H. (1992). Mixing in a stratied shear ow: energetics and sampling. In *Annual Research Briefs*, Center for turbulence research, 334–341, Center for turbulence research.

Ivey, G.N., Winters, K.B. & Koseff, J.R. (2008). Density stratification, turbulence, but how much mixing? *Annual Review of Fluid Mechanics*, **40**, 169–184.

Kaneda, Y. & Ishida, T. (2000). Suppression of vertical diffusion in strongly stratified turbulence. *Journal of Fluid Mechanics*, **402**, 311–327.

Kaneda, Y. & Ishihara, T. (2006). High-resolution direct numerical simulation of turbulence. *Journal of Turbulence*, **7**, 777–781.

Kimura, Y. & Herring, J.R. (1995). Stratified turbulence: Structural issues, and turbulent diffusion. In M. Meneguzzi, A. Pouquet & P.L. Sulem, eds., *Small-Scale Structures in Three-Dimensional Hydrodynamic and Magnetohydrodynamic Turbulence*, vol. 462 of *Lecture Notes in Physics*, 195–203, Springer Berlin / Heidelberg, 10.1007/BFb0102416.

Kimura, Y. & Herring, J.R. (2002). Structural and stastical aspects of stratified turbulece. *APS Meeting Abstracts*, F1+.

Kolmogorov, A.N. (1962). A refinement of previous hypotheses concerning the local structure of turbulence in a viscous incompressible fluid at high reynolds number. *Journal of Fluid Mechanics*, **13**, 82–85.

Lindborg, E. (2006). The energy cascade in a strongly stratified fluid. *Journal of Fluid Mechanics*, **550**, 207–242.

Majda, A.J. & Grote, M.J. (1997). Model dynamics and vertical collapse in decaying strongly stratified flows. *Physics of Fluids*, **9**, 2932–2940.

Mansour, N.N., Kim, J. & Moin, P. (1988). Reynolds-stress and dissipation-rate budgets in a turbulent channel flow. *Journal of Fluid Mechanics*, **194**, 15–44.

Mellor, G.L. & Yamada, T. (1982). Development of a turbulence closure model for geophysical fluid problems. *Rev. Geophys. Space Phys.*, **20**, 851–875.

Metais, O. & Herring, J.R. (1989). Numerical simulations of freely evolving turbulence in stably stratified fluids. *Journal of Fluid Mechanics*, **202**, 117–148.

Moin, P. (2010). *Fundamentals of Engineering Numerical Analysis*. Cambridge University Press.

Munk, W. & Wunsch, C. (1998). Abyssal recipes ii: energetics of tidal and wind mixing. *Deep Sea Research Part I: Oceanographic Research Papers*, **45**, 1977–2010.

Munson, B.R., Young, D.F., Okiishi, T.H. & Huebsch, W. (2008). *Fundamentals of Fluid Mechanics*. Wiley.

Nakanish, M. (2001). Improvement of the mellor–yamada turbulence closure model based on large-eddy simulation data. *Boundary-Layer Meteorology*, **99**, 349–378, 10.1023/A:1018915827400.

Oakey, N.S. (1982). Determination of the rate of dissipation of turbulent energy from simultaneous temperature and velocity shear microstructure measurements. *Journal of Physical Oceanography*, **12**, 256–271.

Oduyemi, K. (1993). Mixing efficiency of a stably stratified fluid. *Boundary-Layer Meteorology*, **62**, 107–115, 10.1007/BF00705548.

Orszag, S. & Patterson, G. (1972). Numerical simulation of turbulence. In M. Rosenblatt & C. Van Atta, eds., *Statistical Models and Turbulence*, vol. 12 of *Lecture Notes in Physics*, 127–147, Springer Berlin / Heidelberg.

Osborn, T.R. (1980). Estimates of the local rate of vertical diffusion from dissipation measurements. *J. Phys. Oceanogr.*, **10**, 83–89.

Ouellette, N.T. (2012). Turbulence in two dimensions. *Physics Today*, **65**, 68–69.

Ozmidov, R.V. (1965). On the turbulent exchange in a stably stratified ocean. *Ivs. Acad. Sci. USSR, Atmos. Oceanic Phys.*, **1**, 853–860.

Pardyjak, E.R., Monti, P. & Fernando, H.J.S. (2002). Flux richardson number measurements in stable atmospheric shear flows. *Journal of Fluid Mechanics*, **459**, 307–316.

Park, Y.G., Whitehead, J.A. & Gnanadeskian, A. (1994). Turbulent mixing in stratified fluids: layer formation and energetics. *Journal of Fluid Mechanics*, **279**, 279–311.

Peltier, W.R. & Caulfield, C.P. (2003). Mixing efficiency in stratified shear flows. *Annual Review of Fluid Mechanics*, **35**, 135–167.

Pope, S.B. (2000). *Turbulent flows*. Cambridge University Press.

Praud, O., Fincham, A.M. & Sommeria, J. (2005). Decaying grid turbulence in a strongly stratified fluid. *Journal of Fluid Mechanics*, **522**, 1–33.

Rehmann, C.R. (2004). Scaling for the mixing efficiency of stratified grid turbulence. *Journal of Hydraulic Research*, **42**, 35–42.

Rehmann, C.R. & Koseff, J.R. (2004). Mean potential energy change in stratified grid turbulence. *Dynamics of Atmospheres and Oceans*, **37**, 271–294.

Riley, J.J. & deBruynKops deBruynKops, S.M. (2003). Dynamics of turbulence strongly influenced by buoyancy. *Physics of Fluids*, **15**, 2047–2059.

Riley, J.J., Metcalfe, R.W. & Weissman, M.A. (1981). Direct numerical simulations of homogeneous turbulence in density-stratified fluids. *AIP Conference Proceedings*, **76**, 79–112.

Roberts, C. (2012). *The Ocean of Life, The Fate of Man and the Sea*. Viking.

Rogallo, R.S. & Moin, P. (1984). Numerical simulation of turbulent flows. *Annual Review of Fluid Mechanics*, **16**, 99–137.

Rottman, J.W. & Britter, R. (1986). The mixing efficiency and decay of grid-generated turbulence in stably stratified fuids. 9th Australasian Fluid Mechanics Conference.

Rouse, H. & Dodu, J. (1955). Diffusion turbulente à travers une discontinuité de densité. *La Houille Blanche*, 522–532.

Shih, L.H., Koseff, J.R., Ivey, G.N. & Ferziger, J.H. (2005). Parameterization of turbulent fluxes and scales using homogeneous sheared stably stratified turbulence simulations. *Journal of Fluid Mechanics*, **525**, 193–214.

Smyth, W.D. & Moum, J.N. (2000). Length scales of turbulence in stably stratified mixing layers. *Physics of Fluids*, **12**, 1327–1342.

Smyth, W.D., Moum, J.N. & Caldwell, D.R. (2001). The Efficiency of Mixing in Turbulent Patches: Inferences from Direct Simulations and Microstructure Observations. *Journal of Physical Oceanography*, **31**, 1969–1992.

Stillinger, D.C., Helland, K.N. & Van Atta, C.W. (1983). Experiments on the transition of homogeneous turbulence to internal waves in a stratified fluid. *Journal of Fluid Mechanics*, **131**, 91–122.

Strang, E.J. & Fernando, H.J.S. (2001). Entrainment and mixing in stratified shear flows. *Journal of Fluid Mechanics*, **428**, 349–386.

Stretch, D.D. & Venayagamoorthy, S.K. (2010). Diapycnal diffusivities in homogeneous stratified turbulence. *Geophys. Res. Lett.*, **37**, L02602.

Stretch, D.D., Rottman, J.W., Venayagamoorthy, S.K., Nomura, K.K. & Rehmann, C.R. (2010). Mixing efficiency in decaying stably stratified turbulence. *Dynamics of Atmospheres and Oceans*, **49**, 25–36.

Taylor, G.I. (1935). Statistical theory of turbulence: Parts i-iii. *Proceedings of the Royal Society of London*, **A 151**, 421–464.

Tennekes, H. & Lumley, J.L. (1974). *A first course in turbulence*. MIT Press.

Thorpe, S.A. (1977). Turbulence and mixing in a scottish loch. *Philosophical Transactions of the Royal Society of London. Series A, Mathematical and Physical Sciences*, **286**, pp. 125–181.

Thorpe, S.A. (2005). *The Turbulent Ocean*. Cambridge University Press.

Townsend, A.A. (1980). *The Structure of Turbulent Shear Flow*. Cambridge University Press, 2nd edn.

Tseng, Y. & Ferziger, J.H. (2001). Mixing and available potential energy in stratified flows. *Physics of Fluids*, **13**, 1281–1293.

Turner, J.S. (1973). *Buoyancy effects in fluids*. University Press, Cambridge [England] :.

Venayagamoorthy, S.K. (2002). *Turbulent Mixing and Dispersion in Environmental Flows*. Master's thesis, University of Natal.

Venayagamoorthy, S.K. & Stretch, D.D. (2006). Lagrangian mixing in decaying stably stratified turbulence. *Journal of Fluid Mechanics*, **564**, 197–226.

Venayagamoorthy, S.K. & Stretch, D.D. (2010). On the turbulent prandtl number in homogeneous stably stratified turbulence. *Journal of Fluid Mechanics*, **644**, 359–369.

Venayagamoorthy, S.K., Ku, H., Fringer, O.B., Chiu, A., Naylor, R. & Koseff, J.R. (2011). Numerical modeling of aquaculture dissolved waste transport in a coastal embayment. *Environmental Fluid Mechanics*, **11**, 329–352.

Vincent, A. & Meneguzzi, M. (1991). The spatial structure and statistical properties of homogeneous turbulence. *Journal of Fluid Mechanics*, **225**, 1–20.

Winters, K.B. & D'Asaro, E.A. (1996). Diascalar flux and the rate of fluid mixing. *Journal of Fluid Mechanics*, **317**, 179–193.

Wunsch, C. & Ferrari, R. (2004). Vertical mixing, energy, and the general circulation of the oceans. *Annual Review of Fluid Mechanics*, **36**, 281–314.

Yeung, P.K. & Pope, S.B. (1989). Lagrangian statistics from direct numerical simulations of isotropic turbulence. *Journal of Fluid Mechanics*, **207**, 531–586.

Appendix A

Description of simulations and models

A.1 Summary of runs

DNS were used to explore the dynamics of turbulent flows for a range of Ri, Pr, and Re_0. The main DNS parametric study performed contains 32 runs with varying Ri and Pr. The main DNS study is summarized in Table (A.1). To investigate Reynolds number effects, a DNS parametric study was performed for 12 runs with $Ri = 1000$ and with varying Re_0 and Pr. The Reynolds number DNS study is summarized in Table (A.2).

RDT was used to further investigate Prandtl number and Reynolds number effects. All RDT runs are for $Ri = 1000$ to ensure the flow is adequately anisotropic and "distorted". For the Reynolds number RDT study, summarized in Table (A.3), 5 RDT runs were performed for $Pr = 1$ with varying Re_0. The inviscid and non-diffusive limits was explored at very high Reynolds and Peclet numbers with 8 runs summarized in Table (A.4). Prandtl number effects were explored with 7 runs in the Prandtl number RDT study, summarized in Table (A.5).

Stability requirements for isotropic turbulence is generally defined by the Courant number (Eq. 2.66), which is a function of the turbulent kinetic energy. For the strongly stable runs, a smaller timestep was required to account for reduced fluctuations in the vertical velocity field.

To calculate accurate Rf using Eq. (2.31) the majority of k should be dissipated. Venayagamoorthy (2002) ran all simulations for 10 T_0 so that 95% of k was dissipated. In this work, less than 95% of k was dissipated for strongly stratified simulations. The irreversible formulation of Rf (Eq. 2.32) produced convergence within approximately $1T_0$ making durations of simulations appropriate.

The Taylor Reynolds number Re_λ and turbulent Reynolds number Re_L are calculated

at the decay point, as discussed in Sec. (3.3.3). The buoyancy Reynolds number R_b are the peak values. The normalized wavenumbers $\kappa_{max}L_\eta$ and $\kappa_{max}L_B$ are the minimum values for each simulation.

Table A.1: Main DNS study - Parameter values and results of runs analyzed in main DNS study.

Run #	Parameters						Results							
	Ri	Pr	N	ν	Δt	t_{final}	k_{final}/k_0	$\kappa_{max}L_\eta$	$\kappa_{max}L_B$	Rf	Re_0	Re_λ	Re_L	R_b
DNS256_Ri0001_Pr01	0.00987	0.1	256	0.0016	0.001	10	0.986	1.044	3.304	0.006940	625	64.56	605.7	51934
DNS256_Ri0001_Pr05	0.00987	0.5	256	0.0016	0.001	10	0.986	1.044	1.477	0.007230	625	64.56	605.7	51916
DNS256_Ri0001_Pr1	0.00987	1	256	0.0016	0.001	10	0.986	1.044	1.044	0.007030	625	64.56	605.7	51913
DNS256_Ri0001_Pr2	0.00987	2	256	0.0016	0.0005	10	0.986	1.045	0.7391	0.006701	625	64.71	608.9	51839
DNS256_Ri001_Pr01	0.100	0.1	256	0.0016	0.001	10	0.991	1.050	3.321	0.04648	625	64.19	598.9	5019
DNS256_Ri001_Pr05	0.100	0.5	256	0.0016	0.001	10	0.990	1.051	1.486	0.04977	625	64.19	599.1	5003
DNS256_Ri001_Pr2	0.100	2	256	0.0016	0.0005	10	0.990	1.051	0.7437	0.04787	625	65.08	615.9	4992
DNS256_Ri001_Pr1	0.100	1	256	0.0016	0.001	10	0.990	1.051	1.051	0.04906	625	64.18	599.3	5000
DNS256_Ri004_Pr01	0.395	0.1	256	0.0016	0.001	10	0.990	1.067	3.376	0.1159	625	64.50	605.7	1190
DNS256_Ri004_Pr05	0.395	0.5	256	0.0016	0.001	10	0.989	1.070	1.514	0.1238	625	64.58	606.7	1177
DNS256_Ri004_Pr2	0.395	2	256	0.0016	0.0005	10	0.988	1.071	0.7578	0.1191	625	65.50	624.3	1172
DNS256_Ri004_Pr1	0.395	1	256	0.0016	0.001	10	0.988	1.071	1.071	0.1221	625	64.60	606.9	1175
DNS256_Ri015_Pr01	1.58	0.1	256	0.0016	0.001	10	0.984	1.127	3.564	0.2734	625	65.61	626.0	239.7
DNS256_Ri015_Pr05	1.58	0.5	256	0.0016	0.001	10	0.981	1.133	1.603	0.2711	625	65.72	627.9	233.9
DNS256_Ri015_Pr1	1.58	1	256	0.0016	0.001	10	0.981	1.133	1.133	0.2598	625	65.65	626.9	234.0
DNS256_Ri015_Pr2	1.58	2	256	0.0016	0.0005	10	0.980	1.133	0.8014	0.2479	625	64.98	614.1	234.3
DNS256_Ri010_Pr01	9.97	0.1	256	0.0016	0.001	10	0.958	1.296	4.101	0.5519	625	75.42	823.9	21.66
DNS256_Ri010_Pr05	9.97	0.5	256	0.0016	0.001	10	0.957	1.215	1.719	0.4310	625	70.01	711.0	28.06
DNS256_Ri010_Pr1	9.97	1	256	0.0016	0.001	10	0.956	1.185	1.185	0.3722	625	66.94	650.4	30.98
DNS256_Ri010_Pr2	9.97	2	256	0.0016	0.001	10	0.955	1.163	0.8229	0.3215	625	65.32	619.0	33.39
DNS256_Ri040_Pr01	39.5	0.1	256	0.0016	0.001	10	0.940	1.418	4.486	0.6242	625	112.4	1835	3.820
DNS256_Ri040_Pr05	39.5	0.5	256	0.0016	0.001	10	0.925	1.265	1.789	0.4399	625	74.13	797.5	6.040
DNS256_Ri040_Pr1	39.5	1	256	0.0016	0.001	10	0.922	1.216	1.216	0.3520	625	69.94	709.5	7.074
DNS256_Ri040_Pr2	39.5	2	256	0.0016	0.0005	10	0.920	1.182	0.8363	0.2751	625	66.83	648.0	7.906
DNS256_Ri158_Pr01	158	0.1	256	0.0016	0.0005	10	0.917	1.566	4.954	0.6056	625	117.0	1987	0.6417
DNS256_Ri158_Pr05	158	0.5	256	0.0016	0.0005	10	0.897	1.371	1.939	0.4072	625	103.9	1569	1.092
DNS256_Ri158_Pr1	158	1	256	0.0016	0.0005	10	0.891	1.310	1.310	0.3097	625	97.35	1377	1.311
DNS256_Ri158_Pr2	158	2	256	0.0016	0.0005	10	0.887	1.266	0.8958	0.2225	625	92.13	1233	1.501
DNS256_Ri100_Pr01	987	0.1	256	0.0016	0.0005	10	0.893	1.614	5.105	0.5675	625	131.4	2507	0.09108
DNS256_Ri100_Pr05	987	0.5	256	0.0016	0.0005	10	0.860	1.456	2.060	0.3572	625	127.1	2346	0.1374
DNS256_Ri100_Pr1	987	1	256	0.0016	0.0005	10	0.848	1.400	1.400	0.2548	625	121.0	2126	0.1607
DNS256_Ri100_Pr2	987	2	256	0.0016	0.0005	10	0.839	1.361	0.9623	0.1655	625	115.8	1948	0.1804

Table A.2: Reynolds number DNS study - Parameter values and results of runs analyzed in Reynolds number DNS study.

Run #	Parameters						Results							
	Ri	Pr	N	ν	Δt	t_{final}	k_{final}/k_0	$\kappa_{max}L_\eta$	$\kappa_{max}L_B$	Rf	Re_0	Re_λ	Re_L	R_b
DNS256_Re100_Pr01	987	0.1	256	0.01	0.0005	5	0.928	4.157	13.14	0.5058	100	42.48	262.2	0.08095
DNS256_Re200_Pr01	987	0.1	256	0.005	0.0005	5	0.880	2.940	9.295	0.5440	200	84.95	1048	0.08095
DNS256_Re400_Pr01	987	0.1	256	0.0025	0.0005	5	0.830	2.079	6.573	0.5807	400	169.90	4195	0.08095
DNS256_Ri100_Pr01	987	0.1	256	0.0016	0.0005	10	0.893	1.614	5.105	0.5675	625	131.43	2507	0.09108
DNS256_Re100_Pr05	987	0.5	256	0.01	0.0005	5	0.911	4.157	5.878	0.3435	100	42.48	262.2	0.08095
DNS256_Re200_Pr05	987	0.5	256	0.005	0.0005	5	0.851	2.940	4.157	0.3563	200	84.95	1048	0.08095
DNS256_Re400_Pr05	987	0.5	256	0.0025	0.0005	5	0.792	1.936	2.737	0.3706	400	99.55	1437	0.1076
DNS256_Ri100_Pr05	987	0.5	256	0.0016	0.0005	10	0.860	1.456	2.060	0.3572	625	127.10	2346	0.1374
DNS256_Re100_Pr1	987	1	256	0.01	0.0005	5	0.902	4.157	4.157	0.2492	100	42.48	262.2	0.08095
DNS256_Re200_Pr1	987	1	256	0.005	0.0005	5	0.839	2.894	2.894	0.2557	200	58.42	495.4	0.08615
DNS256_Re400_Pr1	987	1	256	0.0025	0.0005	5	0.779	1.867	1.868	0.2647	400	90.03	1176	0.1242
DNS256_Ri100_Pr1	987	1	256	0.0016	0.0005	10	0.848	1.401	1.400	0.2548	625	121.00	2126	0.1607

Table A.3: Reynolds number RDT study - Parameter values and results of runs analyzed in Reynolds number RDT study.

Run #	Parameters						Results							
	Ri	Pr	N	ν	Δt	t_{final}	k_{final}/k_0	$\kappa_{max}L_\eta$	$\kappa_{max}L_B$	Rf	Re_0	Re_λ	Re_L	R_b
RDT256_Re100_Pr1	987	1	256	0.01	0.0005	20	0.977	4.157	4.157	0.2429	100	42.47	262.21	0.08095
RDT256_Re200_Pr1	987	1	256	0.005	0.0005	20	0.930	2.939	2.939	0.2471	200	84.95	1048	0.08095
RDT256_Re400_Pr1	987	1	256	0.0025	0.0005	20	0.841	2.078	2.078	0.2516	400	169.90	4195	0.08095
RDT256_Ri100_Pr1	987	1	256	0.0016	0.0005	20	0.759	1.662	1.662	0.2541	625	265.47	10242	0.08095
RDT256_Re1000_Pr1	987	1	256	0.001	0.0005	20	0.656	1.314	1.314	0.2563	1000	424.80	26220	0.08095

Table A.4: Inviscid and non-diffusive RDT study - Parameter values and results of runs analyzed in inviscid and non-diffusive RDT study.

Run #	Parameters						Results							
	Ri	Pr	N	ν	Δt	t_{final}	k_{final}/k_0	$\kappa_{max}L_\eta$	$\kappa_{max}L_B$	Rf	Re_0	Re_λ	Re_L	R_b
RDT256_Re100_Pr1000	987	1000	256	0.01	0.0005	20	0.962	4.157	0.1314	0.000477	100	42.47	262.2	0.0809
RDT256_Re200_Pr1000	987	1000	256	0.005	0.0005	5	0.653	2.939	0.0929	0.000402	200	84.95	1048	0.0809
RDT256_Re400_Pr1000	987	1000	256	0.0025	0.0005	5	0.504	2.078	0.0657	0.000375	400	169.9	4195	0.0809
RDT256_Ri100_Pr1000	987	1000	256	0.0016	0.0005	20	0.708	1.662	0.0525	0.000430	625	265.5	10242	0.0809
RDT256_Re1000_Pr1000	987	1000	256	0.001	0.0005	5	0.355	1.314	0.0415	0.000353	1000	424.7	26220	0.0809
RDT256_Re10000_Pr1000	987	1000	256	0.0001	0.0005	5	0.227	0.415	0.0131	0.000336	10000	4247	2.622e06	0.0809
RDT256_Re100000_Pr1000	987	1000	256	1e-05	0.0005	5	0.212	0.131	0.0041	0.000334	1.0e05	42475	2.622e08	0.0809
RDT256_Re1000000_Pr1000	987	1000	256	1e-06	0.0005	5	0.210	0.041	0.0013	0.000333	1.0e06	424758	2.622e10	0.0809

Table A.5: Prandtl number RDT study - Parameter values and results of runs analyzed in Prandtl number RDT study.

Run #	Parameters						Results							
	Ri	Pr	N	ν	Δt	t_{final}	k_{final}/k_0	$\kappa_{max}L_\eta$	$\kappa_{max}L_B$	Rf	Re_0	Re_λ	Re_L	R_b
RDT256_Ri100_Pr01	987	0.1	256	0.0016	0.0005	20	0.826	1.662	5.258	0.51926	625	265.4	10242	0.08095
RDT256_Ri100_Pr05	987	0.5	256	0.0016	0.0005	20	0.782	1.662	2.351	0.35804	625	265.4	10242	0.08095
RDT256_Ri100_Pr1	987	1	256	0.0016	0.0005	20	0.759	1.662	1.662	0.25413	625	265.4	10242	0.08095
RDT256_Ri100_Pr2	987	2	256	0.0016	0.0005	20	0.739	1.662	1.175	0.16015	625	265.4	10242	0.08095
RDT256_Ri100_Pr10	987	10	256	0.0016	0.0005	20	0.716	1.662	0.5258	0.04034	625	265.4	10242	0.08095
RDT256_Ri100_Pr100	987	100	256	0.0016	0.0005	20	0.709	1.662	0.1662	0.004282	625	265.4	10242	0.08095
RDT256_Ri100_Pr1000	987	1000	256	0.0016	0.0005	20	0.708	1.662	0.05258	0.0004309	625	265.4	10242	0.08095

A.2 Description of DNS code

The DNS code was written by Riley *et al.* (1981) in the FORTRAN 77 programming language. The implemented pseudo-spectral numerical methods are very accurate but can only be run on a single processor. The serial code is conducive to parametric studies with simulations running simultaneously on individual cores. A parallel code is required for future work as the domain size is restricted to the speed of an individual core. Rewriting the pseudo-spectral numerical methods for parallel processing was outside the scope of this work.

All components of the code are summarized in Table (A.6). The file `MAIN` is the program file from which all subroutines are called. To better explain the code, a flowchart of the DNS code is shown in Fig. (A.1).

The format of output statistics in the code was modified. Outputs were previously in text format, which required subroutines to counted spaces to collect output data. The new output format is a MATLAB script file, which is easily run in MATLAB in a function subroutine to extract desired data.

Table A.6: Subroutines and files of DNS code - All files required by code including subroutines and main files.

Filename	Type	Description
`CROSS`	Subroutine	Computes cross product of velocity and vorticity
`DENS`	Subroutine	Generates a random, complex number
`FIVE`	Subroutine	Component of `THRDETR`: Inverse DFT
`FOUR`	Subroutine	Component of `THRDETR`: Forward DFT
`FOUR2`	Subroutine	Component of `THRDETR`: FFT
`IMAGE`	Subroutine	Output flow field parameters
`INIT`	Subfile	Initialization file to declare constants
`MAIN`	Program	Main file to run code
`NORM`	Subroutine	Generates random numbers to be used by DENS and VECT
`PACK`	Subroutine	Computes vorticity and prepares for Fourier transform
`SPECTRA`	Subroutine	Computes energy spectrum to initialize velocity field
`START`	Subroutine	Initializes velocity field
`STAT`	Subroutine	Compute energy spectrums and other statistics
`STEP`	Subroutine	Advance timestep with modified leapfrog and Euler
`THRDETR`	Subroutine	Main subroutine to perform forward and inverse DFT
`TRNSFR`	Subroutine	Compute nonlinear transfer functions
`VECT`	Subroutine	Generates a random, complex vector

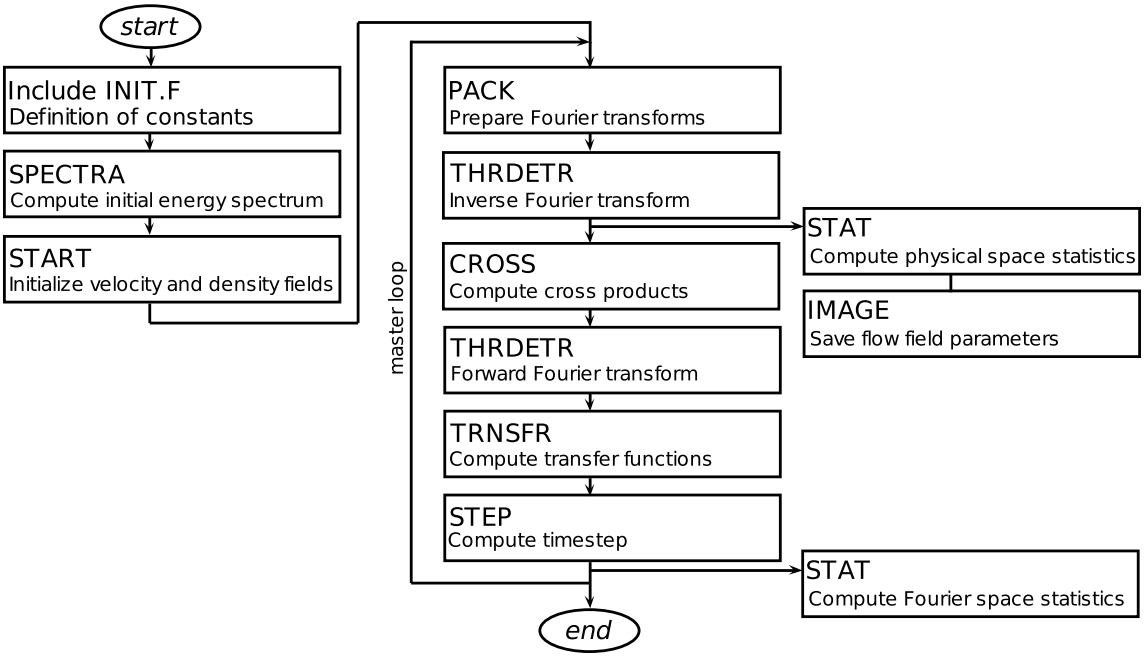

Figure A.1: Flowchart of DNS code - Subroutines are called from the main program file `MAIN`. Statistics are computed from Fourier and physical space with the `STAT` subroutine and parameter fields are output with the `IMAGE` subroutine.

A.3 Description of RDT code

RDT was initially implemented into the code by Stretch *et al.* (2010). Efficiency was improved by removing unnecessary Fourier transforms. As non-linear terms are neglected in RDT, Fourier transforms are only performed to collect physical space statistics and the `CROSS` subroutine is not used. No computations are performed in physical space which need to be transformed back into Fourier space so subroutine `THREDTR` to perform forward Fourier transforms is also not used. The inverse Fourier transforms are only performed when physical space statistics are collected. To adjust for the non-linear terms not calculated, the `TRNSFT` subroutine was also modified. A flowchart of the RDT code is shown in Fig. (A.2).

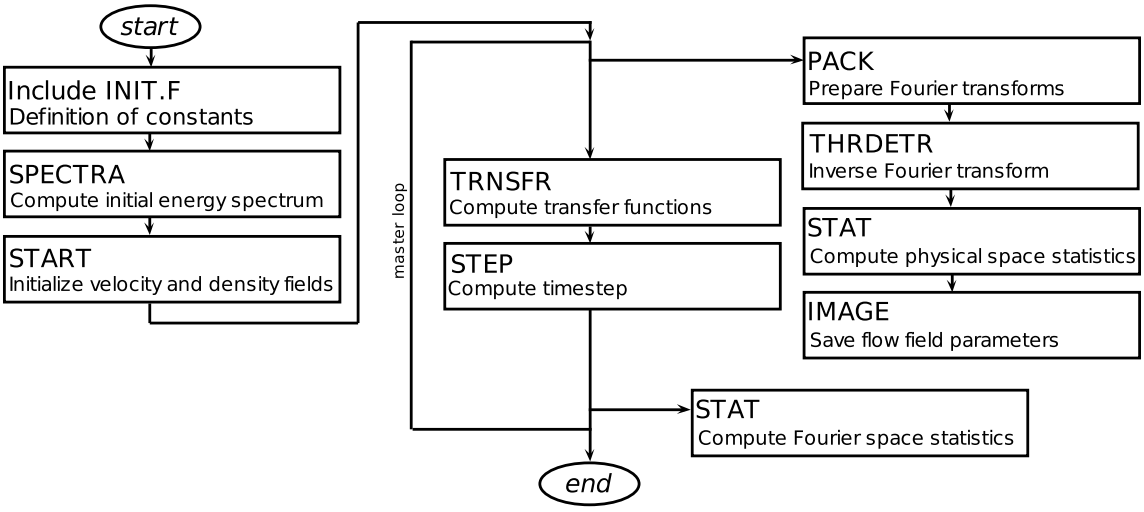

Figure A.2: Flowchart of RDT code - The non-linear computations are performed in physical space by `CROSS` subroutine. Fourier transforms are only performed to collect physical space statistics and `CROSS` is not used. No computations are performed in physical space which need to be transformed back into Fourier space so subroutine `THREDTR` to perform forward Fourier transforms is also not used.

Appendix B

Thorpe scale post-processing

B.1 Ensemble-average Thorpe scale

The background density profile is decoupled from the flow allowing the density field to be calculated directly from the density flux ρ' as

$$\rho_{ijk} = \overline{\rho}_k + \rho_{ijk}. \tag{B.1}$$

The background density $\overline{\rho}$ is normalized such that $\partial\overline{\rho}/\partial z = 1$. The domain height $\mathcal{L}$ is equal to $2\pi/\kappa_0$ with $\kappa_0 = 2$ such that $0 \leq z \leq \pi$ and $0 \leq \overline{\rho} \leq \pi$.

Thorpe displacements are the distance a particle must travel back to a stable position along the gravitationally sorted density profile $\partial\langle\rho\rangle/\partial z$. The sorted density profile is easily determined by sorting a vertical profile monotonically. Thorpe displacements d' are

$$d'_{ijk} = z_{\rho_{ijk}} - z_{\langle\rho\rangle=\rho_{ijk}}, \tag{B.2}$$

which are calculated by tracking the presorted positions.

The Thorpe scale of an individual profile $L_{T,ij}$ is the root-mean-square of non-zero d',

$$L_{T,ij} = \left[\frac{1}{M}\sum_{k=1}^{N} d'^2_{ijk}\right]^{1/2}_{d_{ijk}\neq 0}, \tag{B.3}$$

where M is the number of non-zero d' located in the profile (Thorpe, 2005). The ensemble-average Thorpe scale is commonly used to reduce variance (Itsweire *et al.*, 1993). The MATLAB code used to calculate L_T is located in Listing (B.1).

B.2 3D Thorpe scale

If a three-dimensional sorting technique is used, the resulting 3D Thorpe scale L_{T3D} is a measure of general scalar fluctuations in addition to overturning. To calculate L_{T3D}, the entire $N \times N \times N$ density field in the domain is monotonically sorted into the N^3 long 3D sorted density profile $\partial\langle\rho\rangle_{3D}/\partial z$. The $N \times N \times N$ density field is recreated from $\partial\langle\rho\rangle_{3D}/\partial z$ with the first N^2 values from $\langle\rho\rangle_{3D}$ located in the first row, the second N^2 values in the second row, etcetera. The Thorpe displacements d' are the *vertical* distance a particle must travel back to a gravitationally stable position in the domain. The 3D Thorpe scale is then calculated as the root-mean-square of all displacements (Itsweire *et al.*, 1993),

$$L_{T3D} = \left[\frac{1}{N^3} \sum_{i=1}^{N} \sum_{j=1}^{N} \sum_{k=1}^{N} d'^2_{ijk} \right]^{1/2} . \tag{B.4}$$

The code to calculate L_{T3D} is located in Listing (B.2). To sort the density field, an N^3 array `XYZ` was created with all density values using three loops for k, i, and j (performed in that order). The MATLAB function `sort` was used to monotonically sort `XYZ` into array `XYZsort` and record original position in array `idx`. The position $z_{\rho_{ijk}}$ and $z_{\langle\rho\rangle=\rho_{ijk}}$ (Eq. B.2) were calculated from `XYZsort` and `idx` for a loop count c (where c goes from 1 to N^3) as

$$z_{\rho_{ijk}} = \left(\frac{2\pi}{N\kappa_0} \right) \texttt{ceil}\left(\texttt{idx}(c)/N^2 \right), \tag{B.5}$$

$$z_{\langle\rho\rangle=\rho_{ijk}} = \left(\frac{2\pi}{N\kappa_0} \right) \texttt{ceil}\left(c/N^2 \right), \tag{B.6}$$

where `ceil` is a MATLAB function which rounds up to the next integer. The Thorpe displacement are therefore

$$d'(c) = \left(\frac{2\pi}{N\kappa_0} \right) \left[\texttt{ceil}\left(\texttt{idx}(c)/N^2 \right) - \texttt{ceil}\left(c/N^2 \right) \right]. \tag{B.7}$$

Listing B.1: `load_LT2D` - MATLAB code to calculate ensemble-average Thorpe scale.

```
%%%%%%%%%%%%%%%%%%%%%%%%%%%%%%%%%%%%%%%%%%%%%%%%%%%%%%%%%%%%%%%%%%%%%%%%%%%%
% load_LT2D.m :: This code calculates the Thorpe scales by individually
% sorting each vertical profile in box.
%%%%%%%%%%%%%%%%%%%%%%%%%%%%%%%%%%%%%%%%%%%%%%%%%%%%%%%%%%%%%%%%%%%%%%%%%%%%
%% Specify Variables ------------------------------------------------------
Ri = { '0001' '001' '004' '015' '010' '040' '158' '100'};% Ri: Richardson no. code
Pr = '1';                                       % Pr: Prandtl number code
Type = 'DNS';                                   % Type: DNS or RDT
N = 256;                                        % N: DNS box size
directory = '../../data/IMAGES/';               % directory to harvest from
AKMIN = 2;                                      % normalizing factor from code
% ------------------------------------------------------------------------
%% Begin Ri loop
for r = 1:length(Ri)                            % r: index of Ri
%% Begin t loop
c = 1;
for t = 1:0.25:5                                % t: eddy turnover time
%% Housekeeping
    % determine IMAGE time code (note: Ri = 158 & 1000 have smaller \delta t)
    if length(Ri{r}) ~= 4
        if Ri{r} == '158' | Ri{r} == '100',
            tI = num2str(2*t*1000);             % tI: IMAGE time code
            if t == 5, tI = '9999'; end         % special numbering case
        else tI = num2str(t*1000); end
    else tI = num2str(t*1000); end
    % define normalized arrays and preallocate large matrices for speed
    z = zeros(N,N,N);                           % z: normalized z array
    rho = zeros(N,N,N);                         % rho: background field
    rhoTotal = zeros(N,N,N);                    % rhoTotal: density field
    b = zeros(N,N,N);                           % b: density fluctuations
    d = zeros(N,N,N);                           % d: Thorpe dispalcements
    bg = zeros(N,N,N);                          % bg: sorted profile
    LT = zeros(N,N);                            % LT: Thorpe scales
    idx = zeros(N,N,N);                         % sort indices
%% Load buoyancy flux data from IMAGE (requires function PIC_READ)
filename = ['DNS' num2str(N) '_Ri' Ri{r} '_Pr' Pr '/PIC' num2str(N) '_4_' tI];
b = PIC_READ(directory,filename,N);             % b: buoyancy flux
%% Calculate \rho
for k = 1:N
    rho(:,:,k) = (N-k) / (N-1) * (2*pi/AKMIN);
    z(:,:,k) = (k-1)*(2*pi/AKMIN) / (N-1);
end
rhoTotal = rho + b;            % rho: density
%% Sort \rho by doing one z profile at a time
for i = 1:N, for j = 1:N,
    [bg(i,j,:),idx(i,j,:)] = sort(rhoTotal(i,j,:),'descend'); % bg: sorted rho
end, end,
%% Calculate Thorpe displacements
for i = 1:N, for j = 1:N, for k = 1:N,
     d(i,j,k) = z(i,j,idx(i,j,k)) - z(i,j,k);    % d: Thorpe displacement
end, end, end,
%% Calculate Thorpe scales
for i = 1:N, for j = 1:N,
LT(i,j) = ( nnz(d(i,j,:))^-1 * sum( d(i,j,:).^2 ) )^0.5; % LT: Thorpe scale
end, end,
eval(['LT2D_' Ri{r} '(c) = nanmean( nanmean( LT ) )']); % LT2D: ensemble-avg
eval(['stdev_' Ri{r} '(c) = nanstd( nanstd( LT ) )']);  % standard deviation
c = c+1;
end % end t loop
end % end Ri loop
```

Listing B.2: `load_LT3D` - MATLAB code to calculate 3D Thorpe scale.

```
%%%%%%%%%%%%%%%%%%%%%%%%%%%%%%%%%%%%%%%%%%%%%%%%%%%%%%%%%%%%%%%%%%%%%%%%%%%%
% load_LT3D.m :: This code calculates the 3D Thorpe scale by sorting entire
% box instead of a single profile required for the traditional Thorpe scale
%%%%%%%%%%%%%%%%%%%%%%%%%%%%%%%%%%%%%%%%%%%%%%%%%%%%%%%%%%%%%%%%%%%%%%%%%%%%
%% Specify Variables ------------------------------------------------------
Ri = {'0001' '001' '004' '015' '010' '040' '158' '100'};% Ri: Richardson no. code
Pr = '1';                                          % Pr: Prandtl number code
Type = 'DNS';                                      % Type: DNS or RDT
N = 256;                                           % N: DNS box size
directory = '../../data/IMAGES/';                  % directory to harvest from
AKMIN = 2;                                         % normalizing factpr from code
% ------------------------------------------------------------------------
%% Begin Ri loop
for r = 1:length(Ri)                               % r: index of Ri
%% Begin t loop
q = 1;
for t = 1:0.25:5                                   % t: eddy turnover time
%% Housekeeping
    % determine IMAGE time code (note: Ri = 158 & 1000 have smaller \delta t)
    if length(Ri{r}) ~= 4
        if Ri{r} == '158' | Ri{r} == '100',
            tI = num2str(2*t*1000);                % tI: IMAGE time code
            if t == 5, tI = '9999'; end            % special numbering case
        else tI = num2str(t*1000); end
    else tI = num2str(t*1000); end
    % preallocate all large arrays for speed
    rho = zeros(N,N,N);                            % rho: background density
    rhoTotal = zeros(N,N,N);                       % rhoTotal: total density
    b = zeros(N,N,N);                              % b: buoyancy flux
    XYZ = zeros(1,N^3);                            % XYZ: N^3 array
    XYZsort = zeros(1,N^3);                        % XYZsort: sorted N^3 array
    idx = zeros(1,N^3);                            % idx: indices of XYZsort
    d = zeros(1,N^3);                              % d: thorpe displacements
%% Load buoyancy flux data from IMAGE (requires function PIC_READ)
filename = ['DNS' num2str(N) '_Ri' Ri{r} '_Pr' Pr '/PIC' num2str(N) '_4_' tI];
b = PIC_READ(directory,filename,N);                % b: buoyancy flux
%% Calculate \rho
for k = 1:N
    rho(:,:,k) = (N-k) / (N-1) * (2*pi/AKMIN);     % rho: background density
end
rhoTotal = rho + b;                                % rhoTotal: total density
%% Dump into N^3 array (XYZ)
c = 1;
for k = 1:N,
    for i = 1:N, for j = 1:N
    XYZ(c) = rhoTotal(i,j,k);                      % XYZ: N^3 array
    c = c+1;
    end, end
end
%% Sort N^3 array (XYZ) with highest \rho at top (i.e. k = 1)
[XYZsort, idx] = sort(XYZ,'descend');              % XYZsort: sorted N^3 array
                                                   % idx: indices of XYZsort
%% Calculate Thorpe displacements
for c = 1:N^3,
    d(c) = (2*pi)/(N*AKMIN) * ( ceil( idx(c)/N^2 ) - ceil( c/N^2 ) ) ; % d: thorpe disp.
end
%% Calculate 3D Thorpe scale
eval(['LT3D_' Ri{r} '(q) = mean2( d.^2 )^0.5 ']);% LT3D: 3D LT
q = q+1;
end % end t loop
end % end Ri loop
```

B.3 Tabulated results

Table B.1: Thorpe scale results - L_T and L_{T3D} for all runs analyzed.

Run #	Time	Ensmeble-average Thorpe scale		3D Thorpe scale	Ozmidov scale	Buoyancy scale	Turbulence scale	Ellison scale
	t	L_T	σ	L_{T3D}	L_O	L_b	L	L_E
	1	0.92049	0.05975	0.9762	28.429	6.4551	1.2808	0.56921
	2	0.73785	0.03440	0.9099	19.677	2.607	0.6072	0.55227
DNS256_Ri0001_Pr1	3	0.79368	0.04413	0.9979	10.350	1.3156	0.6789	0.62849
	4	0.84012	0.05161	1.0826	6.7430	0.85699	0.7522	0.71274
	5	0.96318	0.05992	1.1578	4.8881	0.59327	0.8040	0.79310
	1	0.91502	0.05928	0.9704	4.9545	1.9749	1.2807	0.56480
	2	0.72611	0.03494	0.8905	3.4078	0.75835	0.5956	0.53759
DNS256_Ri001_Pr1	3	0.75208	0.04158	0.9495	1.7652	0.32541	0.6134	0.58395
	4	0.7488	0.04265	0.9863	1.0994	0.1734	0.6325	0.62370
	5	0.7955	0.04203	1.0014	0.76616	0.09250	0.6042	0.63875
	1	0.89689	0.05803	0.9516	1.7125	0.91212	1.2729	0.55045
	2	0.68425	0.03457	0.8335	1.1580	0.30208	0.5673	0.49193
DNS256_Ri004_Pr1	3	0.63828	0.04885	0.7857	0.58437	0.09979	0.5343	0.45717
	4	0.59774	0.03654	0.6983	0.35386	0.05255	0.5810	0.39115
	5	0.52922	0.03150	0.5637	0.24758	0.04496	0.7265	0.29816
	1	0.82371	0.05507	0.8742	0.54444	0.33462	1.2416	0.49295
	2	0.51242	0.02702	0.5789	0.36445	0.11945	0.6265	0.32249
DNS256_Ri015_Pr1	3	0.37683	0.02596	0.4169	0.19559	0.05607	0.6900	0.22672
	4	0.32745	0.02658	0.3784	0.12202	0.02546	0.7543	0.20248
	5	0.28503	0.02033	0.3043	0.08867	0.02135	0.9161	0.16279
	1	0.41242	0.01880	0.4211	0.12440	0.13977	1.3414	0.21863
	2	0.26776	0.01294	0.2889	0.08168	0.04804	0.8337	0.14765
DNS256_Ri010_Pr1	3	0.19912	0.01352	0.2069	0.04577	0.02489	1.2261	0.10536
	4	0.15043	0.00871	0.1777	0.03125	0.01536	1.6317	0.08988
	5	0.13825	0.01241	0.1522	0.02419	0.01198	2.0613	0.07739
	1	0.23283	0.01318	0.2455	0.04240	0.04967	1.3696	0.12490
	2	0.15552	0.01061	0.1659	0.02747	0.02279	1.3914	0.08354
DNS256_Ri040_Pr1	3	0.11882	0.00656	0.1354	0.01786	0.01248	1.7929	0.06862
	4	0.10053	0.01699	0.1042	0.01323	0.00939	2.4574	0.05282
	5	0.08716	0.00552	0.0910	0.01072	0.00784	2.9026	0.04538
	1	0.11295	0.00674	0.1137	0.01282	0.02096	2.4554	0.05700
	2	0.07670	0.00415	0.0902	0.01005	0.00958	2.1008	0.04527
DNS256_Ri158_Pr1	3	0.05946	0.00628	0.0773	0.00728	0.00642	2.4809	0.03807
	4	0.04917	0.00567	0.0678	0.00584	0.00414	2.6945	0.03346
	5	0	0	0.0495	0.00502	0.00512	3.1391	0.02426
	1	0.03589	0.00445	0.0451	0.00284	0.01041	3.7188	0.02215
	2	0	0	0.0345	0.00250	0.00627	3.3515	0.01670
DNS256_Ri100_Pr1	3	0	0	0.0356	0.00200	0.00370	3.2523	0.01732
	4	0	0	0.0293	0.00172	0.00332	3.4654	0.01410
	5	0	0	0.0295	0.00146	0.00278	3.3747	0.01431

Glossary

δ_{ij}	Kronecker delta function
Δt	Time step
Δx	Grid size
ϵ_ρ	Density dissipation rate (Eq. 2.21)
ϵ_k	Turbulent kinetic energy dissipation rate (Eq. 2.13)
ϵ_p	Turbulent potential energy dissipation rate (Eq. 2.24)
ϵ_T	Inferred dissipation from L_T (Eq. 4.1)
ϵ_T	Total energy dissipation rate
Γ	Integral mixing efficiency (Eq. 2.27)
κ	Molecular diffusivity
κ	Wavenumber
κ_0	Lowest wavenumber
κ_{eff}	Effective diffusivity
κ_{max}	Highest wavenumber
$\langle\rho\rangle$	Gravitationally stable density profile
$\langle\rho\rangle_{3D}$	3D gravitationally stable sorted density profile
$\mathcal{L}$	Length of domain
$\mathcal{P}$	Turbulent kinetic energy production rate (Eq. 2.13)
$\mathcal{T}$	Turbulent kinetic energy transport rate (Eq. 2.13)
$\mid \omega^2 \mid$	Enstrophy
ν	Kinematic viscosity
ω	Vorticity (Eq. 3.9)
$\overline{\rho}$	Mean density
$\overline{p}$	Mean pressure
$\overline{u}$	Mean velocity
ρ	Total density
ρ'	Density fluctuation from mean
ρ^+	Normalized density fluctuation
ρ_o	Reference density
b	Buoyancy flux (Eq. 2.13)
C	Courant number (Eq. 2.66)
C	Regression coefficient
C_D	Drag coefficient in grid-tow experiments
d'	Thorpe displacements
$E(\kappa)$	Energy cascade
E_p	Mean turbulent potential energy per unit mass (Eq. 2.24)
E_T	Total turbulent energy
E_{input}	Total energy input into fluid in grid-tow experiments
E_{p_n}	Potential energy after n tows in grid-tow experiments (Eq. 2.34)
f	Coriolis frequency
F_D	Drag force in grid-tow experiments
Fr	Turbulent Froude number (Eq. 2.57)
g	Acceleration of gravity
H	Tank height in grid-tow experiments
k	Turbulent kinetic energy per unit mass (Eq. 2.11)
K_ρ	Eddy diffusivity (Eq. 3.10)
k_H	Horizontal turbulent kinetic energy
k_V	Vertical turbulent kinetic energy
L	Tank length in grid-tow experiments
L	Turbulent length scale (Eq. 2.52)
L_0	Initial length scale
L_η	Kolmogorov length scale (Eq. 2.37)
L_λ	Transverse Taylor microscale (Eq. 2.42)

L_B	Batchelor scale (Eq. 2.40)
L_b	Buoyancy scale (Eq. 2.54)
L_E	Ellison scale (Eq. 2.54)
L_O	Ozmidov scale (Eq. 2.53)
L_T	Thorpe scale (Eq. B.3)
L_{T3D}	3D Thorpe scale (Eq. B.4)
M	Total number of time steps in CFD simulation
Ma	Mach number
N	Buoyancy, or Brunt-Väisälä, frequency (Eq. 2.47)
N	Number of grid points in one direction of domain
N	Number of wavenumbers
p	Total pressure
p'	Pressure fluctuation from mean
p^+	Normalized pressure fluctuation
p_o	Reference pressure
Pe_L	Turbulent Peclet number (Eq. 2.60)
Pr	Prandtl number, ratio of ν to κ
R_b	Buoyancy Reynolds number or turbulence activity parameter (Eq. 2.62)
Re_0	Initial Reynolds number(Eq. 2.58)
Re_λ	Taylor Reynolds number (Eq. 2.61)
Re_L	Turbulent Reynolds number (Eq. 2.59)
Re_M	Grid Reynolds number
Rf	Integral flux Richardson number (Eq. 2.32)
Rf_n	Flux Richardson number in grid-tow experiments after n tows
Ri	Initial Richardson number (Eq. 2.56)
Ri_g	Gradient Richardson number
Ro	Rossby number
S	Mean shear rate
s_{ij}	Rate-of-strain tensor $\frac{1}{2}(\partial u_i/\partial x_j + \partial u_j/\partial x_i)$
t	Time
t^+	Normalized time
T_0	Eddy turnover time defined from initial velocity and length scales
T_η	Kolmogorov time scale (Eq. 2.38)
T_L	Turbulent time scale (Eq. 2.51)
T_{bv}	Buoyancy time period (Eq. 2.50)
u	Horizontal velocity
u	Velocity
u'	Fluctuation from mean velocity
u^+	Normalized velocity
u_0	Initial velocity scale
u_η	Kolmogorov velocity scale (Eq. 2.39)
v	Horizontal velocity
W	Tank width in grid-tow experiments
w	Vertical velocity
x	Distance
x	Horizontal distance
x^+	Normalized distance
y	Horizontal distance
z	Vertical distance
z'	Vertical displacement from equilibrium position
D	Dissipation subrange on Kolmogorov's energy cascade
E	Energy-containing range on Kolmogorov's energy cascade
I	Inertial subrange on Kolmogorov's energy cascade
CFD	Computational Fluid Dynamics
DNS	Direct Numerical Simulation
FFT	Fast Fourier transform
LES	Large-Eddy Simulation
PDF	Probability Density Function
RANS	Reynolds-Average Navier-Stokes
RDT	Rapid-Distortion Theory